STRUCTURAL AND ELECTRICAL PROPERTIES OF Ni- AND Mg-DOPED *P*-TYPE α-$AlCrO_3$ WIDE BANDGAP SEMICONDUCTOR

M.Tech. Thesis

By

DHARAVATH VENKATESH

DEPARTMENT OF METALLURGICAL ENGINEERING AND MATERIALS SCIENCE

INDIAN INSTITUTE OF TECHNOLOGY INDORE

MAY 2025

STRUCTURAL AND ELECTRICAL PROPERTIES OF Ni- AND Mg-DOPED *P*-TYPE α-$AlCrO_3$ WIDE BANDGAP SEMICONDUCTOR

A THESIS

Submitted in partial fulfillment of the requirements for the award of the degree of

MASTER OF TECHNOLOGY

By

DHARAVATH VENKATESH
(2302105009)

DEPARTMENT OF METALLURGICAL ENGINEERING AND MATERIALS SCIENCE
INDIAN INSTITUTE OF TECHNOLOGY INDORE
MAY 2025

INDIAN INSTITUTE OF TECHNOLOGY INDORE

CANDIDATE'S DECLARATION

I hereby certify that the work which is being presented in the thesis entitled **"STRUCTURAL AND ELECTRICAL PROPERTIES OF Ni- AND Mg-DOPED P-TYPE $AlCrO_3$ WIDE-BANDGAP SEMICONDUCTOR"** in the partial fulfillment of the requirements for the award of the degree of **MASTER OF TECHNOLOGY** and submitted in the **DEPARTMENT OF METALLURGICAL ENGINEERING AND MATERIALS SCIENCE, INDIAN INSTITUTE OF TECHNOLOGY, INDORE**, is an authentic record of my work carried out during the period from July 2024 to May 2025 under the supervision of Prof. Rupesh S. Devan and Dr. Ravindra Jangir.

The matter presented in this thesis has not been submitted by me for the award of any other degree at this or any other institute.

Dharavath Venkatesh

(DHARAVATH VENKATESH)

This is to certify that the above statement made by the candidate is correct to the best of our knowledge.

Rupesh

(PROF. RUPESH S. DEVAN)

Signature with date

Jangir

(DR. RAVINDRA JANGIR)

Signature with date

DHARAVATH VENKATESH has successfully given his M.Tech. Oral Examination held on **22 May, 2025**.

Rupesh Jangir

Signature(s) of Supervisor(s) of M.Tech. Thesis

Date:

30/05/2025

Convener, DPGC

Date:

भारत सरकार
परमाणु ऊर्जा विभाग
राजा रामन्ना प्रगति प्रौद्योगिकी केन्द्र
इन्दौर -- 452013

Government of India
Department of Atomic Energy
Raja Ramanna Centre For Advanced Technology
Indore - 452013

CERTIFICATE

This is to certify that the dissertation work entitled **"STRUCTURAL AND ELECTRICAL PROPERTIES OF Ni- AND Mg-DOPED *P*-TYPE α-$AlCrO_3$ WIDE BANDGAP SEMICONDUCTOR"**, submitted by **Mr. Dharavath Venkatesh (Roll No. 2302105009)** for the partial fulfilment of **Master of Technology in Materials Science and Engineering** from the **Department of Metallurgical Engineering and Materials Science, Indian Institute of Technology Indore, M.P., India**, is hereby approved as credible work carried out by him during the period from **July 2024 to May 2025** under my supervision in the **Accelerator Physics and Synchrotrons Utilization Division** at **Raja Ramanna Centre for Advanced Technology (RRCAT), Indore, M.P., India**. The work presented has not been submitted or included in any other thesis for any degree/ diploma previously. Furthermore, it has been organized and presented in a manner suitable for acceptance towards the partial fulfilment of the requirements for the degree of Master of Technology in Materials Science and Engineering.

डॉ. रविन्द्र जांगीड़/Dr. Ravindra Jangir
वैज्ञानिक अधिकारी/Scientific Officer
भारत सरकार, परमाणु ऊर्जा विभाग
Government of India, Department of Atomic Energy
राजा रामन्ना प्रगत प्रौद्योगिकी केन्द्र
Raja Ramanna Centre for Advanced Technology
इन्दौर / Indore-452013 (M.P.)

Dr. Ravindra Jangir
Scientific Officer-G
Electron Spectroscopy and Material Lab,
Accelerator Physics and Synchrotrons Utilization Division,
RRCAT, Indore-452013

v

ACKNOWLEDGEMENTS

I would like to express my heartfelt gratitude to Prof. Rupesh S. Devan and Dr. Ravindra Jangir for their unwavering support, encouragement, enthusiasm, and exceptional knowledge throughout my M.Tech. journey. Their insightful guidance has been invaluable in every aspect of my research and the writing of this thesis. Both supervisors have played a pivotal role in deepening my understanding of the project, particularly in the areas of materials synthesis and characterization. Their mentorship has not only enhanced my technical skills but also inspired my academic growth. I am deeply thankful for their continuous motivation and for always being approachable whenever I needed advice or direction. I could not have imagined having better supervisors and mentors for my M.Tech. studies, and I am truly grateful for their dedicated support and belief in my abilities.

In addition to my supervisors, I would like to thank the rest of my thesis committee members from the MEMS department for their encouragement, insightful comments, thorough reviews, and thoughtful evaluation of my work.

I am deeply grateful to Dr. Velaga Srihari for his timely support with materials characterization, particularly through powder and capillary tube X-Ray Diffraction (XRD) characterization. His expertise and guidance in XRD analysis have been instrumental in my learning journey. My sincere thanks also go to Dr. Mangla Nand for his invaluable support in photoelectron spectroscopy characterization. I am equally thankful to Dr. Ashok Kumar Bhakar for his assistance with dielectric measurements and for always being available to help whenever I faced challenges. I would also like to extend my gratitude to Mr. Dinesh Kumar Shukla for facilitating the Seebeck measurement experiments and for his insightful contributions to my understanding of material properties.

I am indebted to RRCAT, Indore, for providing all the necessary facilities, especially the invaluable exposure to Insus-2 beamline-11 and Indus-1 beamline-3, which played a crucial role in my research.

My sincere appreciation goes to my lab-mates from the Nano-architectures Research Group, IIT Indore, for their continuous support, companionship, and motivation. I am grateful to Dr. Harshada Jadhav, Ms. Samtham Manopriya, Ms. Ekta Chaudhary, Ms. Ayushi Miglani, Ms. Suman Yadav, Mr. Ajay Patil, Mr. Ankit, Ms. Sheetal Yamalakonda, Mr. Rishav Sharma, Ms. Apurva, and Mr. Prabhat Singh for the engaging group discussions and the camaraderie we

shared throughout my thesis project. A special word of thanks goes to Mr. Rishav Sharma for his unwavering support, valuable suggestions, and motivation during this journey.

Finally, I would like to express my profound gratitude to my father, Mr. Dharavath Ramulu, my mother, Mrs. Dharavath Mankthi, my brother, Mr. Dharavath Anil, and my friends for their unconditional love, support, and patience, which have been fundamental in helping me achieve my goals. I dedicate this thesis to them. I am also thankful to the Almighty for His unconditional love and blessings throughout this journey. Lastly, I thank myself for persevering and not giving up along the way.

(Dharavath Venkatesh)

Dedicated to my Parents

TABLE OF CONTENTS

Declaration …….....iii

Certificate…….v

Acknowledgements…….……... iv

Table of content……..... ……x

Abstract…….……xiii

List of Figures …….…… ……xv

Nomenclature…….…….....xix

Acronyms…….……...……..xxi

Chapter 1: Introduction and Literature Review…… 1

1.1 Background on Transparent Conducting Oxides (TCOs)…….…..…… 2

1.2 Fundamental Challenges in Development of *p*-Type TCOs…….…..…. 3

1.3 Performance Gap Between *n*-Type and *p*-Type TCOs…….…...3

1.4 Design Strategies for *p*-Type TCOs…….....5

1.4.1 Chemical Modulation of the Valence Band (CMVB)……..…... 5

1.4.2 Electron Correlation Engineering……...…..7

1.5 Literature Review……..... 8

1.5.1 Cu-Based Oxides and Oxychalcogenides…….…….....8

1.5.2 Copper Chromium Oxide ($CuCrO_2$) ……..…..8

1.5.3 Cr_2O_3-Based *p*-Type TCOs ……..…....9

1.5.4 Gallium Chromium Oxide ($GaCrO_3$) and Ni Doping Insights…….…..10

1.6 $AlCrO_3$ as a Promising *p*-Type TCO Host ……...10

1.7 Thesis Structure…….11

Chapter 2: Motivation and Objectives ……13

2.1 Research background and significance……..14

2.1.1 $AlCrO_3$ as a promising *p*-type TCO candidate……14

2.2 Research Gap and Motivation ……...15

2.3 Doping Strategy Using Ni^{2+} and Mg^{2+} in α-$(Al_xCr_{(1-x)})_2O_3$ …….…… 16

2.3.1 Nickel (II) doping (Ni^{2+}) …….... 16

2.3.2 Magnesium (II) doping (Mg^{2+}) ……..16

2.4 Objectives of the Thesis ……17

Chapter 3: Experimental Methods ……...19

3.1 Materials and Reagents……....21

3.2 Synthesis of $AlCrO_3$ and Doped Compositions…….……..21

3.2.1 Solid-State Synthesis Procedure…….……..21

3.3 Characterization Techniques …….. 24

3.3.1 Synchrotron-Based Powder X-ray Diffraction (SXRD) Analysis ……24

3.3.2 Le-Bail Fitting Analysis…….……..25

3.3.3 Diffuse Reflectance Spectroscopy (DRS) …….……...26

3.3.4 Complex Impedance Spectroscopy (CIS) …….……27

3.3.5 Seebeck Coefficient Measurement ……28

3.3.6 Photoelectron Spectroscopy (PES) ……28

Chapter 4: Results and Discussion of Ni-Doped $AlCrO_3$ ……31

4.1 Introduction……32

4.2 Synchrotron-based X-Ray Diffraction (SXRD) Analysis…….....33

4.2.1 Le-Bail Fitting Analysis……34

4.3 Diffused Reflectance Spectroscopy (DRS) Analysis……35

4.4 Complex Impedance Spectroscopy (CIS) Analysis……...36

4.4.1 Modulus Impedance Spectroscopy……41

4.4.2 Scaling behavior Spectra: M''/M''max vs f/fmax Master Curve……...43

4.4.3 Nyquist Plot Analysis…….....45

4.5 Photoelectron Spectroscopy (PES)……50

4.6 Seebeck Coefficient Measurements……...51

4.7 Conclusion……51

Chapter 5: Results and Discussion of Mg-Doped $AlCrO_3$ ……55

5.1 Introduction……56

5.2 Structural Analysis……56

5.2.1 Synchrotron-based X-Ray Diffraction (SXRD) Analysis……56

5.2.2 Le Bail Fitting Analysis……57

5.3 Diffused Reflectance Spectroscopy……...58

5.4 Electrical Properties by CIS……...59

5.4.1 Complex Impedance Analysis……..59
5.4.2 Modulus Impedance Spectroscopy……...62
5.4.3 M'' Scaling Behaviors Spectra: M''/M''max vs f/fmax master curve…….64
5.4.4 Nyquist Plot Analysis……...67
5.5 Seebeck Coefficient Measurements……...71
5.6 Photoelectron Spectroscopy……...…71
5.7 Conclusion…….73
Chapter 6: Conclusions and Future Scope……..75
6.1 Conclusion…….……76
6.2 Future Scope……..78

ABSTRACT

In this thesis, we explore α-$AlCrO_3$ as a wide bandgap semiconductor oxide potential candidate for *p*-type doping through the strategic doping of divalent cations Ni^{2+} and Mg^{2+} at the Al^{3+} site. The host material α-$(Al_xCr_{1-x})_2O_3$ $(0 \leq x \leq 1)$ exhibits a rhombohedral structure (R-3c) with a tunable bandgap ranging from 3.4-5.3 eV and strong hybridization between Cr 3d and O 2p orbitals that makes it an ideal host for *p*-type conductivity engineering. Single-phase polycrystalline samples of α-$Al_{1-x}B_xCrO_3$, where B = Ni^{2+}, Mg^{2+} and $0 \leq x \leq 0.02$ were synthesized via the solid-state reaction method. Structural integrity and doping solubility were confirmed through synchrotron-based X-ray diffraction and Le-Bail refinement. Optical characterization via DRS reveals that with Ni doping no changes in intrinsic band transitions and thus by observed no change in bandgap energy. The electrical charge carriers transport phenomenon was thoroughly investigated using complex impedance spectroscopy (CIS). Both Ni^{2+} and Mg^{2+} doping led to significant reductions in energy activation and resistance with superior performance observed at $x = 0.01$. Notably, a transition from localized to long-range hopping conduction was evident in the doped samples, that were supported by temperature-dependent imaginary part of impedance spectra Z″, imaginary part of modulus spectra M″, and Nyquist plot analyses. Photoelectron Spectroscopy (PES) performed to obtain ionization energy of ≈ 5.7 eV and 5.1 eV for $Al_{0.99}Ni_{0.01}CrO_3$ and $Al_{0.99}Mg_{0.01}CrO_3$ respectively, making these materials viable for hole transport material applications in most of the hole transport material in perovskite solar cells. Among the studied compositions, Mg-doped α-$AlCrO_3$ ($Al_{0.99}Mg_{0.01}CrO_3$) exhibited the lowest resistance compared to the α-$AlCrO_3$ (undoped) sample and Ni-doped α-$AlCrO_3$ ($Al_{0.99}Ni_{0.01}CrO_3$) exhibited the lowest activation energy obtained and a positive Seebeck coefficient that affirms p-type conductivity. This study establishes a comprehensive structural and electrical properties of Ni- and Mg-doped *p*-type α-$AlCrO_3$ wide bandgap semiconductor and a potential candidate for *p*-type semiconducting optoelectronic applications.

LIST OF FIGURES

Figure 1.1 Comparative analysis of *n*-type TCOs (ITO) and *p*-type TCOs

Figure 1.2 Illustration of Chemical Modulation of the Valence Band through hybridization of O 2p with Cu 3d orbitals (adapted from [14]).

Figure 3.1 Schematic of the solid-state synthesis

Figure 3.2 Schematic of the box furnace program to carry calcination.

Figure 3.3 Schematic of the box furnace program to carry sintering.

Figure 4.1 X-ray Diffraction (XRD) Analysis of α-$Al_{1-x}Ni_xCrO_3$

Figure 4.2 Le-Bail fitting profile of SXRD data for α-$Al_{1-x}Ni_xCrO_3$, x =0.00, 0.005, 0.01, 0.015, and 0.02 samples using FullProf suite software. The fitting confirms the R-3c phase group across all compositions. (f) Variation of refined lattice parameter (a, c) as a function of concentration in a-$Al_{1-x}Ni_xCrO_3$.

Figure 4.3 DRS of α-$Al_{1-x}Ni_xCrO_3$ plotted as a function of Kubelka-Munk versus Energy (eV) for all samples.

Figure 4.4 Schematic representation of an equivalent circuit illustrating the distinct electrical responses of grains and grain boundaries in polycrystalline materials.

Figure 4.5 Frequency-dependent imaginary (Z") plot for ACO, ACONi05, ACONi10, ACONi15, and ACONi20 at various temperatures, showing characteristic peaks shifting shifts toward higher frequencies as the temperature rises.

Figure 4.6 Scaled Z"/Z"max versus f/f_{max} plot for the same undoped ACO and ACONi doped series, demonstrating temperature-independent relaxation behavior via perfect master curve overlap.

Figure 4.7 Arrhenius plots of ln(f_{max}) versus 1/K_BT derived from Z'' data, used to calculate activation energies for grain & grain boundaries contribution in Ni-doped ACO samples.

Figure 4.8 Shows the M" plotted across a spectrum of temperatures plotted against frequency for α-$Al_{1-x}Ni_xCrO_3$ samples (ACO, ACONi05, ACONi10, ACONi15, and ACONi20).

Figure 4.9 Scaling characteristics in the imaginary electric modulus spectral analysis i.e., M"/M"$_{max}$ vs f/f_{max} for all α-$Al_{1-x}Ni_xCrO_3$ samples (ACO, ACONi05, ACONi10, ACONi15, and ACONi20).

Figure 4.10 Arrhenius plots of ln(f_{max}) versus 1/K_BT derived from M'' spectra for all α-$Al_{1-x}Ni_xCrO_3$ samples (ACO, ACONi05, ACONi10, ACONi15, and ACONi20).

Figure 4.11 Nyquist plots (Z" versus Z') for ACO and Ni-doped ACO samples at various temperatures, displaying semicircular arcs that correspond to the electrical response of grains and grain boundaries.

Figure 4.12 Arrhenius plots of bulk (R_G) and grain boundary (R_{GB}) resistances, showing ln(R) as a function of 1/K_BT for all investigated samples.

Figure 4.13 Variation of resistance of bulk (grain) as a function of temperature. (b) Variation of activation energy of a-$Al_{1-x}Ni_xCrO_3$ samples (x = 0.0 to 0.02), obtained from the imaginary part of impedance Z", electric modulus", and Nyquist plots resistance as a function of Ni concentration (x).

Figure 4.14 (a) Valence Band of ACONi10 sample with synchrotron beam at Indus 1-beamline 3, RRCAT, Indore. (b) The spectrum is referenced with the Fermi level set at 0 eV binding energy, and ionization energies are derived from measurements using synchrotron radiation.

Figure 4.15 Linear fitting of ΔV vs ΔT to determine the Seebeck coefficient for ACONi10

Figure 5.1 X-ray Diffraction (XRD) Analysis of α-$Al_{1-x}Mg_xCrO_3$

Figure 5.2 Le-Bail fitting profile of SXRD data for α-$Al_{1-x}Mg_xCrO_3$, x =0.00, 0.005, 0.01, 0.015, and 0.02 samples using FullProf suite software. The fitting confirms the R-3c phase structure across all compositions. (f) Variation of refined lattice parameter (a, c) as a function of concentration in a-$Al_{1-x}Ni_xCrO_3$.

Figure 5.3 DRS of α-$Al_{1-x}Mg_xCrO_3$ plotted as a function of Kubelka-Munk versus Energy (eV) for all samples.

Figure 5.4 Frequency-dependent imaginary(Z") plot for ACO & Mg-doped ACO samples (ACO, ACOMg05, ACOMg10, ACOMg15, and ACOMg20) at

various temperatures, showing characteristic peaks shifting to higher frequencies with increasing temperature.

Figure 5.5 Scaled Z"/Z"$_{max}$ versus f/f_{max} plot for the same undoped ACO and ACOMg doped series, demonstrating temperature-independent relaxation behavior via perfect master curve overlap.

Figure 5.6 Arrhenius plots of ln(f_{max}) versus 1/K_BT derived from Z'' data, used to calculate activation energies for grain & grain boundaries contribution in Mg-doped ACO samples.

Figure 5.7 Frequency-dependent plots of M" at various temperatures for α-$Al_{1-x}Mg_xCrO_3$ samples (ACO, ACOMg05, ACOMg10, ACOMg15, and ACOMg20).

Figure 5.8 Scaled plots of the imaginary part of the modulus spectra, highlighting the consistent behavior across different temperatures, i.e., M"/M"$_{max}$ vs f/f_{max} for all α-$Al_{1-x}Mg_xCrO_3$ samples (ACO, ACOMg05, ACOMg10, ACOMg15, and ACONMg20).

Figure 5.9 Arrhenius plots of ln(f_{max}) versus 1/K_BT derived from M'' spectra for all α-$Al_{1-x}Mg_xCrO_3$ samples (ACO, ACOMg05, ACOMg10, ACOMg15, and ACOMg20).

Figure 5.10 Nyquist (Z" vs Z') for ACO and Mg-doped ACO samples at different temperatures, indicating a semicircular arc attributed to grain and grain boundaries response.

Figure 5.11 Arrhenius plots of bulk (R_G) and grain boundary (R_{GB}) resistances, showing ln(R) as a function of 1/K_BT for all investigated samples.

Figure 5.12 (a) Dependence of bulk (grain) resistance on temperature (b) Variation of activation energy of α-$Al_{1-x}Mg_xCrO_3$ samples (x = 0.0 to 0.02), obtained from the imaginary part of impedance Z", electric modulus", and Nyquist plots resistance as a function of Mg concentration (x).

Figure 5.13 Comparative analysis of Resistance vs Temperature of ACO, ACONi10 and ACOMg10.

Figure 5.14 Linear fitting of ΔV vs ΔT to for ACOMg10 to extract the Seebeck coefficient.

Figure 5.15 (a) Valence Band of ACONi10 sample with synchrotron beam at Indus 1-beamline 3, RRCAT, Indore. (b) The spectrum is referenced with the Fermi level set at 0 eV binding energy, and ionization energies are derived from measurements using synchrotron radiation.

NOMENCLATURE

Symbol / Term	Description
R	Resistance of the material (Ω)
R_0	Pre-exponential factor in Arrhenius equation; resistance at $T \rightarrow \infty$
E_a	Activation energy for charge transport (eV)
K_B	Boltzmann constant (8.617×10^{-5} eV·K^{-1})
T	Absolute temperature (K)
Z″	Imaginary part of the impedance spectra
M″	Imaginary part of the electric modulus spectra
f_{max}	Peak frequency in Z″ or M″ spectrum
C_0	Geometric capacitance of the sample (F)
σ (S/cm)	Electrical conductivity
n (cm^{-3})	Carrier concentration
μ (cm^2/V·s)	Carrier mobility
E_g	Optical bandgap energy (eV)
T (%)	Optical transmittance percentage
d (nm)	Film or sample thickness
V	Unit cell volume ($Å^3$)
a, c	Lattice parameters (Å)

ACRONYMS

TCO	Transparent Conducting Oxide
ITO	Indium Tin Oxide
CIS	Complex Impedance Spectroscopy
XRD	X-ray Diffraction
DRS	Diffuse Reflectance Spectroscopy
PES	Photoelectron Spectroscopy
VBM	Valence Band Maximum
CBM	Conduction Band Minimum
CMVB	Chemical Modulation of the Valence Band
PLD	Pulsed Laser Deposition
MBE	Molecular Beam Epitaxy
NTCR	Negative Temperature Coefficient of Resistance
DFT	Density Functional Theory
CPE	Constant Phase Element
I.E	Ionization Energy

Chapter 1
Introduction

1.1 Background on Transparent Conducting Oxides (TCOs)

Transparent conducting oxides (TCOs) materials are a remarkable class of materials that exhibit two contradictory properties in one material, i.e., optical transparency and electrical conductivity simultaneously. Typically, materials which exhibit excellent electrical conductivity, such as metals, tend to be opaque due to their high free-electron density, which leads to strong absorption and reflection of visible spectrum. On the other hand, materials that are optically transparent, such as glass and ceramics, behave like electrical insulators because they lack free charge carriers. TCOs bridge this gap by addressing a potential candidate material that exhibits both contradictory properties in one material through careful engineering of their electronic structure which allows to satisfy both properties requirements simultaneously[1].

To function as efficient TCO materials, they must satisfy several fundamental requirements. Most importantly, the material must possess a wide optical bandgap energy of ≥ 3.1 eV to avoid optical absorption in the visible spectrum. In addition to that, to facilitate electrical conduction, it must possess sufficient charge carriers such as electrons for *n*-type TCOs and holes for *p*-type TCOs. Moreover, these charge carriers must exhibit high mobility for conduction processes that allow us to achieve high conductivity values[2]. The difficulty lies in careful engineering and obtaining these properties within a single material system simultaneously. Therefore, the conventional approach to developing TCO materials involves creating non-stoichiometry and/or introducing defects in wide bandgap semiconductors. By strategically introducing shallow defects state near the conduction band maximum for *n*-type materials or for the valence band for *p*-type materials, in that way it's possible to enhance conductivity at room temperature while maintaining optical transparency. This combined balance of properties faces significant challenges, particularly for *p*-type materials, driving the search for novel materials systems and design strategies[3].

The importance of TCOs in optoelectronics resulted as a critical component in diverse applications, including flat panel displays, touch screens, light-emitting diodes (LEDs),photovoltaic (PV) cells, electro-chromic smart windows, and emerging transparent electronics[4-8]. The importance of TCOs plays a critical role in optoelectronics, and future

innovations would result in a global market valued at approximately United States Dollar (USD) of valued at 7.5 billion in 2022, the market is expected to grow to USD 12.8 billion by 2030. As the demand for technological importance has driven intensive research efforts aimed at the development of TCOs with enhanced performance, improved stability and reduced environmental impacts.

1.2 Fundamental challenges in the development of *p*-type TCOs

The *n*-type TCOs have achieved significant commercial success in the market, whereas the development of equally the realization of highly efficient *p*-type TCOs is one of the most persistent challenges in transparent optoelectronic applications. This disparity stems from fundamental limitations in the electronic structure of oxide materials that result in *p*-type doping inherently more difficult than *n*-type doping. The fundamental challenge lies in the nature of the valence band in conventional oxide semiconductors. The valence band maximum (VBM) in most semiconductors is predominantly composed of oxygen 2p orbitals and due to oxygen's high electronegativity, orbitals are strongly localized, resulting in several detrimental effects for hole transport. Firstly, flat valence bands with minimal dispersion, which means the localized nature of O 2p orbitals results in narrow valence bands with minimal dispersion. This leads to high effective masses for holes, resulting in inherently low hole mobility. In *p*-type oxides, dopants create deep acceptor states instead of shallow levels near the VBM, while electron-phonon coupling induces small polaron formation, both of which degrade hole mobility. And lastly, compensating defects due to native donor defects like oxygen vacancies compensate for intentionally introduced acceptors. These fundamental limitations result in poor performance of *p*-type TCO's conductivity, which is significantly lower than their *n*-type counterparts [9].

1.3 Performance Gap Between *n*-Type and *p*-Type TCOs

The disparity in performance of *n*-type and *p*-type materials can be understood by comparative analysis of their properties. Figure 1.1 provides a comparative illustration of the inverse sheet resistance and optical transmission for various *p*-type TCOs reported in the literature (represented by red squares) and the commercial *n*-type indium tin oxide (ITO) alongside was shown as a benchmark [10]. The data highlights the persistent disparity in performance between n-type and p-type TCOs. Moreover, we can observe that

commercially available *n*-type ITO exhibits both high optical transmission and low sheet resistance, whereas most *p*-type TCOs in the region exhibit lower transmission and higher resistance. For instance, materials such as $BaBiTaO_6$, $SrCuO_2$, and SnO exhibit relatively high optical transmission but suffer from limited electrical conductivity as indicated by their lower inverse sheet resistance. As shown in Figure 1.1, it can be seen that no *p*-type TCO has achieved a combination of electrical and optical properties that rival those of commercial *n*-type TCO.

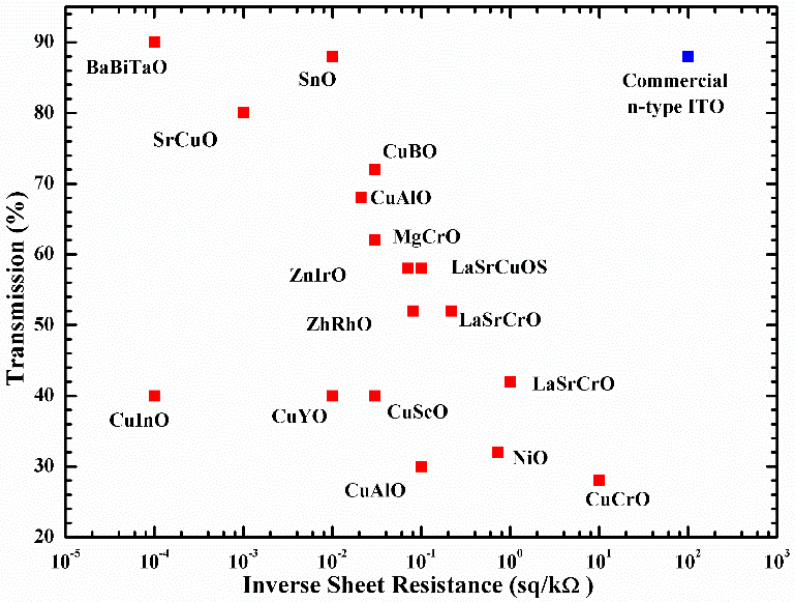

Figure 1.1: Comparative analysis of *n*-type TCOs (ITO) and *p*-type TCOs

Materials	Structure	Growth methods	*d* (nm)	*T* (%)	E_{opt} (eV)	σ (S cm^{-1})	*n* (cm^{-3})	μ ($cm^2 V^{-1} s^{-1}$)
Sn:In_2O_3 (ITO)	Bixbyite	Sputtering	115	85	3.7	5900	1.2×10^{21}	30
Cu_2O	Cubic	PLD	650	—	2.17	0.014	1.7×10^{14}	90
$CuBO_2$	Delafossite	PLD	200	75	4.5	1.65	1×10^{17}	100
$CuAlO_2$	Delafossite	PLD	500	28	3.5	0.95	1.3×10^{17}	10.4
$CuAlO_2$	Delafossite	PLD	230	70	3.5	0.34	2.7×10^{19}	0.13
$CuGaO_2$	Delafossite	PLD	300	80	3.6	0.02	1.7×10^{18}	0.23
$La_{0.50}Sr_{0.50}CrO_3$	Perovskite	MBE	50	43	4.6	56	7.5×10^{21}	0.04

Table 1.1. Overview of prominent p-type TCOs documented in previous studies [10]

As shown in Table 1.1, it highlights the superior performance of the *n*-type TCO of ITO compared to various *p*-type TCOs [13]. Here, ITO, with a bixbyite structure which

was deposited via sputtering, has demonstrated an impressive optical transmittance of 85% and an outstanding electrical conductivity of 5900 $S\,cm^{-1}$. This high performance is attributed to its substantial carrier concentration ($\sim 1.2 \times 10^{21}\,cm^{-3}$) and high carrier mobility ($\sim 30\,cm^2\,V^{-1}\,s^{-1}$). On the other hand, *p*-type TCOs such as $CuAlO_2$, $CuGaO_2$, and $La_{0.50}Sr_{0.50}CrO_3$, despite possessing wide optical bandgaps which are suitable for transparent applications and exhibit significantly lower electrical conductivity and mobilities. For instance, $CuAlO_2$ and $CuGaO_2$ are both delafossite-structured by developing a delafossite and developed via pulsed laser deposition (PLD), exhibiting limited conductivity ($\leq 1\ S\,cm^{-1}$) and moderate transparency. Although certain delafossites, such as $CuBO_2$, report higher mobilities ($\sim 100\,cm^2V^{-1}s^{-1}$) but their overall electrical performance remains constrained due to low carrier concentrations ($\sim 10^{17}\,cm^{-3}$). Similarly, a perovskite-structured $La_{0.50}Sr_{0.50}CrO_3$ material synthesized by molecular beam epitaxy (MBE) exhibits a relatively high carrier concentration ($\sim 7.5 \times 10^{21}\,cm^{-3}$) but is hindered by extremely low hole mobility ($\sim 0.04\,cm^2V^{-1}\,s^{-1}$) and thus limits its conductivity ($\sim 56\,Scm^{-1}$) [10]. These comparisons present the inherent material limitations and that continue to challenge the advancement of high-performance *p*-type TCOs.

1.4 Design Strategies for *p*-Type TCOs

To address the fundamental challenges linked to *p*-type doping in semiconducting oxides, there were two major conceptual approaches that have emerged such as (i) Chemical Modulation of the Valence Band (CMVB) and (ii) Electron Correlation Engineering. These strategies have resulted in the identification and development of several promising *p*-type TCO materials that include delafossites, oxychalcogenides, and chromium-based oxides [9].

1.4.1 Chemical Modulation of the Valence Band (CMVB)

In 1997, Hosono et.al developed the concept of Chemical Modulation of the Valence Band (CMVB) to deal with the more dispersive valence band of O2p orbitals. This approach has been introduced for hybridization of O 2p with nearly closed energy orbitals to delocalize the hole and engineer the Valence Band Maximum (VBM) to reduce the effective mass of holes. As shown in the Figure 1.2, this is achieved by hybridizing the O 2p orbitals with suitable metal cation states such as filled d-orbitals (d^{10} configuration) or

lone pair s-orbitals (s^2 configuration), which are more spatially extended and capable of forming strong hybrid states.

The CMVB strategy involves primarily three key design principles as follows:

1. **d^{10} configuration cations**: Cations with a closed-shell d^{10} electronic configuration such as Cu^+ ($3d^{10}$), Ag^+ ($4d^{10}$), and Au^+ ($5d^{10}$) are more advantageous materials that avoids the d-d transitions and facilitate the hybridization of their metal d-orbital with O 2p orbitals. Moreover, this hybridization contributes to valence band delocalization and promotes higher hole mobility.

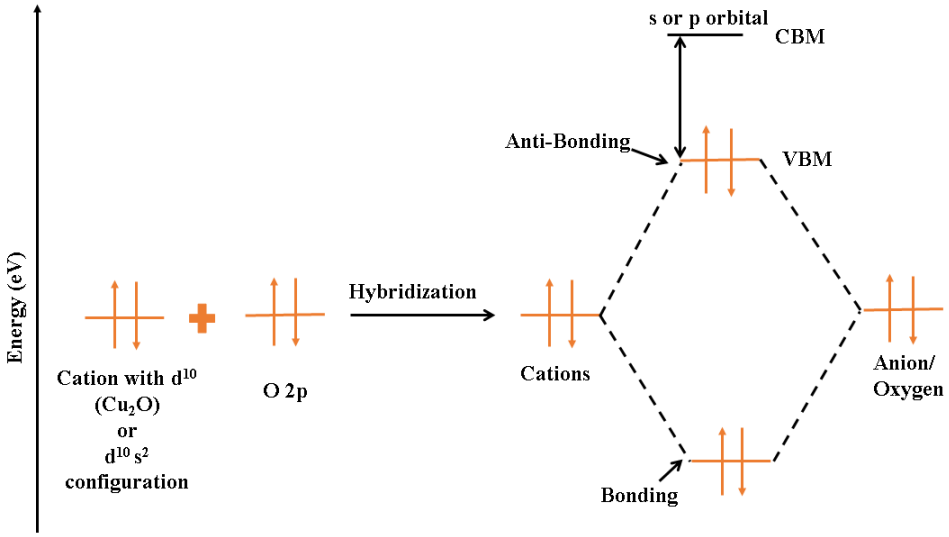

Figure 1.2: Illustration of Chemical Modulation of the Valence Band through hybridization of O 2p with Cu 3d orbitals (adapted from [14]).

2. **Incorporation of s^2 Configuration Cations**: Non-transition metal cations such as Sn^{2+} ($5s^2$) and Bi^{3+}($6s^2$), which possess the active lone pairs result to interact with O 2p orbitals, and that leads to a more dispersive valence band. The inclusion of such cations helps in raising the VBM and thereby enhancing the hole transport phenomenon.

3. **Energy Level Alignment**: For hybridization the cation orbital states energy must lie close in energy to the O 2p orbitals levels. This band alignment ensures significant hybridization and results in the formation of bonding and antibonding states with the antibonding VBM which leads to exhibiting higher dispersion. This directly contributes to reduced hole effective mass and improved conductivity.

An early and successful demonstration of this strategy was realized in the delafossite $CuAlO_2$ exhibits a wide optical bandgap (~3.5 eV), where Cu^+ ($3d^{10}$) cations hybridize with O 2p orbitals and result in dispersive VBM and *p*-type conductivity in the range of ~1 $S \cdot cm^{-1}$. Although the conductivity reported was modest, this material represented the first proof-of-concept for *p*-type TCOs and laid the foundation for future research into valence band-engineering [14].

This CMVB-based design approach has led to the development of a wide range of *p*-type TCOs, including delafossite oxides, oxychalcogenides, and spinel-based oxides, all aiming to replicate the success of Cu-based delafossites while enhancing mobility and conductivity [13-15].

1.4.2 Electron Correlation Engineering

Another design strategy exploits electron correlation effects, which are particularly observed in transition metal oxides with partially filled d-orbitals. Unlike CMVB, this approach will not only rely on delocalized oxygen orbitals but instead utilizes correlated electron systems where controlled hole doping can enable *p*-type transport simultaneously maintaining optical transparency. A prominent example of this strategy is the *p*-type materials conduction observed in Sr-doped $LaCrO_3$, a perovskite oxide. In this system, upon Sr substitution $La_{1-x}Sr_xCrO_3$ hole carriers are introduced into the Cr 3d (t_{2g}) band resulting in relatively delocalized holes that participate in electrical conduction [9,10]. Importantly, optical transparency is preserved because the Cr^{3+}/Cr^{4+} transitions are dipole-forbidden and thus do not contribute significantly to optical absorption in the visible range. This concept has also been extended to other correlated oxide systems such as LaCuOSe and $LaCrO_3$-based systems.

In addition, to further support the design of such systems as well as first-principles computational methods for including density functional theory (DFT) to improve the description of strongly correlated electron systems, particularly those involving localized orbitals, like in transition metal oxides and hybrid functional approaches, are employed to predict and model the band structure, hole effective mass, and polaronic behavior. These tools help in screening and exploring new materials systems and understanding the trade-offs between conductivity and transparency. The electron correlation approach

demonstrates that even in systems with strong Coulomb interactions and partially filled d-bands, it is possible to achieve *p*-type behavior with reasonable transport properties if transitions remain optically inactive and carriers remain delocalized.

Together, these strategies have broadened the landscape of *p*-type TCO materials, with Cr-based oxides gaining increasing attention for their compatibility with both CMVB and correlation-driven mechanisms.

1.5 Literature Review

1.5.1 Cu-Based Oxides and Oxychalcogenides

Based on the *p*-type design strategies, early research was focused on Cu^{+}-based oxides as promising *p*-type TCO candidates. Cu(I) compounds were attractive because Cu^{+} has filled $3d^{10}$ orbitals that can hybridize with anion p-orbitals, yielding a maximum valence band (VBM) that is less O 2p dominated. The breakthrough came in 1997, when Kawazoe *et al.* reported transparent *p*-type conduction in $CuAlO_2$ which is delafossite-structured of Cu^{+} oxide [11]. Thin films of $CuAlO_2$ exhibited a *p*-type conductivity on the order of ~1 Scm^{-1} at room temperature. While modest, this conductivity was remarkable at the time, and it demonstrated for the first time that a wide-bandgap oxide could facilitate hole transport. $CuAlO_2$ has a rhombohedral layered structure with an indirect bandgap of ~3.5 eV, yielding ~80% transparency in the visible. This work proved that the CMVB strategy that is hybridizing O 2p with closed-shell Cu 3d orbital could successfully address the issues of *p*-type doping, and it paved the way for a "proof-of-concept" *p*-type TCO.

1.5.2 Copper Chromium Oxide ($CuCrO_2$)

This material is a shining example of a *p*-type TCO achieved through CMVB. This adopts the delafossite structure ABO_2 type, with $A = Cu^{+}$, $B = Cr^{3+}$ and has a rhombohedral layered structure. The presence of Cu^{+} ($3d^{10}$) is the key as delocalizing the valence band through Cu 3d and O 2p hybridization via CMVB strategy, resulting in *p*-type conductivity. Undoped $CuCrO_2$ has a band gap of approximately 3.0 eV (indirect) and around 3.5 eV (direct), making it transparent with a slight greenish tint. In 1997, $CuCrO_2$ was reported as a *p*-type TCO shortly after $CuAlO_2$ demonstrating that replacing Al with Cr in the delafossite structure also yields *p*-type behavior. The performance of $CuCrO_2$ was further

improved by aliovalent doping such as Mg^{2+} doping on the Cr^{3+} site forming $CuCr_{1-x}Mg_xO_2$ [12] has been shown to dramatically increase hole concentration. Magnesium doping provides acceptor defects (each Mg^{2+} creates a deficiency of positive charge that must be compensated by a hole on neighboring O/Cr sites). As a result, the conductivity of $CuCrO_2$ can rise by orders of magnitude upon Mg doping. For instance, Mg-doped $CuCrO_2$ films have achieved conductivity on the order of ~10 S/cm with visible transparency around 70-80% for thin films. This is still modest compared to *n*-type TCOs but is a remarkable improvement for *p*-type semiconductor oxides. Mg-doped $CuCrO_2$ is often cited as one of the best *p*-type TCOs to date. Its success illustrates two important points: (1) the effectiveness of the Cu^+ and Cr^{3+} chemistry in achieving *p*-type conduction; and (2) the principle that divalent cation doping (Mg^{2+}) on a trivalent site is a viable way to introduce holes in a Cr-based oxide. $CuCrO_2$ exhibits a high optical band gap of approximately 3 eV, contributing to its substantial to optical transparency.

1.5.3 Cr_2O_3-based *p*-Type TCOs

Cr_2O_3 also known as eskolaite, is a wide-bandgap oxide with a bandgap ~3.4 eV with a corundum crystal structure as same structure as Al_2O_3. Pure Cr_2O_3 is an insulating antiferromagnetic oxide. Its valence band consists of O 2p mixed with some Cr 3d (t_{2g}) states, and it does not intrinsically conduct holes. In principle, if one could introduce acceptors into Cr_2O_3, *p*-type conduction might occur. However, attempts to dope Cr_2O_3 for *p*-type conductivity are scarcely reported, likely due to the tendency of Cr_2O_3 to accommodate changes by oxidation states like Cr^{3+} to Cr^{4+} or Cr^{2+} or some other defect formation rather than free-hole creation. Moreover, Cr_2O_3 is transparent in the green part of the spectrum while it absorbs in the red and its band gap, just around the visible range, might be slightly low for some transparent applications. Thus, Cr_2O_3 alone has not emerged as a useful *p*-type TCO [13]. To overcome this intrinsic limitation, doping strategies have been effectively utilized. For instance, Magnesium (Mg^{2+}) doping in α-Cr_2O_3, has demonstrated marked success, elevating conductivity levels up to 28 S/cm [14]. The introduction of Mg^{2+} ions helps to modulate electronic structures, enhance the delocalization of holes and improving *p*-type conductivity. Similarly, nickel (Ni^{2+}) doping has been investigated to further optimize electronic structures. Ni^{2+} doping reduces hole effective mass, thereby increasing mobility and enhancing overall conductivity. Such

doping methods maintain the desired transparency of the material while significantly improving electrical characteristics.

1.5.4 Gallium Chromium Oxide ($GaCrO_3$) and Ni Doping Insights

While Cu-based delafossites rely on Cu^+ hybridization, more recent studies have focused on chromium oxides combined with trivalent A-site cations such as Ga^{3+}, forming $GaCrO_3$ [15]. This material provides structural and chemically valuable insight into dopant behavior. In recent report by R. Jangir et al demonstrated the Ni^{2+} doping in $GaCrO_3$ has exhibited *p*-type conductivity while preserving a wide bandgap of ~4.1 eV which was among the highest bandgap reported till date for *p*-type TCOs [16]. Furthermore, Ni-doped $GaCrO_3$ grown epitaxially on Al_2O_3 substrates and showed good crystallinity, aligned band structures were reported [18]. Ni^{2+} introduces acceptor states by substituting for Ga^{3+}, which creates a charge imbalance that can be compensated by hole formation on Cr or O sites. Furthermore, Ni 3d states may participate in valence band formation, further assisting hole delocalization. These studies confirm that transition-metal doping on group 13 cation sites (Ga^{3+}, Al^{3+}) in Cr-based oxides is a viable pathway to achieving *p*-type conduction with excellent optical properties.

1.6 $AlCrO_3$ as a Promising *p*-Type TCO Host

Building upon the insights from $CuCrO_2$ and $GaCrO_3$ materials, the focus of this thesis is on Aluminum Chromium Oxide ($AlCrO_3$) which is an unexplored material yet highly promising host *p*-type semiconductor. $AlCrO_3$ can be synthesized as a solid solution of Al_2O_3 and Cr_2O_3 by solid-state synthesis method both of which crystallize in the corundum structure (space group R-3c) [19]. The bandgap of $AlCrO_3$ lies between the narrow gap of Cr_2O_3 (~3.4 eV) and the ultrawide bandgap of Al_2O_3 (~8.8 eV). Experimental studies by Jangir et al. have reported α-$(Al_xCr_{1-x})_2O_3$ bandgaps tunability in the range of ~3.4 to 5.3 eV. Structurally, α-$(Al_xCr_{1-x})_2O_3$ offers full miscibility across the Al-Cr composition of $0 \leq x \leq 1$ range and excellent thermal and chemical stability. This enables high-temperature processing and compatibility with transparent device platforms. Importantly, the mixed cation (Al/Cr) lattice allows for strategic doping at the Al^{3+} or Cr^{3+} sites, enabling fine-tuned control over valence band characteristics.

This chapter has reviewed the fundamental challenges in developing *p*-type TCOs and outlined key design strategies including CMVB and electron correlation engineering. The literature survey highlights the promise and limitations of Cu-based, Cr-based, and Ga-based systems, leading to the rationale for investigating $AlCrO_3$ as a stable and tunable host material.

1.7 Thesis Structure:

- **Chapter 2** presents the motivation and clearly defined objectives of the research.
- **Chapter 3** outlines the experimental methodology, including synthesis and characterization techniques.
- **Chapter 4** discusses the results of Ni-doped $AlCrO_3$.
- **Chapter 5** presents results for Mg-doped $AlCrO_3$.
- **Chapter 6** concludes the thesis with key findings and future work.

Chapter 2
Motivation and Objectives

2.1 Research Background and Significance

2.1.1 $AlCrO_3$ as a promising *p*-type TCO candidate

Herein, α-$(Al_xCr_{(1-x)})_2O_3$ system is one among the emerging materials in the field of *p*-type wide bandgap semiconductors. This material adopts a rhombohedral crystal structure (space group R-3c) and closely resembles the well-known corundum structure of its end parent structureα-Al_2O_3 and α-Cr_2O_3 [19]. Within this lattice, Al^{3+} and Cr^{3+} cations occupy octahedral sites and are arranged crystallographic site and enabling compositional tuning without disrupting the structural integrity. One of the most striking features of this system is its wide band gap tunability, which allows the bandgap tunability from approximately 3.4 eV in the α-$(Al_xCr_{(1-x)})_2O_3$ at (x = 0) to 5.3 eV (x = 1). This broad optical window not only ensures excellent transparency in the visible region but also ranks among the largest bandgap tunability ranges reported for Cr-based oxide systems to date. The ability to tailor the bandgap across such a wide spectrum without compromising structural coherence is a rare and valuable trait for TCO design. Furthermore, the system displays full solid solubility between α-Al_2O_3 and α-Cr_2O_3 and avoiding the common challenge of immiscibility or secondary-phase formation compared to that of many other oxides. This full miscibility enables precise control over stoichiometry and dopant distribution, thereby enabling property optimization across the entire compositional range.

Moreover, crucial advantage that lies in the valence band structure of α-$(Al_xCr_{(1-x)})_2O_3$ was studied by computational based studies such as DFT and experimental investigations via photoelectron spectroscopy (PES) have shown that the VBM is predominantly derived from Cr 3d orbital and hybridized with O 2p orbital. The substitution of Al introduces a higher degree of hybridization that allowed O 2p orbital hybridization into the VBM which effectively delocalizes the holes and potentially enhances their mobility. Therefore, this valence band engineering plays a pivotal role in enabling *p*-type conduction and distinguishes this system from the parent α-Cr_2O_3, which suffers from localized hole states. Additionally, material possesses exceptional thermal and chemical stability and is inherited from its corundum structure which is highly desirable for real-world device applications where stability under harsh conditions is a prerequisite. Furthermore, the compatibility of this material with existing transparent semiconducting

oxide materials technologies needs further supports its candidacy for integration into optoelectronic and photovoltaic applications. These properties and advantages make α-$(Al_xCr_{(1-x)})_2O_3$ as a promising platform for developing *p*-type TCOs with tunable band gaps and can enhance the hole mobility through strategic doping approaches.

2.2 Research Gap and Motivation

The α-$(Al_xCr_{(1-x)})_2O_3$ system has a lot of potential as a *p*-type transparent conducting oxide but its current applicability is limited by a number of important scientific questions that have not yet been resolved. Although it is a promising platform due to its wide bandgap tunability (3.4-5.3 eV), structural compatibility, and full miscibility between α-Al_2O_3 and α-Cr_2O_3 the mechanisms governing its optoelectronic behavior, particularly upon doping, remain unexplored. This results in a sizable research gap that requires methodical study.

Understanding the impact of aliovalent doping, especially with divalent cations like Ni^{2+} and Mg^{2+}, is one of the main knowledge gaps. Despite earlier research showing effective *p*-type conductivity enhancement in related systems such as $CuCrO_2$ (by Mg^{2+} doping at Cr^{3+} site) [12] and $GaCrO_3$ (by Ni^{2+} doping at Ga^{3+} site) [16-19] whereas α-$(Al_xCr_{(1-x)})_2O_3$ in such approaches have not been thoroughly investigated. Furthermore, little is known about the conduction mechanisms in doped α-$(Al_xCr_{(1-x)})_2O_3$[19]. Temperature-dependent impedance and resistivity analyses are still needed to confirm whether these dopants cause defect-mediated conduction, band-like transport, or localized polaronic hopping. To optimize material performance for practical applications, this knowledge must be established.

2.3 Doping Strategies Using Ni^{2+} and Mg^{2+} in α-$(Al_xCr_{(1-x)})_2O_3$

Introducing a small amount of doping of divalent cation (2+ charge) in place of a trivalent cation (3 + charge) is a classical way to create acceptor defects that are holes in the oxides. Both Ni (II) (69 pm) and Mg (II) (72 pm) are promising acceptor dopants for $AlCrO_3$ due to their compatible chemistry and ionic radii. The idea is when Ni^{2+} and Mg^{2+} replace Al^{3+} in the $AlCrO_3$ lattice, where deficiency of charge compensated by Cr by converting Cr^{3+} to Cr^{4+} which effectively donates a hole. The net effect is contributed to *p*-

type conductivity. The mechanism is an analogous to $CuCrO_2$ (Mg^{2+} on Cr^{3+}) which resulted in holes on O/Cr & boosted conductivity [12] and Ni doped $GaCrO_3$ (Ni^{2+} on Ga^{3+}) which achieved *p*-type conduction as reported [16-17].

2.3.1 Nickel (II) doping (Ni^{+2})

NiO is highly explored *p*-type oxide semiconductor, where Ni often exists partly Ni^{3+} state to provide holes. In the context of Ni^{2+} has an ionic radius of (~0.69Å in octahedral coordination) that is reasonably close to that of Cr^{3+} (~0.62Å) and Al^{3+} (~0.53Å). Although slightly larger, small amounts of Ni^{2+} can be expected to substitute into the corundum lattice without severe strain. Further, with Ni substitutes into $AlCrO_3$; the possible electronic configuration scenarios would be that Nickel stays as Ni^{2+} and nearby Cr^{3+} is oxidized to Cr^{4+}, which would indicate that a hole is now on the Cr site making the material *p*-type.

Therefore, Ni doping is expected to introduce holes. In other hand, one must be caution of Ni is doped in too high concentration, it may lead to form its own phases like NiO or $NiAl_2O_4$ or lead to mid-gap impurity band that could enhance conductivity but also cause sub-gap absorption. Thus, Ni doping will be kept at a moderate level of a few atomic percent to ensure single-phase transparent materials.

2.3.2 Magnesium (II) doping (Mg^{2+})

Magnesium is a non-transition metal with a $3s^2$ configuration and no d orbital. Mg^{2+} has an ionic radius of ~0.62Å in octahedral coordination similar to Ni^{2+} and slightly larger than Cr^{3+}. It is well known as an acceptor dopant in various semiconductors like $CuCrO_2$, Mg doping method highly effective in generating holes. When Mg^{2+} substitutes for Cr^{3+}/Al^{3+} in $AlCrO_3$, it cannot undergo further oxidation of Mg^{3+}, which is extremely unstable, so charge compensation must occur by oxidizing the surrounding lattice. Another consideration is that Mg doping is an alkaline earth metal, we ensure that Mg-doping in $AlCrO_3$ remains within solubility to avoid secondary phase MgO or Mg $(Cr,Al)_2O_4$. The expected outcomes, to incorporate Mg into the lattice & activate holes to increase p-type conductivity.

In summary, Ni^{2+}/Mg^{2+} were selected as dopants for $AlCrO_3$ due to successful use in analogous system of Ni doping in $GaCrO_3$ [16] and Mg doping in $CuCrO_2$[12], their ionic compatibility with host and their potential to generate holes, by pursing both, we also gain the opportunity to compare a transition metal acceptor vs alkaline earth acceptor in some hosts which deeper the understanding of how different dopants influence *p*-type oxide properties.

2.6 Objectives of the Thesis

Based on the identified research gaps and the promising characteristics of α-$(Al_xCr_{(1-x)})_2O_3$ material as a *p*-type TCO host and the specific objectives of this thesis are outlined as follows:

Objective 1: To investigate the effect of Ni^{2+} doping at the Al^{3+} site in $AlCrO_3$ (α-$Al_{1-x}Ni_xCrO_3$ and $_3$, x = 0.00, 0.005, 0.01, 0.015 and 0.02) on structural, optical, and electrical properties, aiming to enhance *p*-type conductivity through partial substitution and valence band modulation.

Objective 2: To explore the role of Mg^{2+} doping at the Al^{3+} site in $AlCrO_3$ ($Al_{1-x}Mg_xCrO_3$ x = 0.00, 0.005,0.01,0.015 and 0.02) for achieving *p*-type behavior by introducing acceptor states, while evaluating changes in band structure and transport characteristics using solid-state synthesized polycrystalline samples. Emphasis is placed on the role of partial Ni^{2+}/Mg^{2+} substitution in modulating the valence band structure to enhance hole concentration and improve *p*-type conductivity. Comprehensive characterizations were performed using synchrotron XRD with Le-Bail refinement, UV-Vis diffuse reflectance spectroscopy (DRS), and complex impedance spectroscopy (CIS).

Chapter 3
EXPERIMENTAL METHODOLOGY

3.1 Materials and Reagents

In our study, the method was employed to synthesize undoped $AlCrO_3$ and its Ni- and Mg-doped variants (α-$Al_{1-x}B_xCrO_3$, where B = Ni, Mg, and $0 \leq x \leq 0.02$). The synthesis approach was optimized through stoichiometric precursor weighing. The sample was manually ground using a mortar and pestle, followed by ball milling. A high-temperature calcination process ensured phase formation. For densification, sintering was performed. Detailed procedures are outlined in the following sections. Thereby, we investigate the structural, optical, and electrical properties by various characterization.

For synthesis of single phase polycrystalline α-$Al_{1-x}Ni_xCrO_3$ and $Al_{1-x}Mg_xCrO_3$, high-purity Aluminium Oxide (α-Al_2O_3, 99.997%, Alfa Aesar), Chromium (III) Oxide (Cr_2O_3, 99.97%, Alfa Aesar), Nickel (II) Oxide (NiO, 99.99%, Alfa Aesar), and Magnesium Oxide (MgO, 99.95%, Alfa Aesar) served as the primary precursors. Stoichiometric proportions were calculated to achieve the general formula, for Ni-doped is $Al_{1-x}Ni_xCrO_3$ and Mg-doped is $Al_{1-x}Mg_xCrO_3$, where x = 0, 0.005, 0.01, 0.015, and 0.02 for respectively. The appropriate amounts of powders were calculated according to equations 3.1 and 3.2.

$$\text{For Ni doping: } (1-x)\,Al_2O_3 + Cr_2O_3 + 2xNiO \rightarrow 2Al_{1-x}Ni_xCrO_3 \qquad 3.1$$

$$\text{For Mg doping: } (1-x)\,Al_2O_3 + Cr_2O_3 + 2xMgO \rightarrow 2Al_{1-x}Mg_xCrO_3 \qquad 3.2$$

Two separate syntheses were considered as part of our work for comparative analysis:

- Synthesis 1: Ni-doped $AlCrO_3$ i.e., α-$Al_{1-x}Ni_xCrO_3$ samples at different concentration levels (x= 0.00, 0.005,0.01,0.015 and 0.02) synthesized and labelled as ACO, ACONi05, ACONi10, ACONi15 and ACONi20 respectively.
- Synthesis 2: Mg-doped $AlCrO_3$ i.e., α-$Al_{1-x}Mg_xCrO_3$ samples at different concentration levels (x = 0.00, 0.005,0.01,0.015 and 0.02) synthesized and labelled as ACO, ACOMg05, ACOMg10, ACOMg15 and ACOMg20 respectively.

3.2 Synthesis of $AlCrO_3$ and Doped Compositions

3.2.1 Solid-State Synthesis Procedure

The synthesis procedure followed for preparing samples is illustrated in Figure 3.1. Each step in this process is very important to ensuring the synthesis of single-phase polycrystalline samples and repeatability. The procedure for synthesis as follows:

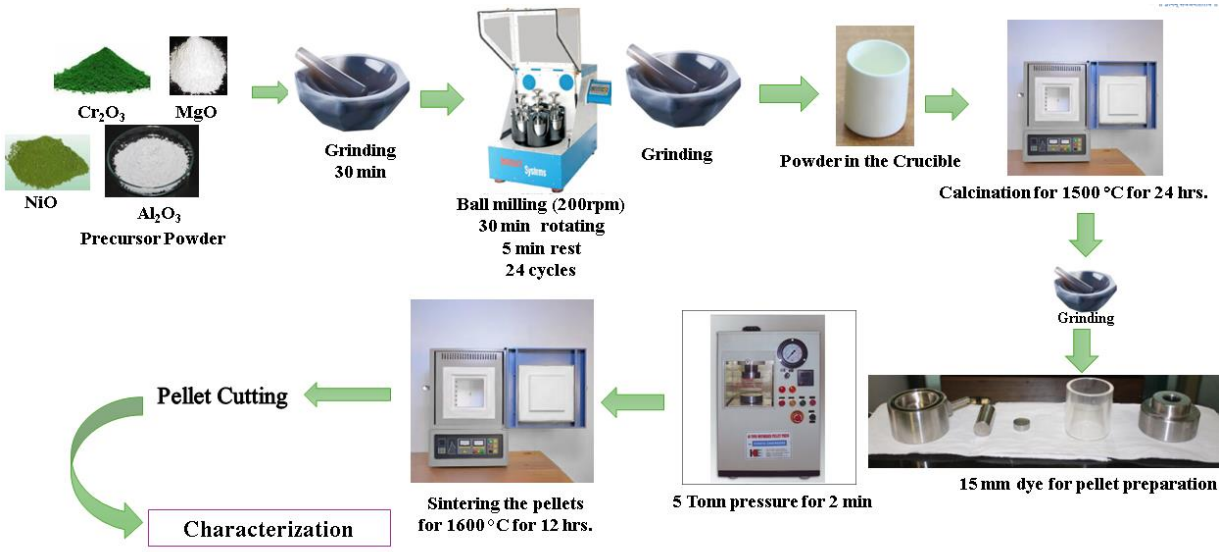

Figure 3.1: Schematic of the solid-state synthesis

(a) Manual Grinding and Homogenization of Precursor

Firstly, according to the stoichiometric ratio, weighing of the samples was carried out, thereafter for homogenization of the weighed powder, manual mixing was done using a mortar and pestle. This manual powder grinding step provides initial homogenization mixing, and breaking the bulk particles and making them fine, which enhances the uniform distribution of precursor powder throughout. Moreover, this uniform distribution of powder particles at the very beginning stage is crucial as it facilitates uniform diffusion during high-temperature treatment and provides in the synthesis of pure sample [20].

(b) Planetary Ball Milling

In addition to the manual mixing, to further improve homogenise precursor mixing and particle refinement, the grounded powder was subjected to planetary ball milling in isopropyl alcohol (IPA), using zirconia balls as the grinding media. This, wet ball milling was carried out at 200 rpm with alternating cycles of 30 minutes of rotatory ball milling

and 5 minutes of rest, for a total duration of 13 hours. Hereby, the use of IPA as a liquid medium helps to minimizes heat generation and promotes deagglomeration along with better dispersion of particles during ball milling. Followed by the ball milling, the slurry was dried under ambient conditions to ensure the complete evaporation of IPA. The resulting fine and homogeneous powder is essential for producing phase-pure materials, this powder again grounded using mortar and pestle for 30 min.

(c) Calcination

The grounded powder was then transferred into alumina crucibles and kept for calcination in a programmable box furnace at 1500 °C for 24 hours, following the procedure reported by R. Jangir et al. for synthesizing single-phase polycrystalline α-$AlCrO_3$. Calcination is a thermal treatment process that involves heating solid materials to high temperatures, often below their melting points and in the presence of a limited supply of air or oxygen. This process plays an important role in driving off volatile components, including thermal decomposition and causing phase transitions. In this process, the reactant powders mix and react chemically with each other in the high-temperature atmosphere. Mixed samples are taken in the alumina cylindrical crucibles and put inside the furnace for calcination, as shown in Fig 3.1 The temperature program set for the box furnace is illustrated in Figure 3.2. Calcination plays a vital role in the solid-state reaction route and serves multiple critical purposes as it facilitates solid-state diffusion between the constituent oxides results in the creation of the targeted α-$AlCrO_3$ pure phase and removes volatile products [21].

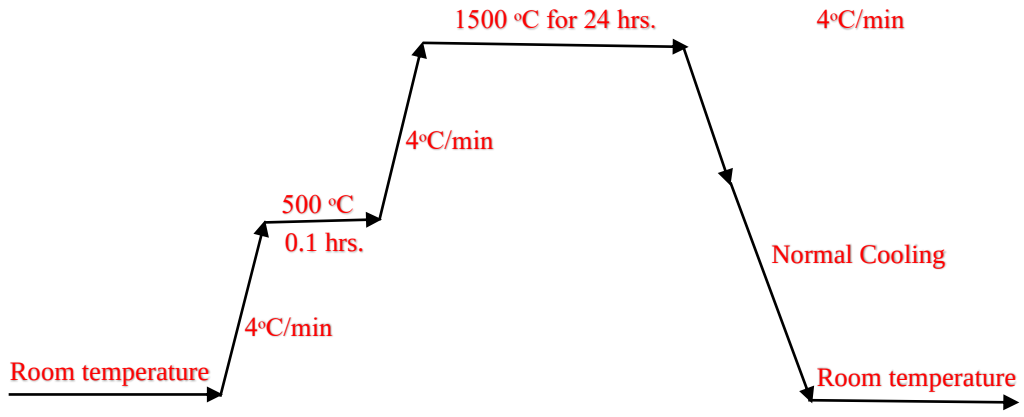

Figure 3.2: Schematic of the box furnace program to carry calcination.

The prolonged dwell time of 24 hours was chosen to guarantee sufficient diffusion and to avoid the formation of undesirable secondary phases such as spinel-type $NiCr_2O_4$ or $MgCr_2O_4$ impurities which can arise result of incomplete reaction conditions. After calcination, the resulting material was naturally cooled and reground using a mortar and pestle. This step eliminates any large agglomerates formed during calcination and improves powder uniformity helps not having any cracks while making pellet preparation.

(d) Pellet Making for Sintering

To improve the mechanical strength of the pellets during handling, two drops of polyvinyl alcohol (PVA) (3 wt% PVA in DI water) solution were added to the calcined powder. PVA acts as a temporary binder, which helps to hold the powder particles together and provides sufficient strength before sintering. It is widely used in solid synthesis processing because it evaporates completely during heating around at 500°C in box furnace for 4 hrs leads without leaving any residue or affecting the chemical composition of the material [54]. The binder mixed powder was then pressed into circular pellets with a diameter of 15 mm using a uniaxial hydraulic press. A pressure of 5 tons was applied for 2 minutes using a steel dye to ensure proper compaction. Uniform and sufficient pressing is important to achieve consistent density, reduce the chances of cracks, voids, or surface defects, and prepare the pellets for high-temperature sintering. Thereby, the pellets underwent sintering at 1600°C for a duration of 12 hours in a box furnace as shown in Figure 3.3. This sintering step important as it promotes densification of particle and crystal growth, this temperature and time ensure that forms completely without any secondary phases. After sintering, the top and bottom portions of the pellets were carefully cut off using a diamond cutter. These outer surfaces were likely in contact with the alumina crucible during high-temperature treatment and may have experienced diffusion small amount of alumina at the surface and may have contamination at the top and bottom side. To ensure the accuracy and reliability

of the characterization results, both the upper and lower faces of the pellets were polished to remove any impurities, uneven textures, or surface defects.

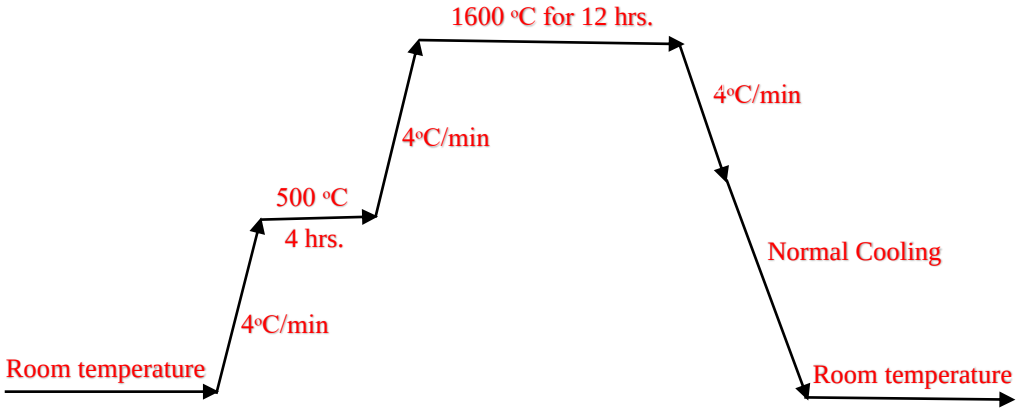

Figure 3.3: Schematic of the box furnace program to carry sintering.

The central region of each pellet, which was expected to be the most uniform was then sliced into thin discs of approximately 0.65 mm thickness. These thin and polished samples were used for various characterization techniques, including synchrotron-based X-ray diffraction (XRD), complex impedance spectroscopy (CIS), diffuse reflectance spectroscopy (DRS), Seebeck coefficient measurements, and photoelectron spectroscopy (PES). Maintaining uniform thickness and a smooth surface is essential to ensure reproducibility in all measurements and to avoid any inconsistencies caused by surface roughness or contamination, especially in optical and electrical characterizations.

3.3 Characterization Techniques

3.3.1 Synchrotron-Based Powder X-ray Diffraction (XRD)

X-ray diffraction (XRD) is employed to investigate crystal structures, detect different phases, and measure lattice parameters in crystalline materials. In this study, XRD measurements were employed to confirm the phase formation of single phase polycrystalline $AlCrO_3$ phase and to analyse structural changes induced by Ni- and Mg-doping. High-resolution powder XRD patterns were obtained using synchrotron radiation of Beamline-11 (Extreme Conditions Angle Dispersive/Energy Dispersive XRD) at the Indus-2 synchrotron source, located at the Raja Ramanna Centre for Advanced Technology (RRCAT), Indore, M.P., synchrotron equipped with a 1.5 T bending magnet, and the synchrotron ring operates at an electron energy of 2.5 GeV with a peak current of 200 mA,

and a beam lifetime of approximately 24 hours, offering a stable and intense X-ray source ideal for structural studies. A Si (111) channel-cut monochromator was employed to select the desired monochromatic X-ray wavelength from the synchrotron's white light. The selected beam was focused onto the capillary-mounted powder sample using a Kirkpatrick-Baez (K-B) mirror, which ensures optimal beam convergence and intensity. The powdered sample was filled into capillaries and exposed to synchrotron radiation of wavelength 0.4895 Å. A MAR345 area detector was utilized to record the two-dimensional diffraction images.

To ensure accurate data interpretation, calibration of the sample-to-detector distance and the incident wavelength was performed using NIST standard reference materials CeO_2. The resulting 2D diffraction images were processed and integrated into 1D intensity Vs 2θ (degrees) profiles using FIT2D software, which enabled further analysis of unit cell dimensions and peak positions.

3.3.2 Le-Bail Fitting Analysis

The Le-Bail fitting technique was used to refine the lattice parameters extracted from the powder diffraction profiles. Unlike the Rietveld refinement, Le Bail fitting does not require an assumed structural model, making it particularly advantageous for systems where the extract crystal structure may be unknown or partially understood. It focuses on fitting the observed diffraction peak positions and intensities to extract unit cell parameters with high precision. The analysis involves indexing the peaks, determining the space group symmetry based on systematic absences and reflection conditions, and refining the unit cell parameters by matching the calculated pattern with the observed diffraction data. The obtained data of XRD patterns all samples were analysed using FullProf software, with Le bail fitting. The structure model used was rhombohedral corundum (space group R-3c). The lattice parameters (*a* and *c*), and weighted profile (R_{wp}) were less than 10% and χ^2 values nearly 1 to ensure fitting reliability. Refined lattice parameters were noted for each sample, and systematic changes in cell dimensions with doping were analysed to confirm successful substitution at the Al site.

3.3.3 Diffuse Reflectance Spectroscopy (DRS)

DRS is a widely used optical characterization technique for analysing materials that are difficult to study using conventional absorption or transmission methods [22]. In this work, DRS was employed to investigate the optical absorption behaviour and band structure modifications induced by Ni- and Mg-doping in $AlCrO_3$. The measurements were carried out on pellets that had been finely ground and polished, utilizing a UV-Vis-NIR spectrophotometer equipped with an integrating sphere to capture diffusely reflected light over the 200-1200 nm wavelength range. When light interacts with a material, it may be absorbed, transmitted, or reflected; diffuse reflectance spectroscopy (DRS) specifically examines the portion of light scattered in multiple directions from the sample surface. The resulting DRS data are interpreted using the Kubelka-Munk function, which links the diffuse reflectance to the material's absorption and scattering properties. Unlike standard transmission spectroscopy, where the band intensity directly correlates with concentration, DRS does not exhibit a straightforward linear relationship between reflected intensity and concentration. As a result, the Kubelka-Munk equation provides an empirical approach to relate the concentration to the intensity of diffusely reflected light, making quantitative analysis possible. The Kubelka-Munk equation [23] is expressed as:

$$f(R_\infty) = \frac{(1 - R_\infty)^2}{2R_\infty} = \frac{C}{k} = \frac{K}{s} \qquad 3.3$$

Here, C denotes the sample concentration, K represents the absorption coefficient, S is the scattering coefficient, and $f(R_\infty)$ refers to the Kubelka–Munk function. R_∞ stands for the absolute reflectance of the sample layer, which is measured as the ratio of the sample's diffuse reflectance to that of a non-absorbing reference such as KBr or KCl at a depth where further increases do not affect the reflectance. The molar absorption coefficient (k) is related to the proportion of light transmitted through the sample, while the scattering coefficient corresponds to the fraction of light scattered diffusely. This analysis allowed for the evaluation of bandgap changes due to doping [24], and for understanding the modification of the electronic structure with substitutional incorporation of Ni^{2+}or Mg^{2+} at the Al^{3+} site.

3.3.4 Complex Impedance Spectroscopy (CIS)

The CIS method was utilized to study the electrical transport characteristics of both undoped and doped $AlCrO_3$ a wide bandgap semiconductor. CIS is a widely used technique for analysing frequency-dependent electrical behaviour in ceramics, as it enables distinguishing the effects of grains, grain boundaries, and electrodes effects [25]. In this study, CIS measurements were performed on polished 0.65 mm thick pellets to analyze the electrical properties on all synthesized compositions, including ACO (undoped), ACONi05 to ACONi20, and ACOMg05 to ACOMg20. Prior to measurements, silver paste was applied on both surfaces, one side fully coated, the other in a defined circular contact region (~2.5 mm radius). The pellets were then dried at 400°C for 4 hours to ensure proper adhesion of the silver electrodes. The measurements were conducted using a precision LCR meter in the frequency range of 100 Hz to 1 MHz, across a temperature range from room temperature up to 90 K to ~480 K. Low temperature was achieved by using liquid nitrogen, and frequency-dependent measurements were recorded across the temperature range. The pellets were placed in a custom-built sample holder and maintained vacuum of $\sim 3.2\times10^{-3}$ mbar.

The complex impedance data were recorded in terms of real (Z') and imaginary (Z'') components of the impedance. From this, Nyquist plots (Z'' vs Z'), Z'' vs frequency plots, and electric modulus (M'') vs frequency plots were generated to analyse relaxation dynamics and conduction mechanisms. The total impedance response was interpreted using both impedance (Z) and electric modulus (M) formalisms to separately assess grain and grain boundary contributions [3]. To extract the resistance and capacitance parameters of the materials, the data were fitted using equivalent circuit models, and constant phase element (CPE) combinations for grain and grain boundary regions. Fitting was performed using EC-Lab software. The temperature-dependent resistance values (R) and relaxation frequencies (f_{max}) were further analysed using the Arrhenius relation to calculate the activation energy (E_a) for the conduction process [25].

This approach enabled a comprehensive evaluation of the electrical charge transport behaviour and confirmed the influence of Ni and Mg doping on grain conductivity, grain boundaries, and relaxation dynamics.

3.3.5 Seebeck Coefficient Measurement

This method relies on the thermoelectric (Seebeck) effect to identify whether a semiconductor material exhibits *p*-type or *n*-type conductivity. The principle behind determining the type of semiconductor using the thermoelectric effect hinges on the nature of charge carriers in the materials. In our work, two probes, a hot probe and a room temperature (Cold) probe, are placed on the semiconductor surface. The hot probe creates a temperature gradient, which makes charge carriers move towards different probes and leads to the generation of voltage differences between the probes. The polarity of this voltage is important to determine the type of charge carrier present in the semiconductor. A positive voltage at the hot probe indicates a *p*-type material, while a negative voltage at the hot probe suggests as an *n*-type material. The relationship between generated voltage (V), Seebeck coefficient (S), and the temperature difference (ΔT) is

$$V = S \times \Delta T \tag{3.4}$$

The Seebeck coefficient varies depending on the doping in the material [26]. Being the simplicity of the technique, the hot probe method is a powerful tool in semiconductor research and device fabrication using a *p*-*n* junction. Also, accuracy in this technique depends on the uniformity of the material, precise control of the temperature gradient, and sensitivity of the voltage measurements.

3.3.6 Photoelectron Spectroscopy (PES)

Photoelectron spectroscopy is employed to examine the electronic structure of material. In our work, the sample material is bombarded with photons, and electrons are emitted from the surface of the sample with some kinetic energy. The energy of these emitted electrons is directly related to their binding energies within the materialwhich reveals' details about the surface's electronic structure and elemental composition. The binding energy is a unique identifier of each element and the chemical state and is calculated using expression: [27]

$$E_{binding} = hv - E_{Kinetics} - \phi \quad 3.5$$

where, Φ is the spectrometer's work function, $E_{kinetic}$ is is the kinetic energy of the emitted photoelectron. With the advancement in technology, PES has witnessed improvements in photon sources such as synchrotron radiation, which provides a broad spectrum of high-intensity light, which not only enhances the resolution but also leads to an increase in the sensitivity of the technique.

Chapter 4

Results and Discussion of Ni-Doped $AlCrO_3$

4.1 Introduction

As highlighted in the previous chapter, systematic studies focusing on *p*-type doping in Aluminum Chromium Oxide (α-$AlCrO_3$) remain unexplored. Driven by the objective of discovering new and efficient *p*-type TCO materials, the present research was structured around clearly defined objectives. This chapter is dedicated to Objective 1, which involves synthesizing and comprehensively characterizing Ni-doped α-$AlCrO_3$ ($Al_{1-x}Ni_xCrO_3$) through the solid-state reaction method. Subsequent sections of this chapter provide detailed investigations into how nickel incorporation influences the structural, optical, and electrical characteristics of α-$Al_{1-x}Ni_xCrO_3$. We employed SXRD for structural analysis, Le-Bail fitting for lattice parameter extraction, CIS for electrical properties, DRS for optical properties, Seebeck coefficient measurements for confirming *n*-type or *p*-type semiconductors, and PES to investigate electronic structures.

Nickel was specifically selected as the dopant primarily because of its divalent state (Ni^{2+}), which can introduce acceptor states when doping for the trivalent aluminum ions (Al^{3+}) in the α-$Al_{1-x}Ni_xCrO_3$ crystal lattice. Additionally, the ionic radius of Ni^{2+} (0.69 Å) is intermediate between those of Al^{3+} (0.54 Å) and Cr^{3+} (0.76 Å). This favorable ionic size compatibility facilitates effective solubility of nickel within the corundum-structured α-$Al_{1-x}Ni_xCrO_3$ lattice, thereby minimizing structural distortions or lattice strain.

To systematically evaluate the impact of Ni-doping, compositions represented by the general formula α-$Al_{1-x}Ni_xCrO_3$ were synthesized, with varying Ni-doping concentrations of x = 0, 0.005, 0.01, 0.015, and 0.02. These samples are referred to hereafter as ACO, ACONi05, ACONi10, ACONi15, and ACONi20, respectively. The synthesis was conducted via the solid-state reaction route, as previously outlined in detail in Chapter 3. The findings discussed throughout this chapter will offer insights into the relationship between nickel doping concentration and the resulting changes in structural and electrical properties that ultimately enhance our understanding of α-$Al_{1-x}Ni_xCrO_3$ as a promising candidate for *p*-type candidate for TCOs and optoelectronic applications.

4.2 Synchrotron-based X-Ray Diffraction (SXRD) Analysis

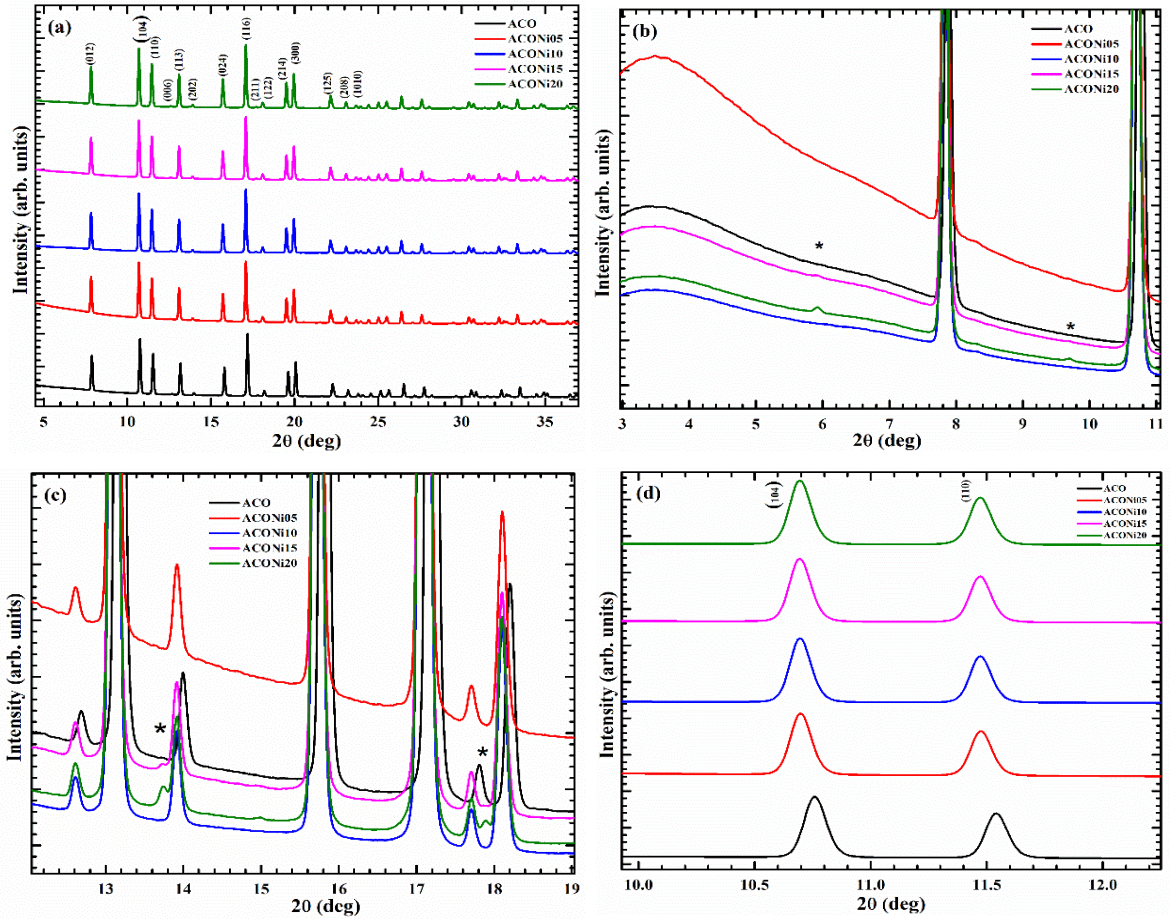

Figure 4.1: X-ray Diffraction (XRD) Analysis of α-$Al_{1-x}Ni_xCrO_3$

To investigate phase formation and crystal structure in the series of Ni-doped α-$AlCrO_3$ i.e., α-$Al_{1-x}Ni_xCrO_3$ (x = 0.00, 0.005, 0.01, 0.015, and 0.02) SXRD data were recorded, using a monochromatic beam with wavelength of 0.4895Å on beamline BL-11 of the Indus-2 synchrotron source (RRCAT, Indore). Figure 4.1 shows the diffraction patterns of α-$Al_{1-x}Ni_xCrO_3$ compositions ($0 \leq x \leq 0.02$), which are indexed to a rhombohedral R-3c space group, consistent with previous reports with α-$AlCrO_3$ [19].

No secondary diffraction peaks were observed up to x = 0.01, revealing that the successful incorporation of Ni^{2+} into the Al-site within the solubility limit. However, for x > 0.015, weak secondary phases (marked with asterisks symbol "*") emerged in the diffraction pattern, may be due to solubility limit or phase segregation effects. Despite these trace impurities, the major diffraction peaks are still representative of the R-3c lattice,

showing that the corundum structure still exists and that Ni^{2+} has been incorporated into the $AlCrO_3$ matrix successfully.

Figure 4.1 (b-c) shows magnified regions of minor secondary peaks observed at a higher doping level, possibly arising from secondary peaks. Figure 4.1(d) observed that peak shift towards lower 2θ values with increasing Ni^{2+} doping concentration. A systematic leftward shift in Bragg reflections such as (104) and (110) was observed with increasing Ni^{2+} content and this peaks shift is attributed to the substitution of smaller Al^{3+} ions (0.54 Å, VI coordination) by slightly large Ni^{2+} ions (0.69 Å, VI coordination), which induces local strain and lattice distortion.

4.2.1 Le-Bail Fitting Analysis

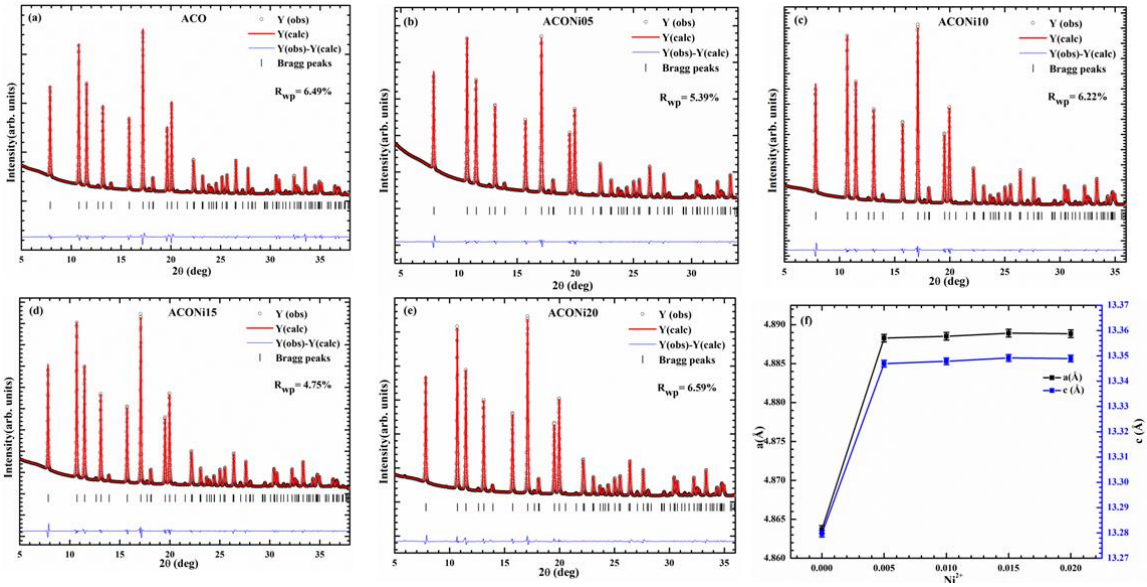

Figure 4.2 (a-e): Le-Bail fitting profile of synchrotron XRD data for α-$Al_{1-x}Ni_xCrO_3$, x = 0.00, 0.005, 0.01, 0.015, and 0.02) samples using FullProf suite software. The fitting confirms the R-3c phase group across all doping compositions. (f) Variation of refined lattice parameter (a, c) as a function concentration in α-$Al_{1-x}Ni_xCrO_3$.

To quantify the structural changes due to Ni doping Le-Bail fitting [28] was performed using FullProf Suite software [29]. The fitting was carried out by assuming the R-3c phase group, with constraints $\alpha = \beta = 90°$, $\gamma = 120°$, and $a = b \neq c$, for all compositions in the α-$Al_{1-x}Ni_xCrO_3$ series. Figure 4.2 (a-e) displays Le-Bail fitting profiles for all samples. The refinement carried out provided excellent agreement between calculated and

experimental data, yielding R_{wp} values below 10% and χ^2 values close to unity, validating the good-fit to the structural model with no evidence of structural phase transitions. The small impurity peaks observed earlier did not significantly affect the quality of the refinement. The lattice constants 'a' and 'c' were obtained through Le-Bail refinement and plotted against Ni^{2+} content, as illustrated in Figure 4.2(f). And it was clearly observed an increase of lattice parameter with the incorporation of Ni^{2+} doping. This is significantly due to the larger ionic radius of Ni^{2+} compared to Al^{3+} and confirms the expected lattice expansion due to the ionic size mismatch.

4.3 Diffused Reflectance Spectroscopy (DRS) Analysis

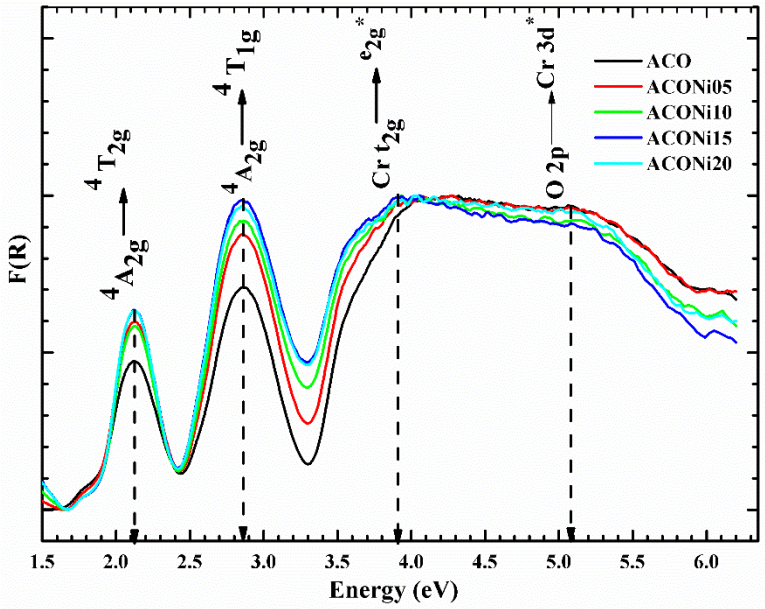

Figure 4.3: DRS of α-$Al_{1-x}Ni_xCrO_3$ plotted as a function of Kubelka-Munk versus Energy (eV) for all samples.

To understand the optical properties of synthesized material, the DRS analysis was carried out using Kubelka-Munk function, as mentioned in equation 3.3. Figure 4.3 displays the F(R) versus energy (eV) plot for all the samples, showing several distinct transitions in Ni-doped $AlCrO_3$ aligning with those reported by R. Jangir et.al in their study on optical structural properties of $AlCrO_3$ [3]. The absorption features detected at 2.11 eV, 2.86 eV, 4.05 eV, and 5.09 eV are attributed to the electronic transitions $^4A_{2g} \rightarrow {}^4T_{2g}$, $^4A_{2g} \rightarrow {}^4T_{1g}$, Cr $t_{2g} \rightarrow e_g^*$ and $O_{2p} \rightarrow$ Cr d*, and O 2p $\rightarrow$ Cr d*, respectively[30-31] It is widely recognized that the splitting of the d-orbitals in α-Cr_2O_3 leads to an optical band gap of

approximately 3.4 eV [30,31]. However, with the substitution of Al, the absorption peak was observed at ~4.05 eV in DRS spectra of α-$AlCrO_3$ (ACO)and Ni-doped α-$AlCrO_3$. It can be observed that all the peaks of corresponding to ACO and Ni-doped samples indicates that bandgap energy was unchanged. Furthermore, no shift in peak positions with increased Ni-doping in α-$AlCrO_3$ was observed, indicating that Ni-doping does not alter the electronic band structure.

4.4 Complex Impedance Spectroscopy (CIS) Analysis

To explore how the electrical properties change with both temperature and frequency, complex impedance spectroscopy (CIS) was performed on all samples. Measurements covered a frequency range from 100 Hz to 1 MHz and temperatures between 90 K and 480 K. CIS is a versatile method for probing the electrical behaviour of materials across broad frequency and temperature ranges [25]. This method is particularly useful for separating the effects of the bulk material, grain boundaries, and electrode interfaces within a system. However, interpreting data to differentiate between long-range conductivity (delocalized charge transport) and localized dipole relaxation remains challenging. Both localized and delocalized conduction mechanisms originate from bulk processes, resulting in identical geometric capacitance values. To address ambiguity, the imaginary impedance component (Z'') is particularly useful for identifying resistive pathways (e.g., grain boundaries), while the imaginary modulus component (M'') excels in highlighting localized relaxation phenomena.

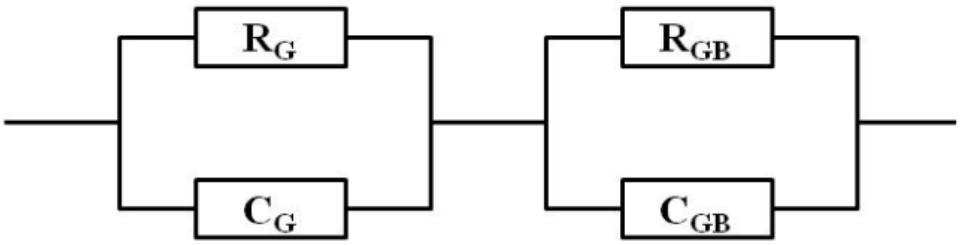

Figure 4.4: Schematic representation of an equivalent circuit illustrating the distinct electrical responses of grains and grain boundaries in polycrystalline materials.

The total impedance (Z*) corresponding to the circuit shown in Figure 4.4 can be expressed as follows:

$$Z^* = Z' + jZ'' \qquad 4.1$$

$$= \left(\frac{1}{R_G + j\omega C_G}\right)^{-1} + \left(\frac{1}{R_{GB} + j\omega C_{GB}}\right)^{-1}$$

where, R_G and R_{GB} represent the DC resistances of grains and grains boundaries, respectively, while C_G and C_{GB} denote the corresponding capacitance.

The real (Z') and imaginary (Z") components of the CIS data can be determined as:

$$Z' = \frac{R_G}{1 + (\omega R_G C_G)^2} + \frac{R_{GB}}{1 + (\omega R_{GB} C_{GB})^2} \qquad 4.2$$

And

$$-Z'' = R_G\left(\frac{\omega R_G C_G}{1+(\omega R_G C_G)^2}\right) + R_G\left(\frac{\omega R_{GB} C_{GB}}{1+(\omega R_{GB} C_{GB})^2}\right) \qquad 4.3$$

The electric modulus (M*) is related to the complex impedance (Z*) by the following relationship:

$$M^* = j\omega C_0 Z^* \qquad 4.4$$

where, C_0 represents the geometrical capacitance, also known as vacuum capacitance. The real (M') and imaginary (M'') parts of the complex modulus are derived as:

$$M' = \frac{C_0}{C_G}\left(\frac{(\omega R_G C_G)^2}{1 + (\omega R_G C_G)^2}\right) + \frac{C_0}{C_{GB}}\left(\frac{(\omega R_{GB} C_{GB})^2}{1 + (\omega R_{GB} C_{GB})^2}\right) \qquad 4.5$$

And for the imaginary component:

$$M'' = \frac{C_0}{C_G}\left(\frac{(\omega R_G C_G)}{1 + (\omega R_G C_G)^2}\right) + \frac{C_0}{C_{GB}}\left(\frac{(\omega R_{GB} C_{GB})}{1 + (\omega R_{GB} C_{GB})^2}\right) \qquad 4.6$$

To obtain complete information about the studied material, it is essential to determine the value of each component (R and C) in the circuit. A combination of the impedance and modulus formalisms is used to achieve these values in the best manner. Each parallel RC element is represented by a semicircle in the complex plane (Z'' vs. Z'; M'' vs. M') and appears as a Debye peak in the spectroscopic plot of the imaginary component (Z'', M'' vs. log f). The frequencies corresponding to the peak maxima in the plots of M'' and Z'' are governed by the following equation:

$$2\pi f_{max} RC = 1 \qquad 4.7$$

In the Nyquist plots of Z'' vs. Z', two semicircles can be observed, corresponding to different elements of the circuit. The semicircle associated with the grain boundaries which is typically larger than that for the bulk (grains). Impedance plots give the most emphasis

to the elements with the largest resistance (grain boundaries), whereas modulus plots highlight those elements with the smallest capacitances (grain).

In the Z″ vs frequency plots were plotted for all the samples as shown in Figure 4.5. Notably, in undoped $AlCrO_3$ (ACO) sample, only a single dominated relaxation peak is observed throughout measured temperature and frequency range. This pattern suggests that a dominant conduction mechanism is primarily responsible for the observed dielectric relaxation process, which is largely influenced by the presence of grain boundaries in the material [32]. This type of conduction mechanism can be understood by short-range conduction mechanisms that occur because of localized movement of charge carriers over atomic-scale distances. Small polaron can be associated due to different mechanisms such as the hopping between adjacent sites or local dipole orientations, or defect dipole relaxations. In undoped ACO available charge carrier transport dominated by small polaron which is highly localized, resulting in short-range hopping conduction confined to grain boundaries. These regions act as potential barriers that dominate the overall impedance response, while the bulk region remains highly resistive and electrically inactive over the accessible frequency range for undoped sample. On other hand, Ni-doping in $AlCrO_3$ that is $Ni^{2+} \rightarrow Al^{3+}$ sites, lead to localized charge imbalance. This imbalance is often compensated by changing of Cr^{4+} oxidization state, which acts as donor-type defects. These defects increase the density of available charge carriers and lower the potential barrier at the grain boundaries. More importantly, they also enhance the electronic overlap between Cr 3d and O 2p orbitals, enabling long-range carrier delocalization through polaron hopping across multiple lattice sites which is nothing but long-range conductions. This occurs because of charge transport over multiple atomic distances including across grains. The Ni-doped samples display two distinct Z″ peaks, the low-frequency peak remains associated with grain boundary conduction, while the high-frequency peak emerges due to enhanced bulk (grain) conductivity respectively.

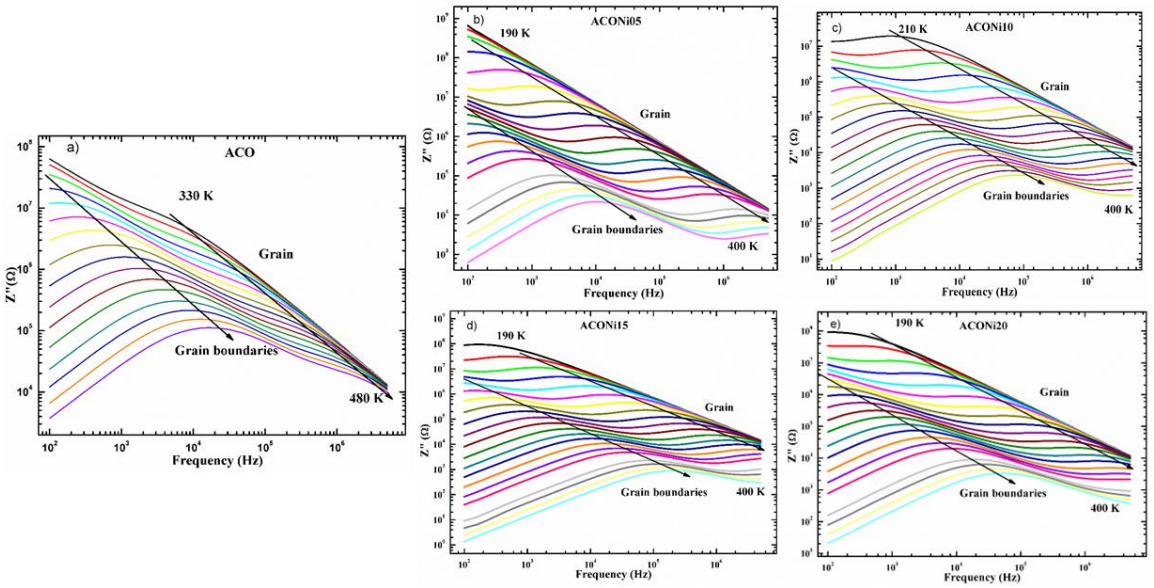

Figure 4.5 (a-e): Frequency-dependent imaginary(Z") plot for ACO, ACONi05, ACONi10, ACONi15 and ACONi20 samples at various temperature, showing characteristic peaks shifting shifts toward higher frequencies as the temperature rises.

To understand the effect of temperature dependance/independence of relaxation times, scaling analysis of impedance plotted as shown in Figure 4.6. The imaginary part of impedance Z" was normalized with its respective peak value (Z''/Z''_{max}), and frequency was scaled with the corresponding peak frequency (f/f_{max}) for each temperature. t was found that, across the entire temperature range studied, all the normalized Z″ spectra overlapped and formed a single master curve. This temperature-independent master curve strongly suggests that the underlying relaxation dynamics are governed by a single mechanism, independent of thermal excitation [33]. Thereby, the fundamental charge transport mechanism remains the same while the characteristic relaxation time varies with temperature. The formation of a master curve implies that Ni-doping does not alter the type of carrier relaxation mechanism but rather affects its rate through structural and electronic modifications such as lattice parameters and carrier density.

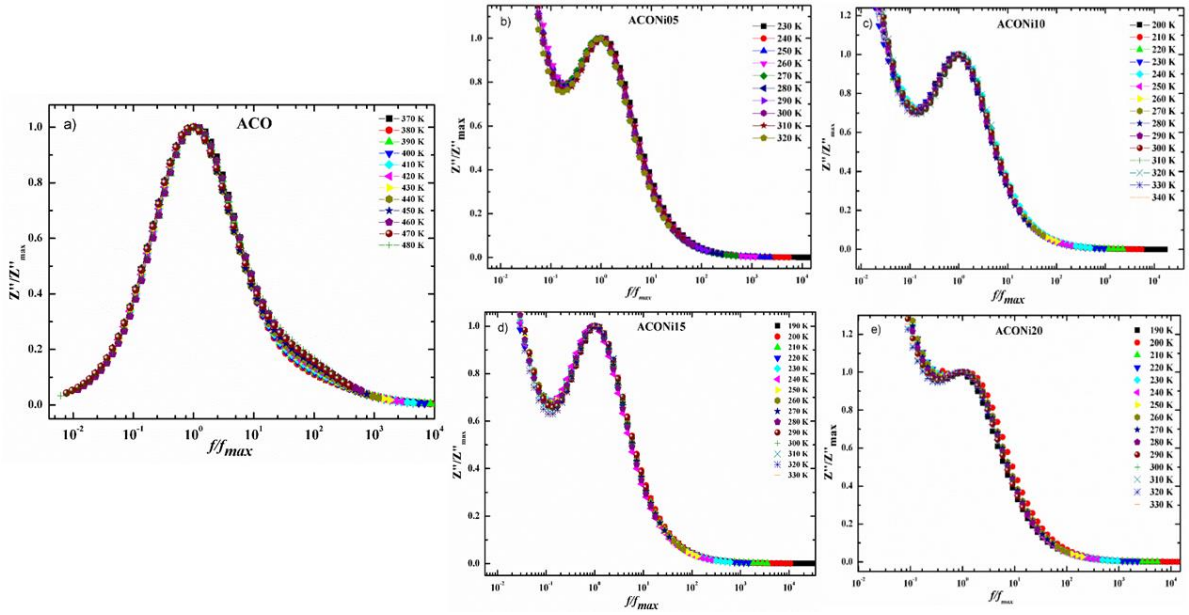

Figure 4.6 (a-e): Scaled Z"/Z"$_{max}$ versus f/f_{max} plot for the same undoped ACO and ACONi doped series, demonstrating temperature-independent relaxation behavior via perfect single master curve overlap.

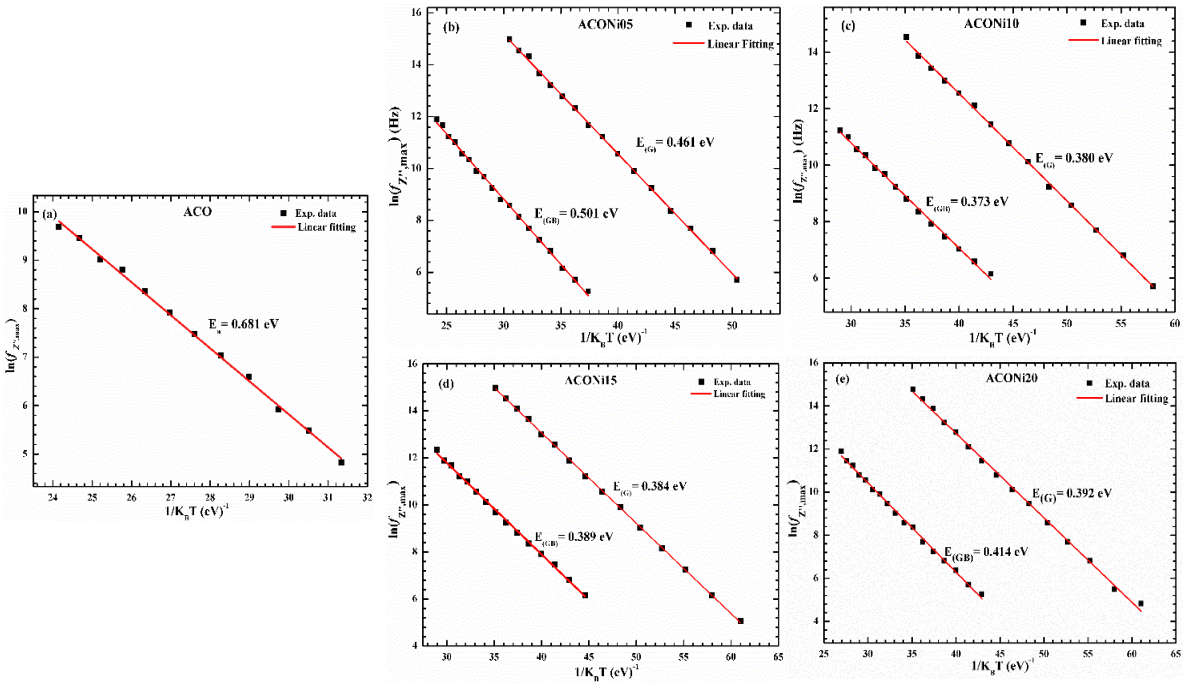

Figure 4.7 (a-e) : Arrhenius plots of ln(f_{max}) versus 1/K_BT derived from Z'' data, used to calculate activation energies for grain & grain boundaries contribution in Ni-doped ACO samples.

Activation is crucial parameter to understand the conduction mechanisms as it indicates energy barrier of charge carriers that must be overcome to participate in

conduction mechanisms. In this study as shown in Figure 4.7, E_a values were obtained for all samples corresponding to grain and grain boundaries by fitting the temperature dependence of the relaxation frequencies (f_{max}) corresponding to the peaks observed in the Z'' vs frequency plots. By plotting $\ln(f_{max})$ against $1/K_BT$ and fitting the data with the Arrhenius relation: $f_{max}=f_0\exp(-E_a/(K_BT)$, was linearized to $\ln(f_{max}) =\ln(f_0)-(E_a/K_B)(1/T)$, Here, f_0 denotes the pre-exponential factor, K_B stands for the Boltzmann constant, and T is the absolute temperature [34]. The slope of each linear fit directly provides the activation energy value, with the linearity of the plots confirming the thermally activated nature of the relaxation processes. This method is effective for clearly distinguishing and determining the activation energies associated with both grain and grain boundary conduction mechanisms.

For all Ni-doped samples, two peaks were observed in the Z" spectra, corresponding to grain and grain boundary relaxations respectively. Therefore, activation energy was separately obtained for both conduction mechanisms. The linearity of the fitting of the Arrhenius plots indicates that the relaxation mechanism follows a single thermally activated process over the measurement range. The activation energy of single relaxation in Z" spectra of ACO was obtained as 0.681 eV. The activation energy for grain relaxation of ACONi05, ACONi10, ACONi15 and ACONi20 obtained as 0.461 eV, 0.380 eV, 0.384 eV, and 0.414 eV, and for and grain boundary as 0.501 eV, 0.373 eV, 0.389 eV, and 0.414 eV, respectively. These results demonstrate a significant decrease in activation energy with Ni doping, especially up to x = 0.01. The decrease in activation energy reveals enhanced carrier mobility and hopping conduction. The slight increase of E_a at higher doping x = 0.015 and 0.02 may be attributed to defect interactions or limited solubility of Ni^{2+} in the lattice.

4.4.1 Modulus Impedance Spectroscopy

Modulus Spectroscopy is often useful for highlighting bulk (grain) relaxation processes, especially when the grain boundary capacitance dominates in the impedance spectra representation. The imaginary part of the modulus (M") suppresses the effect of large capacitances (like grain boundaries or electrodes) and emphasizes processes with smaller

capacitances (like bulk dielectric relaxations). The Figure 4.8(a-e) shows M″ vs frequency plots for the α-$Al_{1-x}Ni_xCrO_3$ samples (x = 0.0 to 0.02).

The complex electric modulus, defined as $M^*(\omega) = j\omega C_0 Z^*(\omega)$, where C_0 is geometrical vacuum capacitance and $\omega = 2\pi f$ is the angular frequency, serves as a powerful technique for probing the dielectric relaxation and charge conduction mechanism within materials. It was initially introduced to study the space charge relaxation phenomena [35], and it has since become a standard method for analyzing ionic conductivities, particularly for polycrystalline materials. The electric modulus M* formalism provides effective representation of the intrinsic dielectric relaxation process and more particularly those associated with the grain (bulk) material, by minimizing the influence of grain boundary and electrode polarization effects.

The complex electric modulus, M*(ω), is mathematically described as:

$$M^* (\omega) = M' (\omega) + j\, M'' (\omega) \qquad 4.8$$

where M'(ω) represents the real part and M''(ω) corresponds to the imaginary part of the electric modulus.

In impedance spectroscopy, the height of each peak in the Z″ versus frequency plot is directly related to the resistance (R) of the corresponding RC circuit element. This relationship allows for the identification and quantification of different resistive contributions within the material, such as those from grains, grain boundaries, or electrodes. Moreover, the modulus spectroscopy M" vs frequency (*f*) plots are proportional to the reciprocal of the capacitance (1/C) for that RC circuit element. Therefore, the fundamental difference, while in impedance plots emphasize features associated with high resistance elements, whereas the modulus plots emphasize the elements with lower capacitance, more typically bulk (grain) response of the material. By analyzing the spectrum, both "grain" and "grain boundary" impedances can be effectively separated [36-40]. The modulus spectroscopy effectively suppresses information concerning grain boundaries (and electrodes) effects, which generally have large capacitance compared to the bulk. This makes it an essential tool for focusing on bulk (grain) properties.

To further analyze these characteristics, temperature-dependent M” vs *f* plotted as shown in the Figure 4.8(a-e) for α-$Al_{1-x}Ni_xCrO_3$ samples (ACO, ACONi05, ACONi10, ACONi15, and ACONi20). The prominent relaxation peak confirms the presence of conductivity relaxation process is thermally activated. The peak frequency position shifts to higher frequency with the rise of temperature, providing insights into the transitions from the short-range localized motion to long-range conduction of charge carriers. In the low frequency range, charge carriers possess sufficient energy to hop between adjacent lattice sites, thereby providing the long-range conduction across the grains (bulk). At higher frequencies, charge carriers are restricted to their local potential wells, allowing only limited, localized movement rather than long-range conduction [41][42].

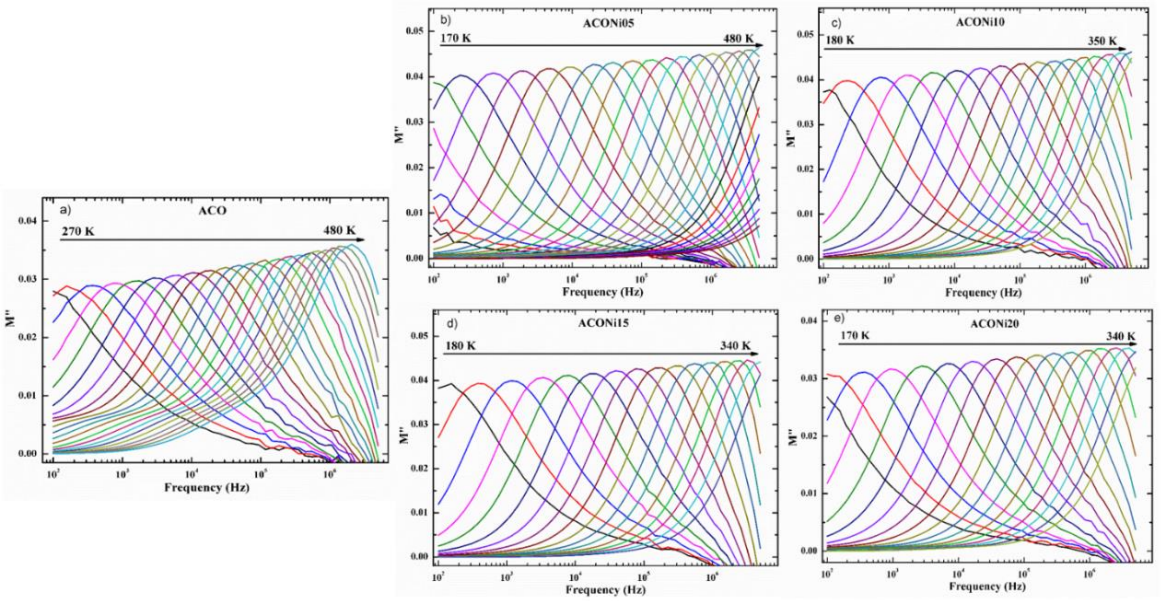

Figure 4.8(a-e): shows the M” plotted across a spectrum of temperatures plotted against frequency for α-$Al_{1-x}Ni_xCrO_3$ samples (ACO, ACONi05, ACONi10, ACONi15, and ACONi20).

4.4.2 M″ Scaling Behaviors Spectra: M″/M″$_{max}$ vs f/f_{max} Master Curve

The imaginary component of the electric modulus, M’’, was divided by its maximum value, M’’$_{max}$, and the frequency axis was adjusted relative to the peak frequency, f_{max}, at each temperature. The resulting master curves, presented in Figure 4.9 (a-e), show the plots of M”/M”$_{max}$ versus f/f_{max} for all samples across the measured temperature range. The complete overlapping of curves at different temperatures for each composition depicts a temperature-independent relaxation mechanism. This overlap confirms that the distribution of relaxation times and the shape of the relaxation function

remain unchanged, although the absolute values of relaxation time and peak frequency shift with temperature as expected for thermally activated processes. In other words, the microscopic mechanism responsible for dielectric relaxation is likely due to thermally activated hopping of localized charge carriers remaining the same throughout the studied temperature range. Moreover, the shape of the normalized M" spectra appears symmetric and relatively narrow, revealing that a quasi-Debye type relaxation mechanism, typically indicative of a well-defined potential landscape for charge carriers within the grains, is dominant. This observation is consistent with the earlier impedance analysis that revealed well-separated grain and grain boundary responses and supports the idea that modulus formalism effectively extracts the bulk (grain) contribution. From the master curve, further the hypothesis that Ni-doping enhances carrier mobility without introducing new relaxation mechanisms. Instead, it modifies the relaxation mechanisms frequency and activation energy by altering the defect landscape originated by Cr^{3+}/Cr^{4+} oxidation state, while preserving the underlying relaxation dynamics. Such behavior is often observed in perovskite and corundum-type oxides where aliovalent doping leads to improved charge transport without disrupting the electronic structure [17]. In summary, the modulus scaling behavior provides compelling evidence that the dielectric relaxation in Ni-doped $AlCrO_3$ is governed by a single, thermally activated mechanism, consistent with hopping conduction in the bulk phase. The activation energies associated with the conduction process in the material were obtained from the modulus (M") spectra. Figures 4.10 (a-e) present the Arrhenius fitting of the $\ln(f_{M"max})$ versus $1/K_BT$ plots, which was used to extract the activation energy related to the relaxation behaviour. Samples ACO, ACONi05, ACONi10, ACONi15, and ACONi20 show only one peak (Figure 4.7) in the M'' versus *f* spectrum with the activation energies of 0.545 eV, 0.451 eV, 0.0.354 eV, 0.365 eV and 0.379 eV respectively. Activation energy drastically decreased upon doping up to $x = 0.01$ and slight increase in E_a observed with higher doping.

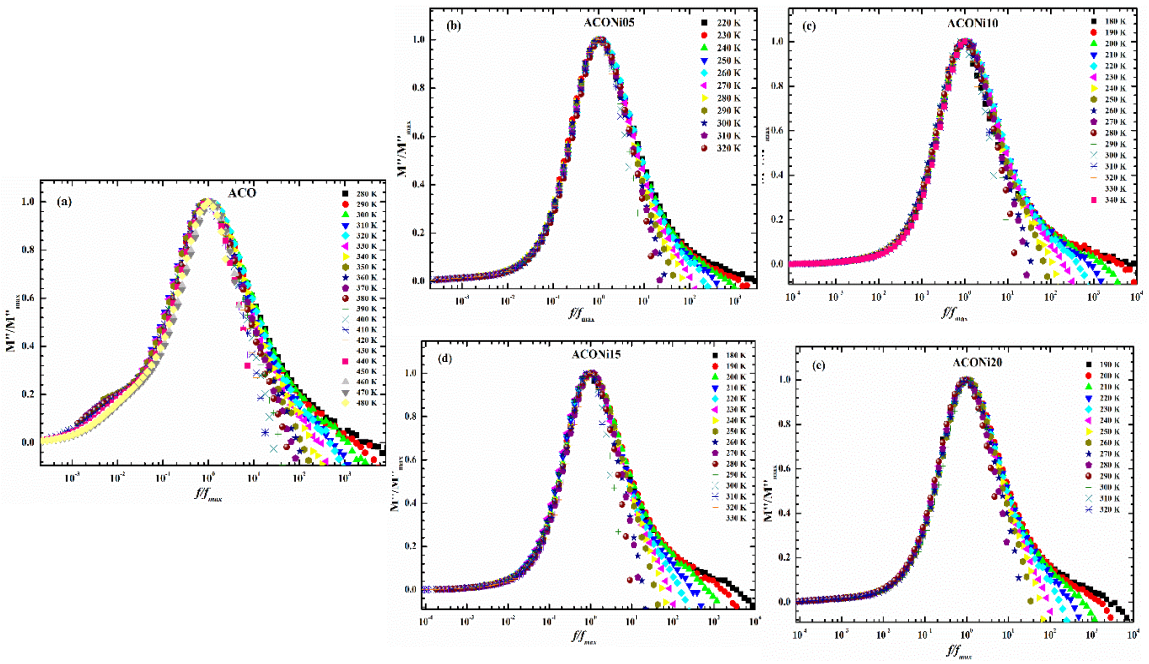

Figure 4.9(a-e): Scaling characteristics in the imaginary electric modulus spectral analysis i.e., M"/M"$_{max}$ vs f/f_{max} for all α-$Al_{1-x}Ni_xCrO_3$ samples (ACO, ACONi05, ACONi10, ACONi15, and ACONi20).

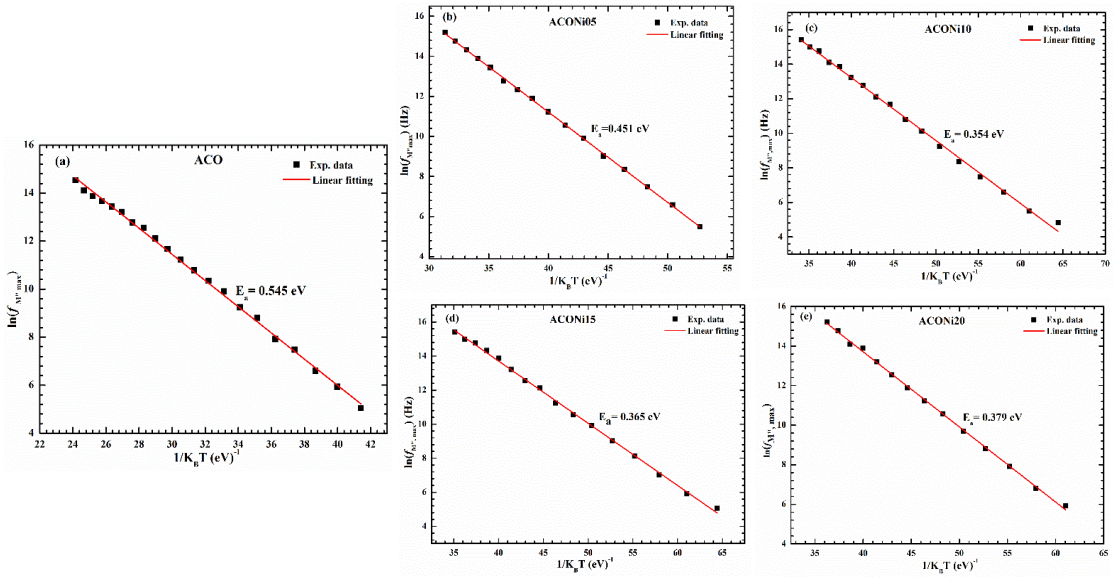

Figure 4.10 (a-e): Arrhenius plots of ln(f_{max}) versus 1/K_BT derived from M'' spectra for all α-$Al_{1-x}Ni_xCrO_3$ samples (ACO, ACONi05, ACONi10, ACONi15, and ACONi20).

4.4.3 Nyquist Plot Analysis

Nyquist plots (Z" vs Z") plots were plotted for wide range of temperature for all the samples as shown in Figure 4.11 (a-e), the resulting curves exhibit two semicircular arcs

for all compositions except the undoped sample. The high-frequency arc is attributed to the response of the grain (bulk), whereas the low-frequency arc, which becomes more prominent at elevated temperatures, is associated with grain boundaries. This dual arc behavior clearly indicates that the dielectric relaxation is governed by two separate mechanisms, one arising from the bulk and the other from grain boundaries.

To further assess the relaxation charge transport mechanism nature, the curves at each temperature were scaled relative to the high-frequency arc of the lowest-temperature plot. Notably, all the Nyquist curves across different ranges of temperatures collapsed into a single master curve after normalization. This implies that the relaxation mechanism remains temperature-independent, and only the time constants shift due to thermal activation. Such overlapping behavior is a strong indication that the material follows a consistent conduction mechanism, which can be modeled reliably across the full temperature range.

The presence of two arcs with asymmetrical curves also suggests that relaxation behavior deviates from an ideal Debye response. For an ideal Debye-like behavior, each relaxation process would correspond to a perfectly symmetrical semicircle with a single, well-defined time constant. In the present case, two peaks were observed, and this behavior required the use of a more flexible model to account for non-ideal dielectric behavior. To model such behavior with the equivalent circuit, with a constant phase element. In this, each curve associated with grain and grain boundaries will be modelled as a parallel combination of resistance and capacitance. The two CPE elements, one of the grains and the other of the grain boundaries, are connected in series to reflect the total polycrystalline material.

The CPE accounts for the deviation from ideal capacitive behavior and is defined by the admittance expression [32-33]:

$$Y(CPE) = Q(j\omega)^n = \quad Q_A\omega^n + jQ_B\omega^n \tag{4.9}$$

$$Q_A = Qcos\left(\pi/2\right) and \quad Q_B = Qsin\left(\pi/2\right) \tag{4.10}$$

where Q is the constant related to the magnitude of dispersion, and n is the phase angle exponent ranges from 0 to 1; with n = 1, the CPE acts as an ideal capacitor, while n = 0 corresponds to ideal resistive behavior. Intermediate values of n represent the degree of

non-ideality, often due to surface roughness, compositional heterogeneity, or a distribution of relaxation times.

The CPE was using EC-Lab software with the fitted parameters as follows same for ACO are: The values of n values associated with grains and grain boundaries remain 0.90 ± 5% and 0.78 ± 5% for ACO samples and 0.86 ± 5% and 0.83 ± 5% for Ni-doped samples. The values of values of Q for the grain and grain boundaries are identified as 21.77 ± 5% pF and 0.20 ± 5% nF for ACO sample and 18.38 ± 5% pF and 13.1 ± 5% nF for the Ni-doped samples within the studied temperature range.

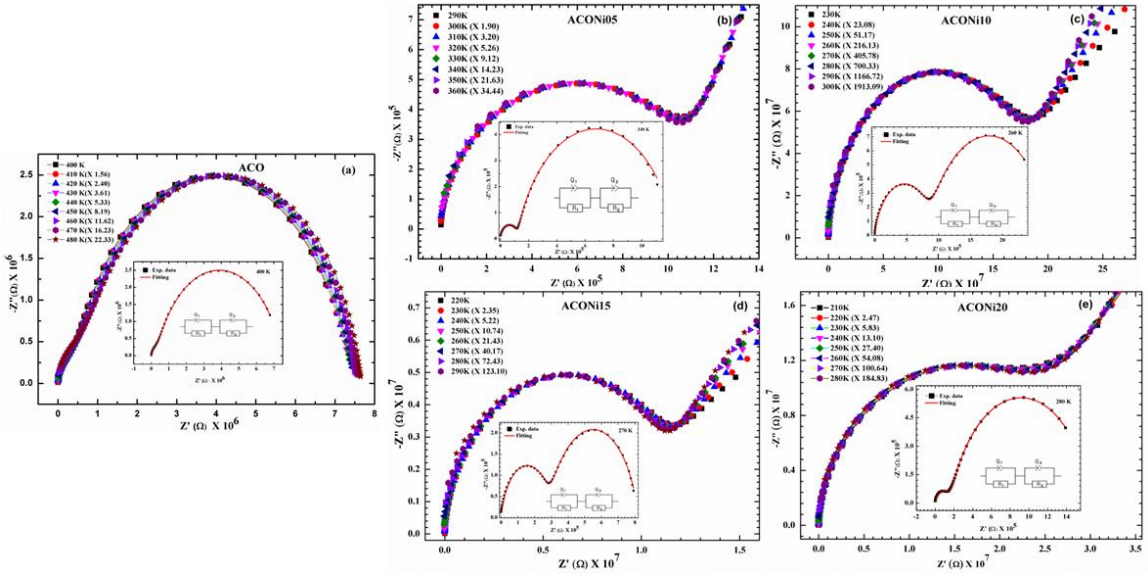

Figure 4.11(a-e): Nyquist plots (Z" versus Z') for ACO and Ni-doped ACO samples at various temperatures, displaying semicircular arcs that correspond to the electrical response of grains and grain boundaries.

For obtaining quantitative data, the resistance values of the grain (R_G) and grain boundary (R_{GB}) were extracted from the fitting of the equivalent circuit to the Nyquist plots at different temperatures.These were further graphically depicted as ln(R) vs. $1/K_BT$, and the respective activation energies (E_a) were calculated by fitting the resulting data to the Arrhenius equation:

$$R_{max} = R_0 e^{(E_a/K_B T)} \qquad 4.11$$

The extracted activation energies for each sample are shown in Figure 4.12(a-e).

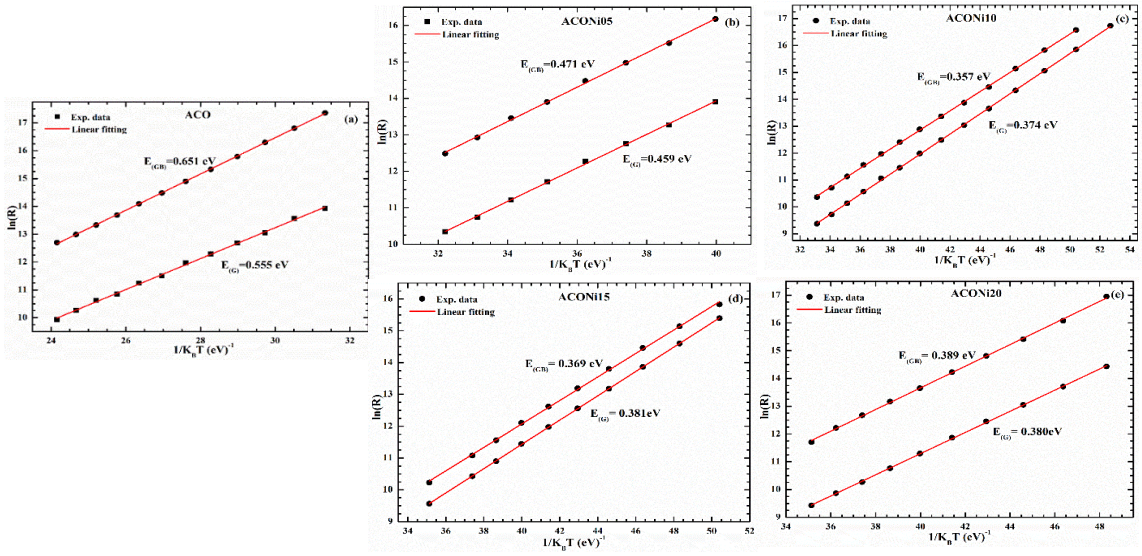

Figure 4.12(a-e): Arrhenius plots of bulk (R_G) and grain boundary (R_{GB}) resistances, showing ln(R) as a function of $1/K_BT$ for all investigated samples.

A notable reduction in activation energy is evident up to x = 0.01 of Ni doping (ACONi10). This reduction trend of E_a reflects a clear enhancement in charge carrier mobility within both grains and grain boundary conduction mechanisms. However, a slight increase in activation energy is observed for ACONi15 and ACONi20, suggesting that beyond optimal doping (x = 0.01), additional Ni doping may lead to defect clustering, phase inhomogeneity, or possible segregation at grain boundaries, which can mildly hinder carrier mobility. Even so, the activation energies at these higher doping levels remain significantly lower than that of the undoped ACO sample.

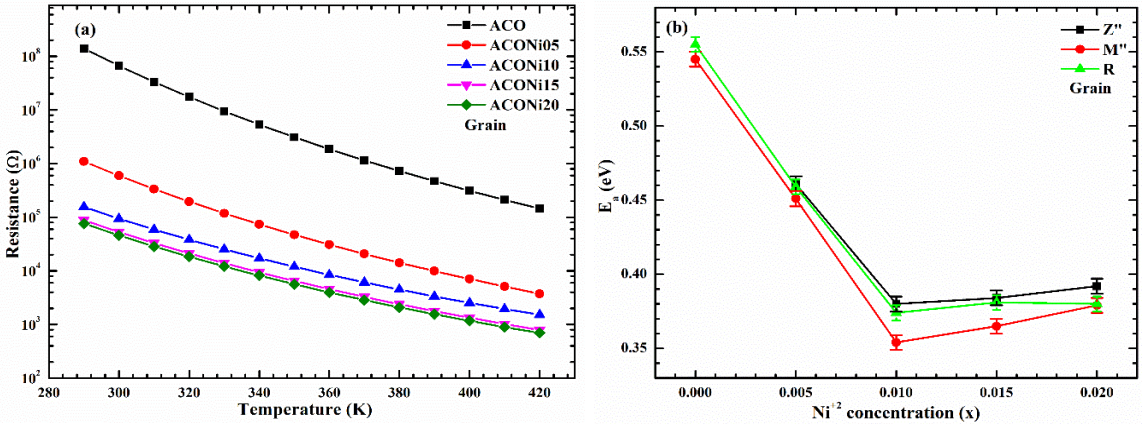

Figure 4.13: (a) Dependence of bulk (grain) resistance on temperature. (b) Change in activation energy for samples with respect to varying Ni^{2+} content (x).

The value of R_0 was determined by extrapolating the fitted linear plots to T = 0 K as depicted in Figure 4.12(a-e). This corresponds to the intercept on the y-axis in the natural

logarithmic form of the Arrhenius relation. Using values in equation 4.8 the resistance of the bulk for a wide range of temperatures was extrapolitted for all the samples as shown in Figure 4.13(a). All samples exhibited a decrease in resistance with increasing temperature, which reveals that negative temperature coefficient of resistance (NTCR) and this behavior strongly confirms the semiconducting nature of the materials [40]. The reduction in activation energy with Ni doping, combined with NTCR behavior, clearly indicates that the introduction of Ni enhances carrier mobility and activates thermally assisted hopping conduction pathways within the material. The activation energy derived from three formalisms such as Z"', M" and Nyquist plot fitting , were plotted as a function of Ni-doping concentration (x = 0, 0.005, 0.01,0.015 and 0.02). The comparative analysis plots were shown in Figure 4.13(b), as activation energy on the y-axis and Ni^{2+} concentration (x) on the x-axis for all three methods. In all the three approaches, it was observed that activation energy was decreased with Ni-doping and reaches minimum at x = 0.01 (ACONi10), which indicates the most efficient charge transport at this doping concentration. At higher concentration x = 0.015 and 0.02, a slight increase in activation energy was observed in all theree formalisms, indicating is likely due to the onset of dopant saturation, defect clustering, or minority impurity phase formations, which may result in introducing scattering centers or trap states.

In conclusion with the combined analysis of activation energy and NTCR behaviour of materials reveals that moderate Ni doping is x = 0.01 (ACONi10), due to enhanced carrier conductions by minimising activation energy, while exhibiting semiconducting characteristics with minimal resistances.

4.5 Photoelectron Spectroscopy (PES)

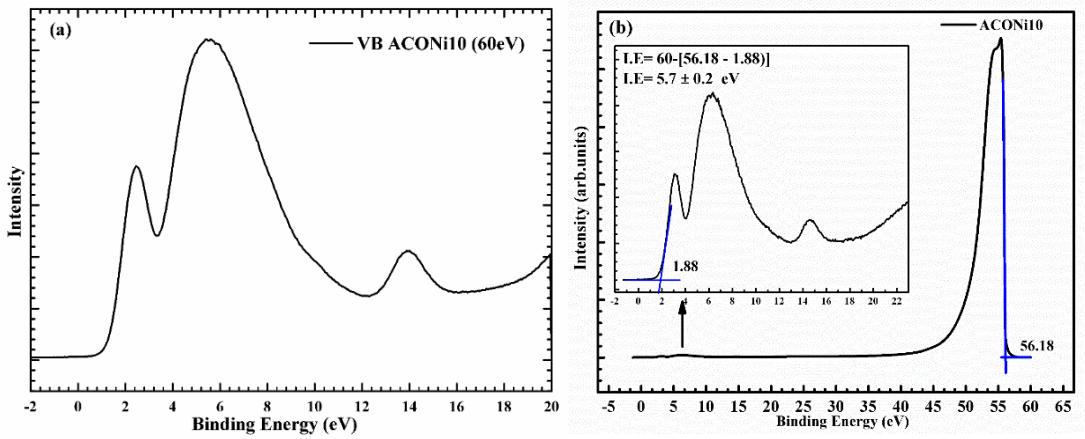

Figure 4.14: (a) Valence Band of ACONi10 sample with synchrotron beam at Indus 1- beamline 3, RRCAT, Indore. (b) The spectrum is referenced with the Fermi level set at 0 eV binding energy, and ionization energies are derived from measurements using synchrotron radiation.

Photoelectron Spectroscopy (PES) measurements were conducted to study the valence band structure and ionization energy (I.E) of $AlCrO_3$ and thereby to investigate the impact of Ni doping. Figure 4.14 (a) presents the valence band spectrum of the ACONi10 sample, acquired using the synchrotron radiation source at Indus-1 (beamline 03, RRCAT, Indore) The spectra were calibrated so that the Fermi level corresponded to 0 eV binding energy. In the valence band spectrum for ACONi10, the first significant feature appears near 1.7 eV binding energy, mainly associated with Cr 3d electronic states, with a smaller contribution from O 2p states in this region. Another prominent band is observed between 5 and 7 eV, which is primarily due to O 2p orbitals, along with some hybridization from Cr 3d states. These features are consistent with the expected electronic structure of chromium-based wide-bandgap semiconductors. The I.E of the ACONi10 sample was determined from the low-energy cutoff in the secondary electron region of the PES spectra, as shown in Figure 4.14 (b). The I.E was calculated to be approximately 5.7 ± 0.2 eV based on measurements using both the synchrotron beam.

4.6 Seebeck Coefficient Measurements

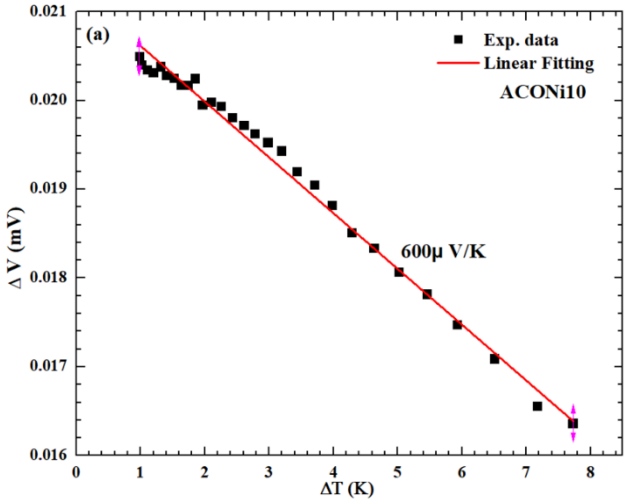

Figure 4.15 (a): Linear fitting of ΔV vs ΔT of ACONi10

Seebeck coefficient measurements were conducted to investigate the nature of charge carriers in the material [43] of Ni-doped α-$AlCrO_3$ of the ACONi10 sample. A controlled heat pulse was used to generate a temperature gradient (ΔT) and the corresponding thermoelectric voltage (ΔV) was recorded. As shown in Figure 4.15, the linear fitting of ΔV versus ΔT yielded a positive Seebeck coefficient of approximately +600 μV/K for ACONi10 and this positive value confirms that holes are the dominant charge carriers which reveals successful *p*-type conduction in the Ni-doped sample [41]. On the other hand, the undoped α-$AlCrO_3$ (ACO) we didn't find negligible Seebeck voltage and consistent with its insulating behavior. These findings affirm that Ni^{2+} substitution at Al^{3+} sites introduces acceptor levels in the valence band, thereby enhancing hole concentration and promoting their delocalization within the Cr-O network.

4.7 Conclusion

In summary, this chapter has explored the structural and electrical characteristics of Ni-doped aluminum chromium oxide samples synthesized by solid state synthesis method with varied concentration (α-$Al_{1-x}Ni_xCrO_3$,$0 \leq x \leq 0.02$) with objective of enhancing its *p*-type semiconducting behavior through doping of aliovalent substitution. The polycrystalline samples were synthesized via solid-state reaction and studied by characterization using SXRD, DRS, CIS, Seebeck coefficient measurements and PES. The XRD analysis confirmed that the synthesized samples exhibited the rhombohedral R-3c

structure was preserved for all doping concentrations, and we observed minor impurity phases beyond $x = 0.01$ which suggests the solubility limit of Ni^{2+} in the $AlCrO_3$ lattice. Optical characterization via DRS reveals that with Ni doping no changes in intrinsic band transitions a thus observed no change in bandgap energy. Electrical impedance analysis showed marked improvements in the dielectric relaxation charge transport phenomenon and reduction of resistance upon Ni doping. Notably, undoped samples displayed a single relaxation process dominated by grain boundary resistance, whereas Ni-doped samples exhibited dual relaxation peaks corresponding to grains and grain boundaries, which reveal an enhanced contribution from short-range conduction to long-range conduction. The corresponding Nyquist plots supported this observation by showing two semicircular arcs, which were successfully modeled using a double CPE equivalent circuit and extracted grain and grain boundary resistance.

Activation energies were extracted from Z″ spectra and M″ spectra and Nyquist plots of resistance. All three formalisms yielded nearly identical values, which strongly indicate that both localized and delocalized conduction mechanisms arise from the same thermally activated charge carriers. The activation energy decreased significantly with Ni doping up to $x = 0.01$ (ACONi10). Furthermore, beyond the doping concentration which leads to increasing in the E_a due to dopant saturation and emerging impurity phases. This trend matched well with the XRD observations that provides a consistent structural-electrical correlation. Additionally, temperature-dependent resistance plots confirm NTCR semiconducting behavior for all samples, which is a characteristic of semiconducting behavior. The resistance dropped drastically by nearly an order of four of magnitude with Ni doping and further affirming the role of Ni in enhancing carrier transport. PES measurements provided further support for these results by the valence band spectra reveal that increased Cr 3d-O 2p hybridization occurs with Ni doping and is accompanied by a I.E of approximately 5.7± 0.2 eV.

In summary, Ni- doping at the Al site in α-$AlCrO_3$ successfully introduces acceptor states and enhances electrical conductivity through a combination of structural distortion and defect engineering, and valence band modulation. Therefore, the optimal performance at $x = 0.01$ of Ni doping (ACONi10) demonstrates the viability of this material for future applications in wide bandgap semiconductors that includes transparent electronics, energy

devices and optoelectronic applications. This chapter lays a strong foundation for extending the same analysis to alternative dopants such as Mg^{2+} as part of objective 2 discussed in the following chapter.

Chapter 5

Mg-Doped α-$AlCrO_3$

5.1 Introduction

Herein, in this chapter we discuss a comprehensive investigation of magnesium-doped aluminum chromium oxide (α-$Al_{1-x}Mg_xCrO_3$) as a potential *p*-type transparent conducting oxide. Building on the investigation of Ni-doping presented in Chapter 4, this chapter examines a series of samples with compositions $Al_{1-x}Ni_xCrO_3$ (x = 0, 0.005, 0.01, 0.015, and 0.02) synthesized under identical conditions to enable direct comparison between the two dopants. The chapter focuses on establishing clear relationships between composition, structure, electrical properties, and optical characteristics, with the goal of evaluating magnesium's potential as a dopant for *p*-type TCO applications.

5.2 Structural Properties

5.2.1 Synchrotron-Based X-ray Diffraction (SXRD)

Synchrotron-based X-ray diffraction patterns for the α-$Al_{1-x}Mg_xCrO_3$ samples are shown in Figure 5.1. As with the undoped sample discussed in Chapter 4, the undoped α-$AlCrO_3$ exhibits a rhombohedral structure with space group R-3c, consistent with earlier reports [19]. For samples with magnesium $x \leq 0.01$ content, XRD diffraction patterns could be indexed to the rhombohedral (R-3c) structure, with no detectable secondary phases. This reveals that successful incorporation of magnesium ions into the host lattice up to this doping concentration. The primary diffraction peaks corresponding to the (012) and (104) planes of the rhombohedral structure show systematic shifts toward lower angles with increasing magnesium content, indicating lattice expansion due to the substitution of Al^{3+} (ionic radius 0.54 Å) with the larger Mg^{2+} ions (ionic radius 0.72 Å). For the sample with magnesium concentration (x = 0.02) possess additional minor diffraction peaks appeared at 2θ values of 5.85°, 13.60°and 19.33°. This indicates that the solubility limit of magnesium in the α-$AlCrO_3$ lattice under the synthesis conditions employed lies between 1.5 and 2.0 atomic percent.

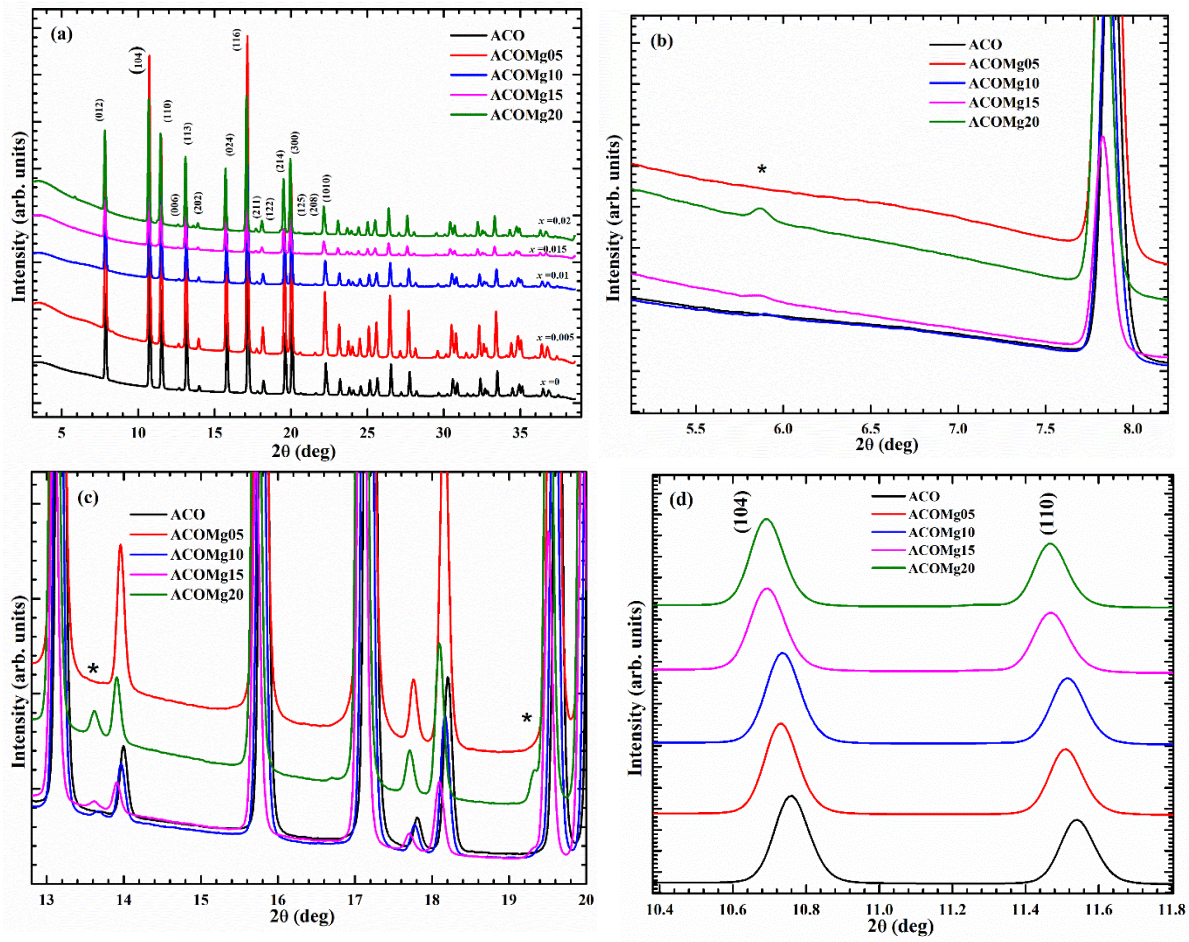

Figure 5.1: X-ray Diffraction (XRD) Analysis of α-$Al_{1-x}Mg_xCrO_3$

5.2.2 Le-Bail Fitting Analysis

Figure 5.2 illustrates the variation of lattice parameters and unit cell volume as a function of magnesium concentration. For samples with $x \leq 0.015$, both the '*a*' and '*c*' lattice parameters increase linearly with magnesium concentration, following Vegard's law. This linear dependence provides strong evidence for the doping incorporation of Mg^{2+} at Al^{3+} sites and allows estimation of the actual dopant concentration in the lattice.

Le-Bail fitting was performed on all diffraction patterns to extract detailed structural information. Figure shows the refinement results, including lattice parameters, unit cell volume, and goodness-of-fit parameters. The refinement confirmed the single-phase nature of samples with the quality of the refinements, as indicated by the low R_{wp} values (< 10%) and goodness-of-fit parameters χ^2~1, confirms the reliability of the structural model.

Comparing the lattice expansion caused by magnesium doping with that observed for nickel doping (Chapter 4), magnesium induces a more pronounced expansion for equivalent doping concentrations. This is consistent with the larger ionic radius difference between Mg^{2+} (0.72 Å) and Al^{3+} (0.54 Å) compared to Ni^{2+} (0.69 Å) and Al^{3+} (0.54 Å).

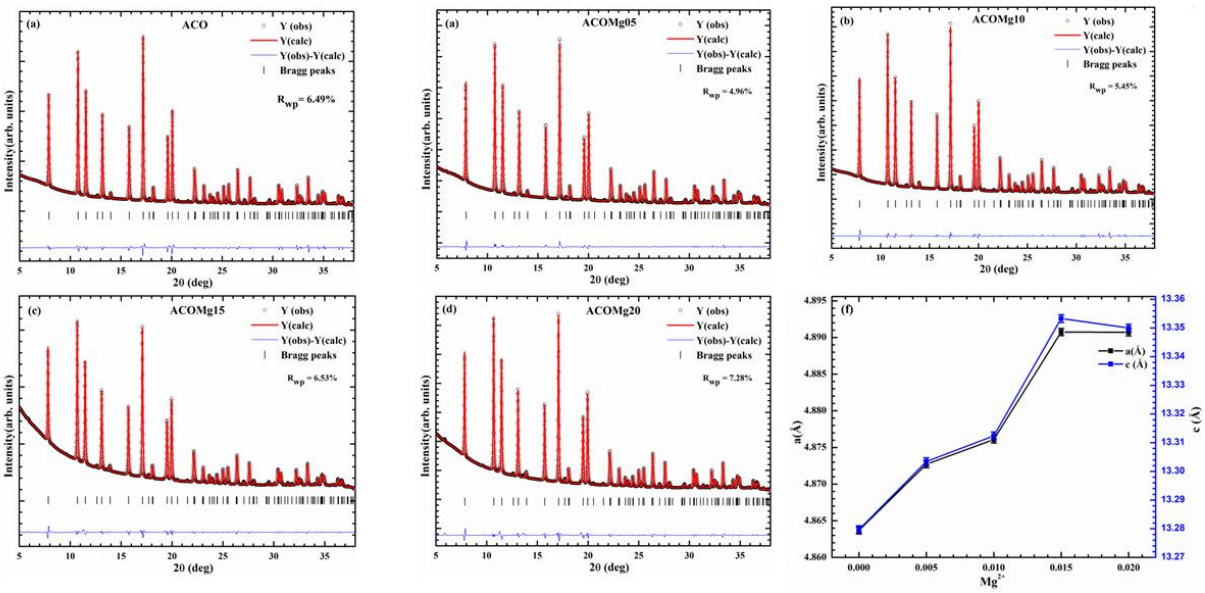

Figure 5.2: Le Bail fitting profile of synchrotron XRD data for α-$Al_{1-x}Mg_xCrO_3$, x = 0.00, 0.005, 0.01, 0.015, and 0.02) samples using FullProf Suite Software. The fitting confirms R-3c phases structure across all compositions. (f) Variation of refined lattice parameter (a, c) as a function concentration in α- $Al_{1-x}Mg_xCrO_3$.

5.3 Diffused Reflectance Spectroscopy

Figure 5.3 displays the F(R) versus Energy (eV) plot for all the samples, showing several distinct transitions in Mg-doped $AlCrO_3$ aligning with those reported by R. Jangir et.al in their study on optical structural properties of $AlCrO_3$ [23]. The absorption features detected at 2.11 eV, 2.86 eV, 4.05 eV, and 5.09 eV are attributed to the electronic transitions $^4A_{2g} \rightarrow {}^4T_{2g}$, $^4A_{2g} \rightarrow {}^4T_{1g}$, Cr $t_{2g} \rightarrow e_g$* and $O_{2p} \rightarrow$Cr d*, and O 2p → Cr d*, respectively. It is widely recognized that the splitting of the d-orbitals in α-Cr_2O_3 leads to an optical band gap of approximately 3.4 eV [44-45]. However, with the substitution of Al, the absorption peak was observed at ~4.05 eV in DRS spectra of α-$AlCrO_3$ (ACO) and Mg-doped α-$AlCrO_3$. Furthermore, no shift in peak positions with increased Mg doping in α-$AlCrO_3$ was observed, indicating that Mg doping does not alter the electronic band structure.

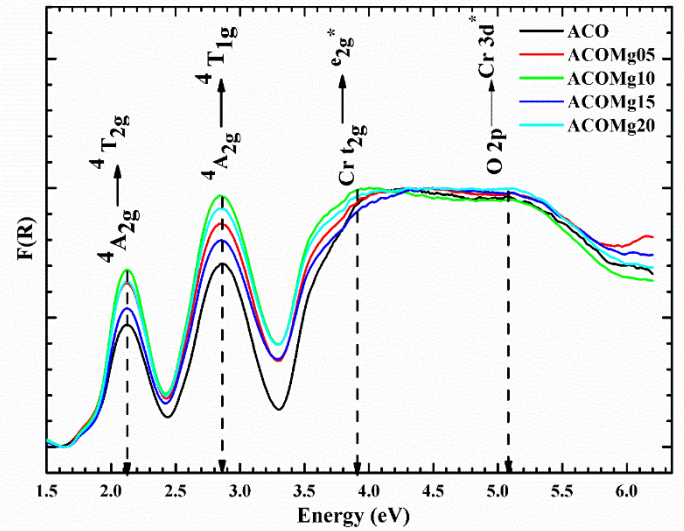

Figure 5.3: DRS of α-$Al_{1-x}Mg_xCrO_3$ plotted as a function of Kubelka-Munk versus Energy (eV) for all samples.

5.4 Electrical Properties by CIS

5.4.1 Complex Impedance Spectroscopy Analysis

To understand the effect of doping on electrical property of the materials, complex impedance spectroscopy was a widely powerful technique [25]. CIS technique is non-destructive and useful to distinguish the contribution from grain and grain boundaries. By doing so, we will get insights into how the small doping has modified the electrical process in the material. Therefore, we have used this technique. In the literature R. Jangir et.al also probed this method to understand the effect of doping [17]. Similarly, we are also utilizing this technique to understand the effects. Therefore, we have performed the CIS measurements in the range of 90K to 480K. CIS Analysis was employed to investigate the frequency and temperature dependent electrical response of Mg-doped $AlCrO_3$. The aim was to understand the effect of Mg^{2+} doping at the Al^{3+} site on charge transport behavior of grain and grain boundaries as well as dielectric mechanisms and activation energy

trends. All measurements were carried out over a frequency of 100 to 1M Hz and over a range of temperature of 90K to 480K.

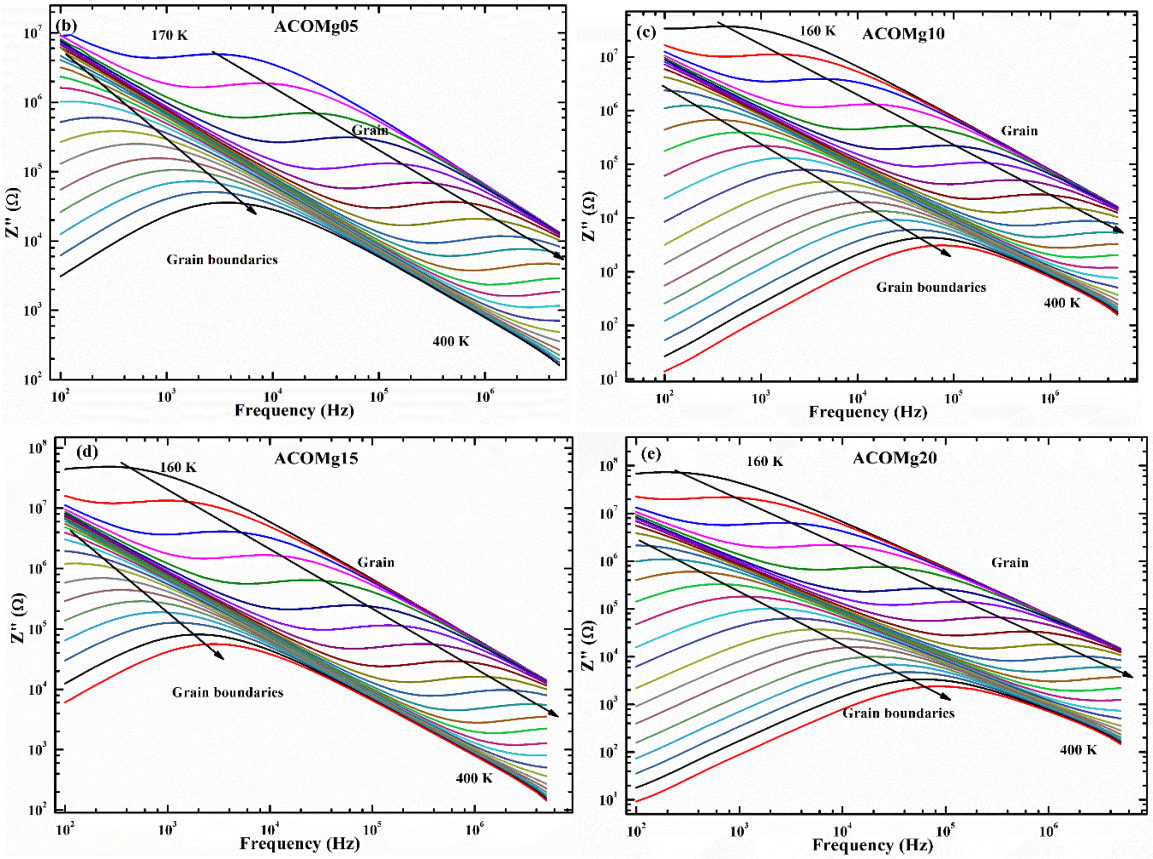

Figure 5.4: Frequency-dependent imaginary(Z") plot for ACO & Mg-doped ACO samples (ACO, ACOMg05, ACOMg10, ACOMg15 and ACOMg20) at various temperature, showing characteristic peaks shifting to higher frequencies with increasing temperature.

Figure 5.4 shows the imaginary part of the impedance (Z'') plotted as a function of frequency (f) for a range of temperature for Mg-doped $AlCrO_3$ samples. It was observed that two relaxation peaks with distinct contributions from grain (high frequency peaks) and grain boundaries (low-frequency peaks). This dual relaxation peaks reveals that heterogeneous polycrystalline materials, where both grain and grain boundaries contribute independently to the overall impedance response. As temperature increases, both peaks shift towards higher frequencies reveals that reduction in relaxation time and thereby confirms that the thermally activated nature of dielectric relaxations. Moreover, the peaks

of the Z” decreases with raise in temperature reflecting reduced resistance and transition towards enhance carrier mobility.

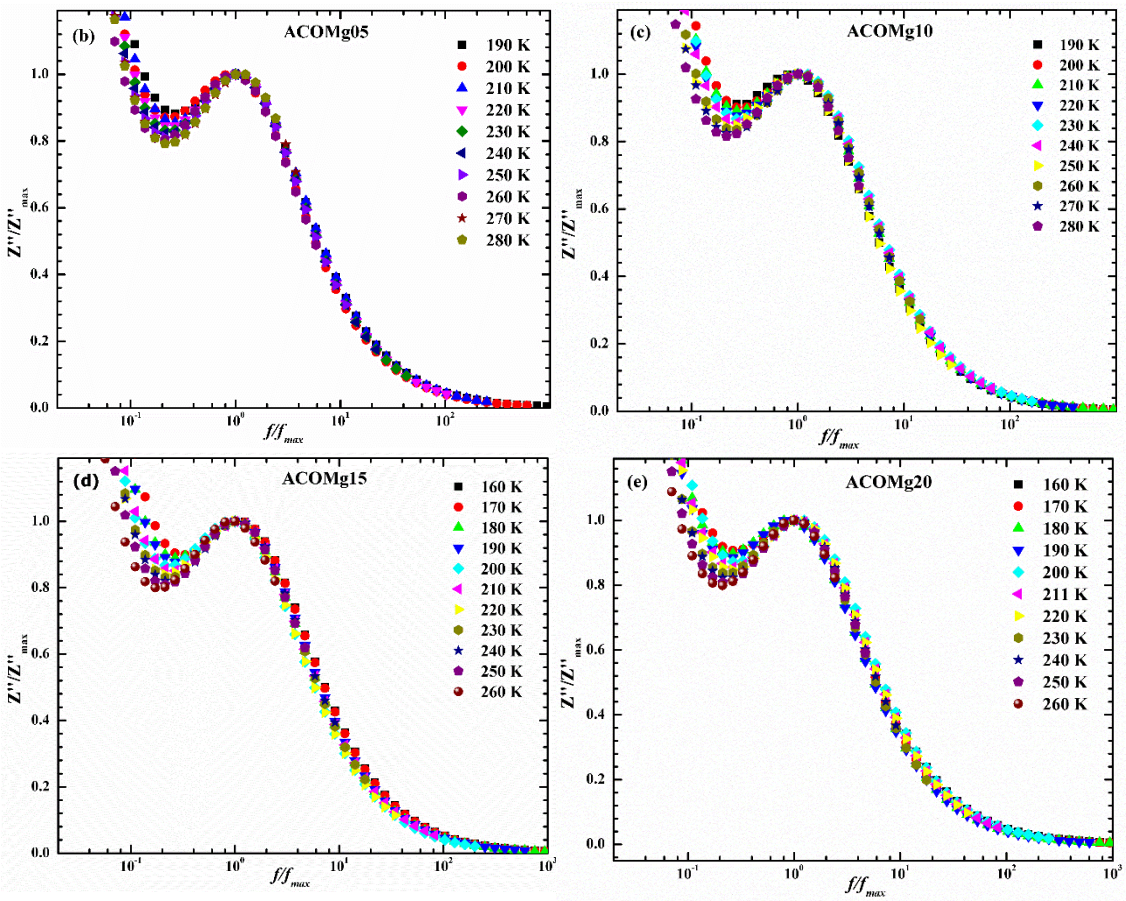

Figure 5.5: Scaled Z”/Z”$_{max}$ versus f/f_{max} plot for the same undoped ACO and ACOMg-doped series, demonstrating temperature- independent relaxation behavior via perfect master curve overlap.

To study the effect of the relaxation mechanism with temperatures, the Z” spectra were normalized by their respective Z” peak maxima (Z”/Z”$_{max}$) and the frequency were scaled by the corresponding peak frequency (f/f_{max}) as shown in the figure 5.5. The resulting master curves reveal that excellent overlap over all measured temperatures indicate that the relaxation behavior is governed by the single relaxation and temperature independent mechanism. This universal scaling behavior confirms that relaxation time constantly shift

with temperature which is fundamental nature of the charge transport mechanism that most likely hopping conduction which had remained unaltered.

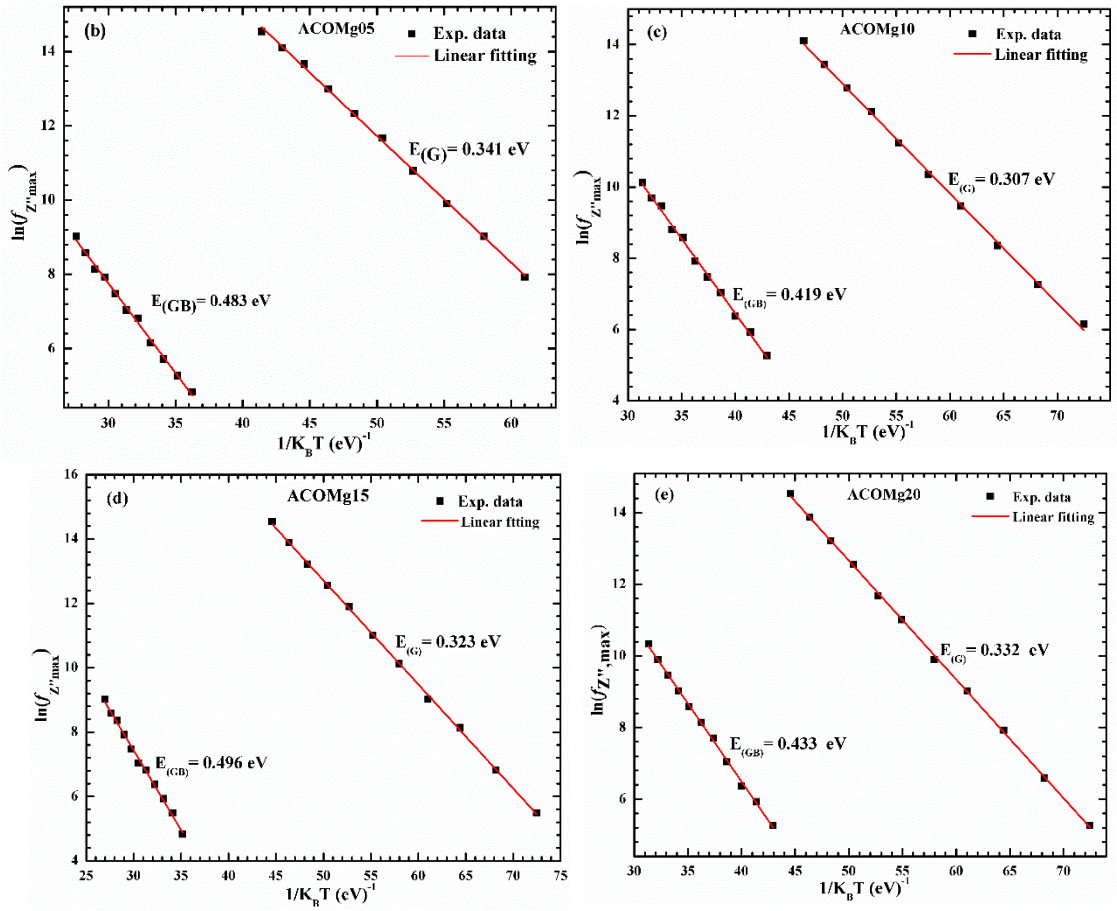

Figure 5.6: Arrhenius plots of ln(f_{max}) versus 1/K_BT derived from Z'' data, used to calculate activation energies for grain & grain boundaries contribution in Mg-doped $AlCrO_3$ samples.

As shown in figure 5.6, the activation energy for grain relaxation of ACOMg05, ACOMg10, ACOMg15 and ACOMg20 obtained as 0.341 eV, 0.307 eV, 0.323 eV and 0.332 eV and for and grain boundary as 0.483 eV, 0.419 eV, 0.496 eV, and 0.433 eV respectively. These results demonstrate a significant decrease in activation energy with Mg doping especially up to x = 0.01. The decrease in activation energy reveals that enhanced carrier mobility and hopping conduction. The slight increase of E_a at higher doping x=0.015 and 0.02 may be attributed to defect interactions or limited solubility of Ni in the lattice.

5.4.2 Modulus Impedance Spectroscopy

In order to complement the impedance analysis and supress grain boundary contributions, electric modulus formalisms were used for Mg-doped $AlCrO_3$. The modulus

formalism provides the insight into grain (bulk) relaxation phenomenon contribution which may otherwise be masked in the impedance spectra due to highly resistive grain boundaries.

The imaginary part of modulus spectra M" plotted as a function of frequency for all Mg-doped $AlCrO_3$. In contrast to the Z'' vs *f* plots, the M'' vs *f* plots revealed single well defined relaxation peaks at each temperature for all samples. This observation indicates that conduction that contributed by grain (bulk) dominates in the modulus spectra, while grain boundary contribution is effectively suppressed due to their comparative larger capacitance values. To further analyze these characteristics, temperature-dependent M" vs *f* plotted as shown in the Figure 5.7 for α-$Al_{1-x}Mg_xCrO_3$ samples ACOMg05, ACOMg10, ACOMg15, and ACOMg20).

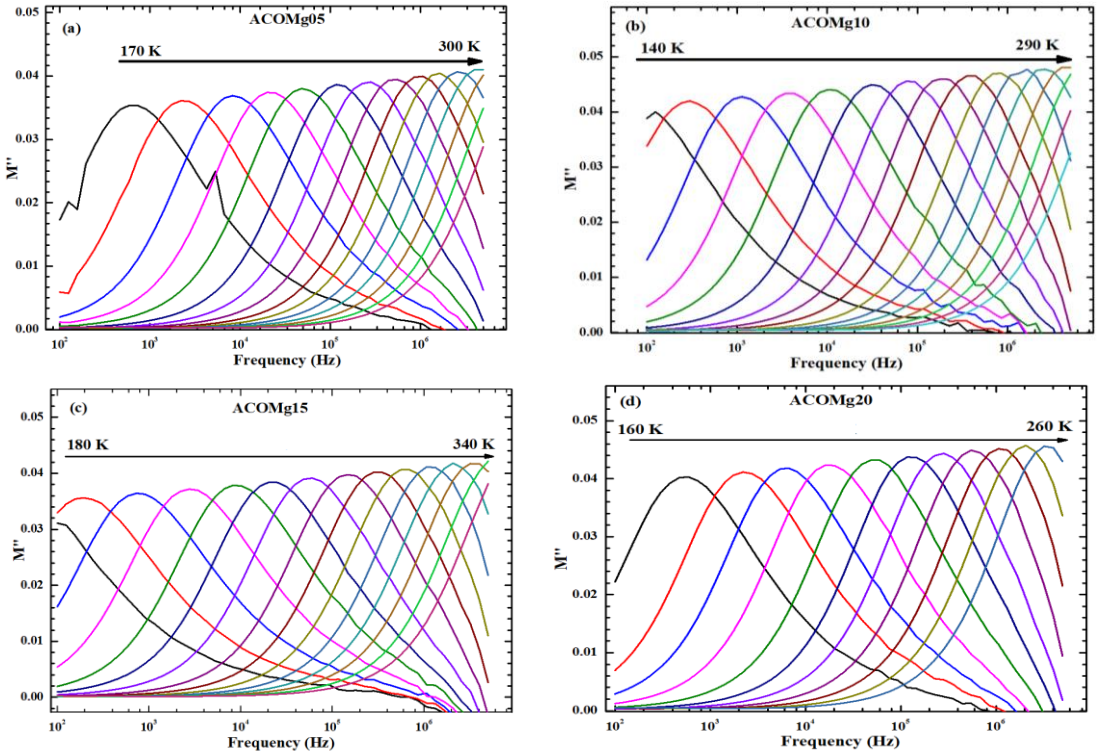

Figure 5.7: M" plotted Frequency-dependent plots of M" at various temperatures for α-$Al_{1-x}Mg_xCrO_3$ samples (ACOMg05, ACOMg10, ACOMg15, and ACOMg20).

The prominent relaxation peak confirms the presence of conductivity relaxation process is thermally activated. The peak frequency position shift to higher frequency with rise of temperature provides insights into the transitions from the short-range localized

motion to long-range conduction of charge carriers. In the low frequency range, charge carriers possess sufficient energy to hop between adjacent lattice sites thereby providing the long-range conduction across the grains(bulk). In contrast, in the high-frequency range, the conductions of charge carriers are spatially confined to their potential wells and can perform only localized conductions [46].

5.4.3 M″ Scaling Behaviors Spectra: M″/M″$_{max}$ vs f/f_{max} Master Curve

he imaginary part of the electric modulus, M’’, was divided by its peak value, M″max, and the frequency was scaled relative to the peak frequency, f_{max}, for each temperature. The resulting master curves, shown in Figure 5.8, display M’’/M’’$_{max}$ plotted against f/f_{max} for all samples over the full temperature range studied. The complete overlapping of curves at different temperatures for each composition depicts a temperature-independent relaxation mechanism. This overlap confirms that the distribution of relaxation times and the shape of the relaxation function remain unchanged although the absolute values of relaxation time and peak frequency shift with temperature as expected for thermally activated processes.

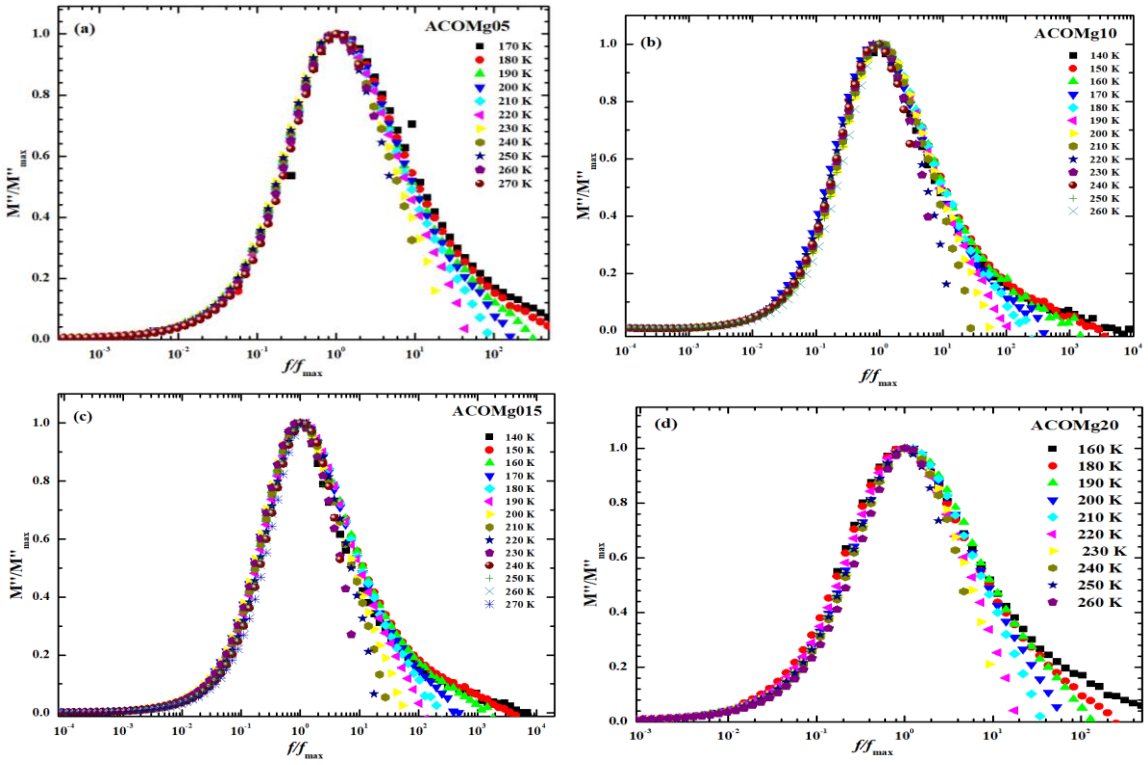

Figure 5.8: Scaled plots of the imaginary part of the modulus spectra, highlighting the consistent behavior across different temperatures, i.e., M”/M”$_{max}$ vs f/f_{max} for all samples ACO, ACOMg05, ACOMg10, ACOMg15, and ACOMg20.

In other words, the microscopic mechanism responsible for dielectric relaxation is likely due to thermally activated hopping of localized charge carriers remaining the same throughout the studied temperature range. Moreover, the shape of the normalized M'' spectra appears symmetric and relatively narrow, revealing that a quasi-Debye type relaxation mechanism, typically indicative of a well-defined potential landscape for charge carriers within the grains, is dominant. This observation is consistent with the earlier impedance analysis that revealed well-separated grain and grain boundary responses and supports the idea that modulus formalism effectively extracts the bulk (grain) contribution. In summary, the modulus scaling behavior provides compelling evidence that the dielectric relaxation in Mg-doped $AlCrO_3$ is governed by a single, thermally activated mechanism, consistent with hopping conduction in the bulk phase. The activation energies related to the conduction mechanism in the material were obtained from the analysis of the modulus (M'') spectra. Figures 5.9 (a-d) shows Arrhenius fit of $\ln(f_{M'',max})$ versus $1/K_BT$ data, which was used to estimate the activation energy associated with the relaxation process. The sample ACO exhibited activation energy as 0.545 eV as shown in the last chapter and similarly here the ACOMg05, ACOMg10, ACOMg15, and ACOMg20 activation energy derived from the plots for grain contribution as 0.367 eV, 0.285 eV, 0.288 eV and 0.313 eV and for grain boundaries contribution as 0.450 eV ,0.448 eV, 0.500 eV and 0.473 eV respectively. Activation energy drastically decreased upon doping up to $x = 0.01$ and slight

increase in E_a observed with higher doping same results consistent in the Z" spectra analysis.

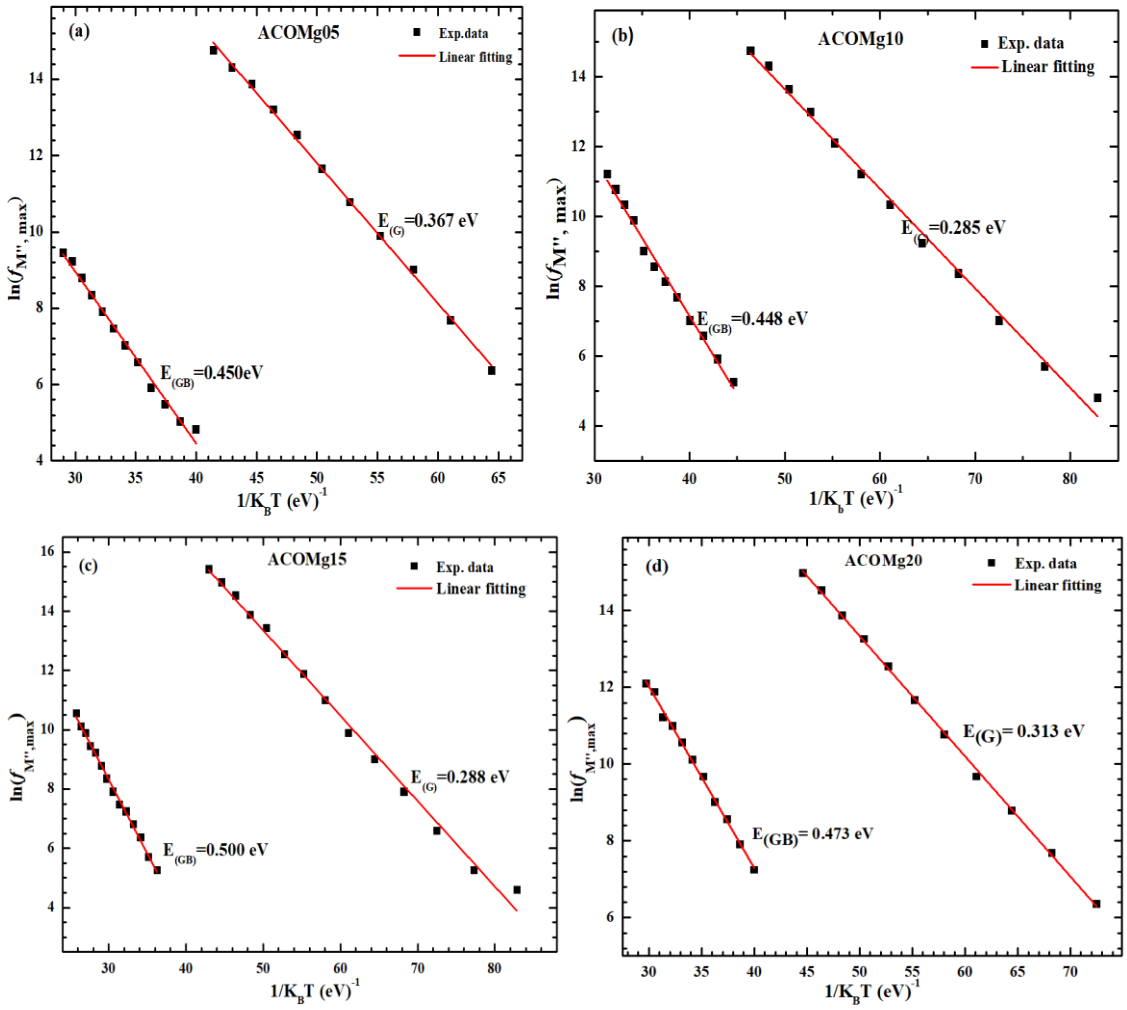

Figure 5.9: Arrhenius plots of ln(f_{max}) versus 1/K_BT derived from M'' spectra for all α-$Al_{1-x}Mg_xCrO_3$ samples (ACOMg05, ACOMg10, ACOMg15, and ACOMg20).

5.4.4 Nyquist Plot Analysis

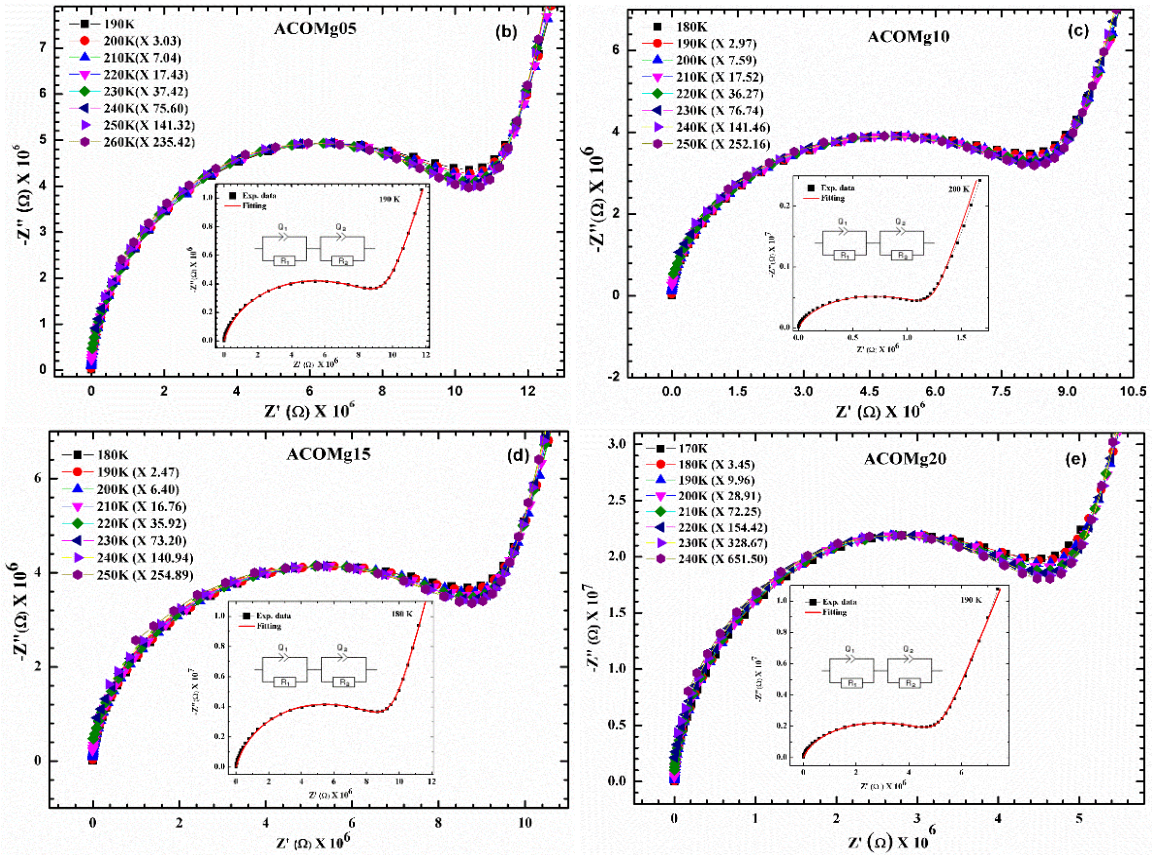

Figure 5.10: Nyquist (Z" vs Z') for ACO and Mg-doped ACO samples at different temperatures indicating semicircular arc are attributed to grain and grain boundaries response.

The Nyquist plots (Z″ vs Z′) of α-$Al_{1-x}Mg_xCrO_3$ were analyzed to understand the roles of grains and grain boundaries in influencing the total conduction behavior. The Nyquist plots for ACOMg05, ACOMg10, ACOMg15, and ACOMg20 exhibited two distinct semicircular arcs as shown in the Figure 5.10. The high-frequency arc corresponds to the grain (bulk) conduction process while the lower frequency arc is associated with the grain boundaries conduction. To extract resistance and capacitance values, the impedance spectra was fitted using an equivalent circuit model of CPE as discussed in the last chapter. The equivalent circuit used in shown in the inset of the Figure 5.10. The CPE fitting was carried using EC-Lab software with the fitted parameters as follows same for the Mg-doped $AlCrO_3$ sample values of n for grain and grain boundaries remains as 90 ± 5% and 0.88 ± 5% respectively. The values of values of Q for the grain and grain boundaries are identified

as 14.38 ± 5% pF and 0.41 ± 5% *n*F for Mg-doped samples within the studied temperature range.

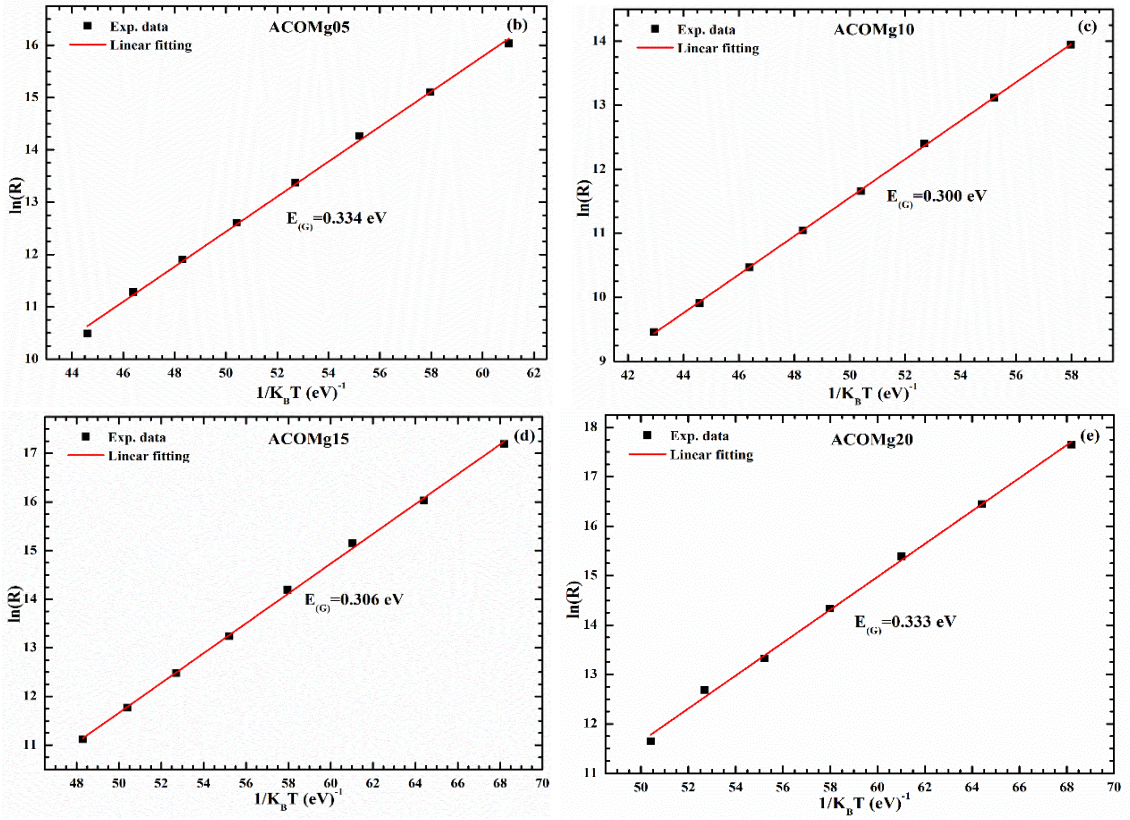

Figure 5.11: Arrhenius plots of bulk (R_G) and grain boundary (R_{GB}) resistances, showing ln(R) as a function of $1/K_BT$ for all investigated samples.

The temperature dependence of the bulk resistance (R_G) for the Mg doped $AlCrO_3$ samples was analysed to further investigate the conduction mechanism. The extracted R_G values were plotted as ln(R) versus $1/K_BT$ as shown in Figure 5.11 and fitted using the Arrhenius equation 4.8. The ln(R) versus $1/K_BT$ plots for each sample exhibited good linearity over the studied temperature range, confirming that thermally activated hopping conduction governs the bulk transport mechanisms. The activation energy values corresponding to the grain (bulk) conduction were extracted as follows 0.334 eV, 0.300 eV, 0.306 eV and 0.333 eV respectively. The data show a significant reduction in activation energy with Mg doping, reaching a minimum at ACOMg10. This trend reflects the enhanced carrier mobility due to Mg incorporation, which likely introduces oxygen vacancies and modulates the local bonding environment, facilitating easier hopping of

charge carriers. The slight increase in activation energy observed for ACOMg10 and ACOMg20 may be attributed to dopant saturation effects or defect clustering.

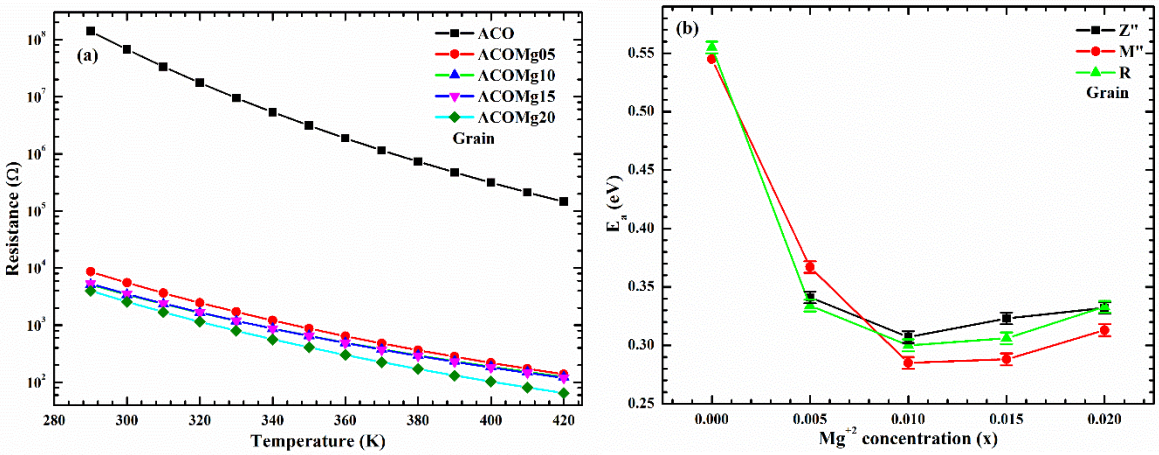

Figure 5.12: (a) Dependence of bulk (grain) resistance on temperature. (b) Change in activation energy for α-$Al_{1-x}Mg_xCrO_3$ samples (x = 0.0 to 0.02), as determined from the imaginary component of impedance (Z"), electric modulus (M"), and resistance values from Nyquist plots, with respect to varying Mg^{2+} content (*x*).

From the Arrhenius fitting of the ln(R) versus $1/K_BT$ plots shown in Figure 5.11, the values of the pre-exponential factor (R_o) and activation energy (E_a) were extracted for all Mg-doped $AlCrO_3$ samples. Using these extracted parameters, the bulk grain resistance (R_G) was extrapolated and plotted over an extended temperature range, as illustrated in Figure 5.12. The plotted resistance curves confirm a systematic decrease in R with increasing temperature across all compositions, demonstrating a clear NTCR behaviour [33]. Such NTCR characteristics are typical of semiconducting materials, where thermally activated charge carriers enable enhanced conductivity at elevated temperatures. The activation energy derived from three formalisms such as Z"', M" and Nyquist plot fitting , were plotted as a function of Mg-doping concentration (*x* = 0, 0.005, 0.01,0.015 and 0.02). The comparative analysis plots were shown in Figure 5.12(b), as activation energy on the y-axis and Mg^{2+} concentration (*x*) on the *x*-axis for all three methods. In all the three approaches, it was observed that activation energy was decreased with Mg-doping and reaches minimum at *x* = 0.01 (ACOMg10), which indicates the most efficient charge transport at this doping concentration. At higher concentration *x* = 0.015 and 0.02, a slight increase in activation energy was observed in all theree formalisms, indicating is likely due

to the onset of dopant saturation, defect clustering, or minority impurity phase formations, which may result in introducing scattering centers or trap states.

In particular, the resistance of $AlCrO_3$ materials was found to decrease drastically with Mg doping, consistent with the enhanced charge carrier mobility due to defect-induced conduction mechanisms. The overall decrease in resistance upon Mg doping is nearly four orders of magnitude ($\sim 10^4$ times) compared to the undoped $AlCrO_3$ material, confirming the effectiveness of Mg doping in significantly improving the *p*-type conductivity. This remarkable reduction in resistance and activation energy upon Mg incorporation aligns well with the trends observed from the impedance and modulus analyses.

Together, these findings strongly reinforce that Mg-doped $AlCrO_3$ is a promising wide bandgap semiconductor material suitable for future transparent electronics and optoelectronic device applications.

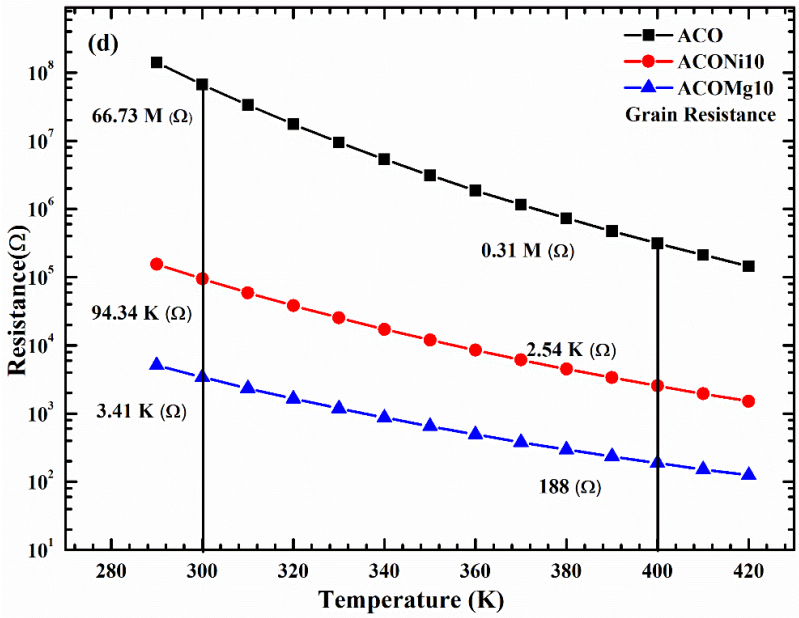

Figure 5.13: Comparative analysis of Resistance vs Temperature ACO, ACONi10 and ACOMg10.

Comparative analysis of ACO, ACONi10 and ACOMg10 were analysed as shown in the Figure 5.13. It was observed that the ACOMg10 sample exhibited lower resistance than the ACONi10 samples which reveals that the delocalization with Mg doping is more comparative to that of Ni doping samples. This may be due to the Mg 2s spatially spherical

orbitals that significantly enhancing the delocalization thus resulted in the better preformation.

5.5 Seebeck Coefficient Measurements

Seebeck coefficient measurements were performed to further confirm the nature of charge carriers in Mg-doped α-$AlCrO_3$ on the ACOMg10 sample [26]. The thermoelectric voltage (ΔV) was recorded as a function of temperature difference (ΔT) generated through a controlled thermal gradient. The ΔV versus ΔT plot as shown in Figure 5.14 exhibited a clear linear trend, and the extracted Seebeck coefficient was positive, with a magnitude of approximately +566 μV/K. This result confirms the *p*-type conduction in Mg-doped $AlCrO_3$, with holes being the majority charge carriers [41].

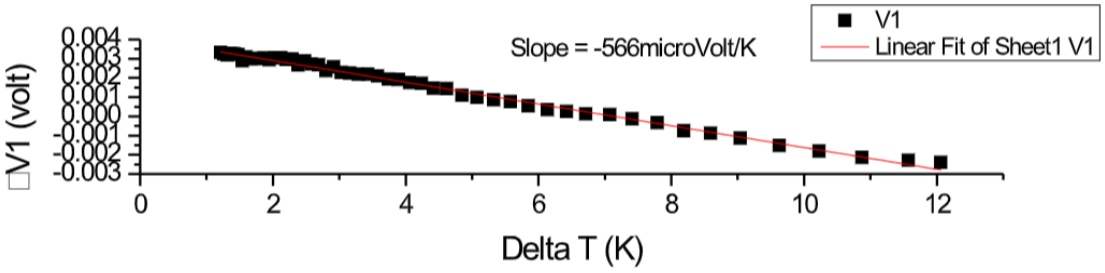

Figure 5.14: Linear fitting of ΔV vs ΔT to for ACOMg10 to extract the Seebeck coefficient.

The absence of any measurable Seebeck voltage in the undoped α-$AlCrO_3$ sample is consistent with its insulating character. The positive Seebeck response observed in ACOMg10 reflects the creation of acceptor states due to Mg^{2+} substituting for Al^{3+}, leading to the generation and delocalization of hole carriers within the Cr-O framework.

5.6 Photoelectron Spectroscopy

The valence band spectra and I.E for the sample ACOMg10 was obtained using PES measurements at BL-03 of the Indus-I synchrotron radiation source. Figure 5.15 (a-b) displays the PES spectra for the sample ACOMg01.The spectrum is calibrated such that the valence band edge falls at 0 eV binding energy, representing electrons with the maximum kinetic energy emitted from the sample. The difference between the maximum kinetic energy (KE_{max}) and minimum kinetic energy (KE_{min}) from the secondary edge helps in determining the ionization energy of the sample. The ionization energy is calculated using the following equation:

$$IE = \hbar\omega - |KE_{max} - KE_{min}| \quad 5.1$$

where $\hbar\omega$ represents the energy of the photons.

PES measurements were conducted to study the electronic structure and valence band and work function of $AlCrO_3$ and thereby investigate the impact of Mg doping. Figure 5.15 (a-b) presents the valence band spectrum of the ACOMg10 sample, acquired using the synchrotron radiation source at Indus-1 (Beamline 03, RRCAT, Indore) and I.E evaluation. The ionisation energy (I.E) of the ACOMg10 sample was calculated to be 5.1 ± 0.2 eV. The ± 0.2 eV was considered as an error margin for experimental and fitting error. The spectra were calibrated such that the Fermi level was set at 0 eV binding energy. In the valence band spectrum of ACOMg10, the first major feature appears around 1.7 eV binding energy, which is primarily attributed to the Cr 3d states. A smaller contribution from the O 2p states is also present in this region. A second prominent band is observed in the range of 5-7 eV, which mainly arises from O 2p orbitals, with some hybridization contribution from Cr 3d states. These features are consistent with the expected electronic structure of chromium-based wide-bandgap semiconductors. The I.E. of the ACOMg10 sample was determined from the low-energy cutoff in the secondary electron region of the PES spectra, as shown in Figure 5.15(b). The ionization energy was calculated to be approximately 5.1 ± 0.2 eV based on measurements using both the synchrotron beam. This is suitable for many applications in optoelectronics such as solar cells and LEDS as hole blocking layer.

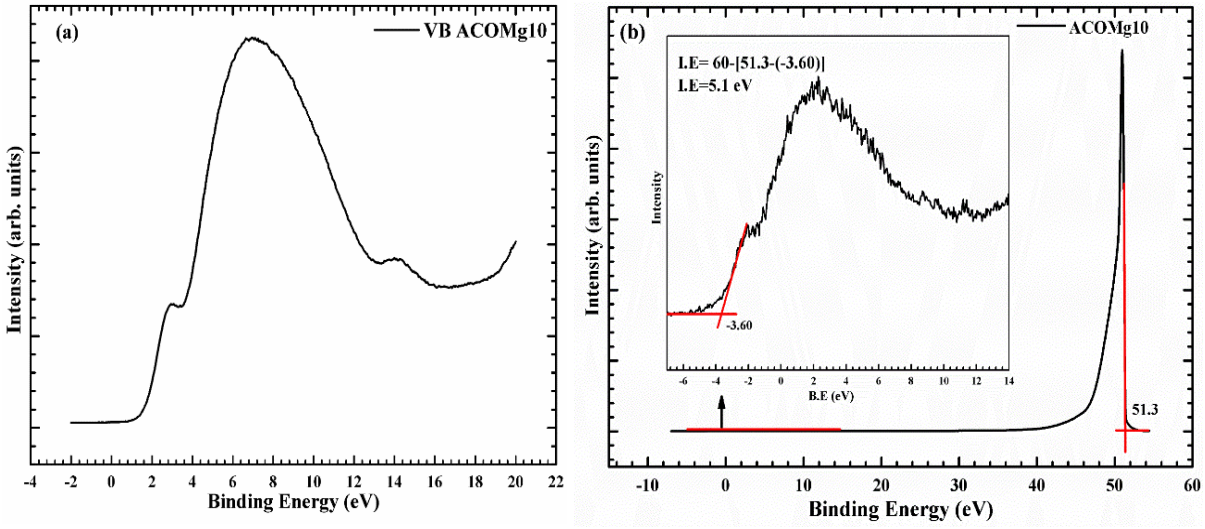

Figure 5.15: (a) Valence Band of ACOMg10 sample and I.E calculated from the data obtained from synchrotron radiation of 60 eV of beamline-3, of Indus 1, RRCAT, Indore.

5.7 Conclusion

In this chapter, we have investigated the effect of magnesium-doped in α-$AlCrO_3$ (α-$Al_{1-x}Mg_xCrO_3$,$0 \leq x \leq 1$) was undertaken to evaluate its potential as a wide bandgap *p*-type transparent conducting oxide. Structural analysis using SXRD confirmed polycrystalline single phase rhombohedral R-3c structure up to $x = 0.01$ and observed that beyond doping which leads to minor secondary phases emerging that indicating the solubility limit of Mg^{2+} in the lattice. Le-Bail fitting revealed a linear expansion of lattice parameters with doping consistent with Vegard's law up to $x = 0.01$ of Mg doping of Mg^{2+} at Al^{3+} site.

Optical studies using DRS showed characteristic Cr-centered d-d transitions with the band edge transition remaining nearly unchanged for all samples suggesting that Mg doping does not significantly alter the fundamental band structure indicating no change in bandgap energy. Complex impedance and electric modulus spectra analyses revealed dual relaxation processes of grain and grain boundary with a clear transition from localized short-range to long-range conduction upon Mg doping. Temperature scaling of Z''/Z''_{max} and M''/M''_{max} master curves confirms temperature-independent relaxation dynamics governed by a single thermally activated mechanism.

Moreover, activation energies extracted from Z'' formalism and M'' formalism and Nyquist plot analyses consistently demonstrated a sharp decrease with Mg doping up to $x = 0.01$ (ACOMg10) which indicates enhanced carrier mobility through polaron hopping. Further doping ($x \geq 0.015$) led to a slight increase in activation energies which is likely due to defect induced effects of scattering. The NTCR behavior observed for all compositions samples which affirms the semiconducting nature of the material while bulk resistance decreased by nearly four orders of magnitude upon Mg doping.

Chapter 6
Conclusion and Future Scope

Chapter 6: Conclusion and Future Scope

6.1 Conclusion

In our work, we have explored *p*-type doping in aluminum chromium oxide α-$AlCrO_3$, focusing on aliovalent doping strategies involving nickel (Ni^{2+}) and magnesium (Mg^{2+}) at the aluminum (Al^{3+}) site. The main aim was to enhance the *p*-type conductivity of α-$AlCrO_3$ while preserving its wide bandgap and structural stability, thereby advancing its suitability for optoelectronic and transparent device applications.

The results from Ni- and Mg-doping investigations reveal that α-$AlCrO_3$ is an selectronically tunable host lattice capable of incorporating divalent dopants without significant disruption to the corundum structure (R-3c) up to their respective solubility limits. Comprehensive characterizations such as SXRD, Le-Bail fitting, DRS, CIS, Seebeck coefficient measurement confirmed that both dopants introduced defect-mediated pathways for hole conduction and more significantly reduced the activation energies associated with carrier transport.

Firstly, from the comparative analysis of Ni-doped synthesized samples, it was found that Ni-doping induced noticeable improvements in both bulk and grain boundary conduction by lowering the activation energy for conduction. Furthermore, we observed that the doping concentration at x = 0.01 (ACONi10), where the activation energy was reached. Hereby, Ni^{2+} doping led to generation of $Cr^{3+/}$ Cr^{4+} oxidation thereby hole generated that enhanced charge transport. However, beyond optimal doping level, a slight increase in activation energy and the emergence of secondary phases suggested dopant oversaturation and localized defect scattering.

In contrast, Mg^{2+} doping also proved highly effective in reducing the resistance of α-$AlCrO_3$, with the best performance observed at x = 0.01 (ACOMg10). The larger ionic radius of Mg^{2+} caused a more pronounced lattice expansion than $Ni^{2+,}$ and while it lacked d-orbital contribution, its role in promoting oxygen vacancy formation and modulating the local defect landscape enabled enhanced grain conductivity. Importantly, Mg-doped samples retained their structural integrity with minimal phase separation, and activation energies derived from Z'', M'', and Nyquist analysis collectively confirmed the dominance of thermally activated hopping transport in the grain region.

The resistance versus temperature (R-T) plots of ACO, ACOMg10 and ACONi10 reveal all samples indicating NTCR behavior whereas that minimum resistance offered by ACOMg10 samples. The resistance drops of ACO sample from the order of Mega (Ω) to Kilo (Ω), reveals that significant effect of dopant that induced conductivity in the samples. Moreover, all samples exhibited a steep NTCR trend that dropping and when compared to the ACO, ACONi10 and ACOMg10 sample, the resistance dropped significantly. For ACONi10 sample resistance drops of the order of three and ACOMg10 sample by four compared the undoped ACO samples. This reveals that enhanced conductivity would be possible for the sample of Mg doped $AlCrO_3$.

Positive Seebeck coefficients of +566 μV/K for ACOMg10, +600 μV/K for ACONi10 unambiguously confirmed *p*-type behavior, which reveals that the majority charge carriers that are responsible for conductions are holes. Therefore, we can conclude that the *p*-type semiconductor nature for both Ni- and Mg- doped $AlCrO_3$ samples. PES measurement revealed that ionization energy of 5.1 eV and 5.7 eV ± 0.2 eV for ACOMg10 and ACONi respectively, that demonstrated excellent alignment with hole transport layer requirements in perovskite solar cells and organic photovoltaic devices applications.

These findings establish Mg- doped α-$AlCrO_3$ as a breakthrough *p*-type transparent semiconductor that successfully bridges the critical performance gap between existing materials and the demanding requirements of emerging transparent electronics that include UV optoelectronics, and high-efficiency energy conversion technologies. The demonstrated combination of wide bandgap energy which promises excellent optical transparency with enhanced *p*-type conductivity and device-compatible work functions positions this material system as a transformative platform for advancing the frontiers of transparent conducting oxide research and enabling the next generation of efficient, versatile optoelectronic devices operating across extended spectral ranges. Therefore, this material can be potential candidates any many applications such as UV detectors, hole transport material (HTL) in perovskite solar cells applications, p-n junction solar cells, and many more.

6.2 Future Scope

Herein, in our work the successful synthesis and characterization of Ni- and Mg-doped p-type aluminum chromium oxide (α-$AlCrO_3$) research has laid the work for further exploration into these materials as a potential candidate for next-generation optoelectronic devices. However, several opportunities remain open for extending and deepening the investigation into these materials. The following directions are proposed for future research:

Even though this study focused on bulk polycrystalline samples synthesized via solid-state reactions, the future work should aim at fabricating thin films of α-$Al_{1-x}B_xCrO_3$ (B = Ni, Mg) using advanced deposition techniques such as pulsed laser deposition (PLD), RF magnetron sputtering (RFMS), and atomic layer deposition (ALD). Thin-film growth techniques would allow integration of these materials into real optoelectronic applications and facilitate the way for future device integration.

Given the high work function (~5.1 eV for ACOMg10 and ~5.7 eV for ACONi10) with the wide band gap energy and demonstrated *p*-type semiconducting behavior, these materials are well-suited for use as hole transport layers (HTLs) in perovskite solar cells, dye-sensitized solar cells, and organic light-emitting diodes (OLEDs). Therefore, future studies should focus on:

- Fabrication of complete heterojunction devices ACONi10 and ACOMg10 as HTLs.
- Investigating energy level alignment with adjacent layers (e.g., perovskites or organic semiconductors).
- Device performance synthesized by these samples such as open-circuit voltage (V_{oc}) and power conversion efficiency (PCE).
- Fabrication of UV detectors.

Based on the valence band position and work function data, future work could explore the formation of *p*-*n* junctions or heterojunctions with widely used *n*-type TCOs (e.g., ZnO, SnO_2, In_2O_3). These would enable transparent diodes, photodetectors, and transistor devices.

References

1. D. Ginley, *Handbook of Transparent Conductors*, 2011.
2. G. Hautier, A. Miglio, G. Ceder, G.-M. Rignanese, and X. Gonze, "Identification and design principles of low hole effective mass *p*-type transparent conducting oxides," Nature Communications, vol. 4, p. 2292, 2013/08/13 2013.
3. D. Ginley, T. Coutts, J. Perkins, D. Young, X. Li, and P. Parilla, "Next-Generation Transparent Conducting Oxides for Photovoltaic Cells: an Overview," MRS Proceedings, vol. 668, 01/01 2001.
4. T. Wang, K. Lu, Z. Xu, Z. Lin, H. Ning, T. Qiu, et al. (2021, Recent Developments in Flexible Transparent Electrode. Crystals 11(5).
5. H. Wen, B. Weng, B. Wang, W. Xiao, X. Liu, Y. Wang, et al. (2024, Advancements in Transparent Conductive Oxides for Photoelectrochemical Applications. Nanomaterials 14(7).
6. J.-K. Lee and M. Yang, "Progress in light harvesting and charge injection of dye-sensitized solar cells," Materials Science and Engineering: B, vol. 176, pp. 1142-1160, 2011/09/15/ 2011.
7. C.-J. Chang, C.-W. Lai, W.-C. Jiang, Y.-S. Li, C. Choi, H.-C. Yu, *et al.*, "Fabrication and Characterization of P-Type Semiconducting Copper Oxide-Based Thin-Film Photoelectrodes for Solar Water Splitting," *Coatings*, vol. 12, p. 1206, 08/17 2022.
8. K. Ellmer, "Past Achievements and Future Challenges in the Development of Optically Transparent Electrodes," Nature Photonics, vol. 6, pp. 809-817, 12/01 2012.
9. L. Hu, R. H. Wei, X. W. Tang, W. J. Lu, X. B. Zhu, and Y. P. Sun, "Design strategy for p-type transparent conducting oxides," Journal of Applied Physics, vol. 128, p. 140902, 2020.
10. K. H. L. Zhang, K. Xi, M. G. Blamire, and R. G. Egdell, "Invited Topical Review: P-type transparent conducting oxides," *Journal of Physics: Condensed Matter*, vol. 28, no. 38, p. 383002, 2016, doi: 10.1088/0953-8984/28/38/383002.
11. B. Saha, R. Thapa, S. Jana, and K. Chattopadhyay, "Optical and electrical properties of p-type transparent conducting CuAlO2 thin film synthesized by reactive radio frequency magnetron sputtering technique," Indian Journal of Physics, vol. 84, pp. 1341-1346, 10/01 2010.
12. M. Poienar, F. Damay, C. Martin, V. Hardy, A. Maignan, and G. André, "Structural and Magnetic Properties of CuCr1−xMgxO2 by Neutron Powder Diffraction," Physical Review B, vol. 79, 01/12 2009.

13. Aoife B. Kehoe, Elisabetta Arca, David O. Scanlon, Igor V. Shvets, and Graeme W. Watson, (2016), Assessing the potential of Mg-doped Cr_2O_3 as a novel p-type transparent conducting oxide, J. Phys.: Condens. Matter, 28 (12), 125501. (DOI: 10.1088/0953-8984/28/12/125501)

14. Arca, E.; Fleischer, K.; Shvets, I. (2011), Magnesium, nitrogen codoped Cr_2O_3: A p-type transparent conducting oxide, Appl. Phys. Lett., APPL PHYS LETT, 99, 111910. (DOI: 10.1063/1.3638461)

15. Guo, D.; Guo, Q.; Chen, Z.; Wu, Z.; Li, P.; Tang, W. (2019), Review of Ga_2O_3 based optoelectronic devices, Mater. Today Phys., 11. (DOI: 10.1016/j.mtphys.2019.100157)

16. Jangir, R.; Kumar, D.; Srihari, V.; Bhakar, A.; Poswal, A.; Sagdeo, P.; Nand, M.; Jha, S.; Tiwari, P.; Ganguli, T. (2018), Studies on structural and optical gap tunability in α-$(Ga_xCr_{(1-x)})_2O_3$ solid solutions, J. Alloys Compd., 766. (DOI: 10.1016/j.jallcom.2018.07.001)

17. Jangir, R.; Srihari, V.; Bhakar, A. K.; Nand, M.; Shukla, D. K.; Jha, S. N.; Ganguli, T. (2022), Wide-Band-Gap p-Type $GaCrO_3$:Ni Semiconductor: A Hole Transport Material, ACS Appl. Energy Mater., 5 (7), 8629-8638. (DOI: 10.1021/acsaem.2c01154)

18. Sharma, Rishav & Baraik, Kiran & Srivastava, Himanshu & Mandal, Satish & Ganguli, Tapas & Jangir, R.. (2024). Structural and interface band alignment properties of transparent p-type α-GaCrO3:Ni/α-Al2O3 heterojunction. Journal of Applied Physics. 136. 10.1063/5.0205892.

19. R. Jangir, V. Srihari, A. Bhakar, C. Kamal, A. K. Yadav, P. R. Sagdeo, et al., "Structural and optical properties of transparent, tunable bandgap semiconductor: α-(AlxCr1−x)2O3," Journal of Applied Physics, vol. 128, p. 135703, 2020.

20. Shewmon, P. (1989), Diffusion in Solids, 2nd ed.; Minerals, Metals and Materials Society: Springer Cham.

21. Khachaturian, A. G. (1983), Theory of structural transformations in solids, John Wiley and Sons, New York, NY: United States.

22. Kortüm, Gustav (1969), Reflectance Spectroscopy: Principles, Methods, Applications, Springer-Verlag.

23. Atkins, Peter; de Paula, Julio (2014), Physical Chemistry, 10th ed., Oxford University Press.

24. Optical Properties and Electronic Structure of Amorphous Ge and Si (1968), Mater. Res. Bull., 3, 37-46. (DOI: 10.1016/0025-5408(68)90023-8).

25. Macdonald, J. R.; Barsoukov, E. (2018), Impedance Spectroscopy: Theory, Experiment, and Applications, John Wiley & Sons.

26. Goldsmid, H. J. (2010), Introduction to Thermoelectricity, Springer.

27. Jarrold, C. C. (2005), Electronic and Photoelectron Spectroscopy: Fundamentals and Case Studies By Andrew M. Ellis, Miklos Feher, and Timothy G. Wright, J. Am. Chem. Soc., 127 (33), 11877-11877.

28. Rietveld, H. M. (1969), A profile refinement method for nuclear and magnetic structures. J. Appl. Crystallogr., 2 (2), 65-71. (DOI: 10.1107/S0021889869006558)

29. Rodríguez-Carvajal, J. (1993), Recent advances in magnetic structure determination by neutron powder diffraction. Physica B: Condens. Matter, 192 (1), 55-69. (DOI: 10.1016/0921-4526(93)90108-I)

30. Chamberlin, E.; Wang, Y.; Lopata, K.; Kaspar, T.C.; Cohn, A.W.; Gamelin, D.R.; Govind, N.; Sushko, P.V.; Chambers, S.A. (2013), Optical absorption and spectral photoconductivity in a-(Fe1-xCrx)2O3 solid-solution thin films. J. Phys.: Condens. Matter, 25, 392002. (DOI: 10.1088/0953-8984/25/39/392002

31. Blazey, K.W. (1972), The wavelength-modulated reflectivity of Cr_2O_3 and its relation to the absorption spectrum of other Cr3þ-containing insulators. Solid State Commun., 11, 371-374. (DOI: 10.1016/0038-1098(72)90251-7).

32. Madolappa, S.; Choudhary, H. K.; Punia, N.; Anupama, A. V.; Sahoo, B. (2021), Dielectric properties of A-site Mn-doped bismuth sodium titanate perovskite: $(Bi_{0\cdot5}Na_{0.5})_{0.9}Mn_{0\cdot1}TiO_3$. Mater. Chem. Phys., 270, 124849. (DOI: /10.1016/j.matchemphys.2021.124849).

33. Pokhriyal, P.; Bhakar, A.; Sinha, A.; Sagdeo, A. (2019), Colossal dielectric permittivity and mechanism of AC conduction in bulk delafossite $CuFeO_2$. J. Appl. Phys., 125 (16), 164101. (DOI: /10.1063/1.5064483)

34. Jung, W.-H. (2013), Dielectric relaxation and hopping conduction in $La_2NiO^{4+\ \delta}$. J. Mater., 2013. (DOI: 10.1155/2013/169528).

35. Macedo, P. (1972), The role of ionic diffusion in polarisation in vitreous ionic conductors. Phys. Chem. Glasses, 13, 171-179.

36. Raymond, O.; Font, R.; Suárez-Almodovar, N.; Portelles, J.; Siqueiros, J. M. (2005), Frequency-temperature response of ferroelectromagnetic $Pb(Fe1⁄2Nb_{1/2})O_3$ ceramics obtained by different precursors. Part I. Structural and thermo-electrical characterization. J. Appl. Phys., 97 (8), 084107. (DOI: 10.1063/1.1870099)

37. Andrew, K. J. (1999), Dielectric relaxation in solids. J. Phys. D: Appl. Phys., 32 (14), R57. (DOI: 10.1088/0022-3727/32/14/201)

38. Schmidt, R.; Eerenstein, W.; Winiecki, T.; Morrison, F.; Midgley, P. (2007), Impedance Spectroscopy of Epitaxial Multiferroic Thin Films. Phys. Rev. B, 75, 245111. (DOI: 10.1103/PhysRevB.75.245111)

39. Hitha, H.; John, M.; Jose, A.; Kuriakose, S.; Varghese, T. (2020), Effect of Bi substitution on structural and electrical properties of polycrystalline $NiWO_4$ nanoparticles. J. Mater. Sci.: Mater. Electron., 31, 1-13. (DOI: 10.1007/s10854-020-04630-x)

40. Pokhriyal, P.; Bhakar, A.; Sinha, A.; Sagdeo, A. (2019), Colossal dielectric permittivity and mechanism of AC conduction in bulk delafossite $CuFeO_2$. J. Appl. Phys., 125, 164101. (DOI: 10.1063/1.5064483)

41. Lunca-Popa, P.; Afonso, J.; Grysan, P.; Crêpellière, J.; Leturcq, R.; Lenoble, D. (2018), Tuning the electrical properties of the p-type transparent conducting oxide $Cu_{1-x}Cr_{1+x}O_2$ by controlled annealing. Sci. Rep., 8 (1), 7216. (DOI: 10.1038/s41598-018-25659-3)

42. Pradhan, D. K.; Choudhary, R.; Rinaldi, C.; Katiyar, R. (2009), Effect of Mn substitution on electrical and magnetic properties of $Bi_{0.9}La_{0.1}FeO_3$. J. Appl. Phys., 106 (2), 024102. (DOI: 10.1063/1.3158121).

43. Ahad, A.; Shukla, D. K. (2019), A setup for Seebeck coefficient measurement through controlled heat pulses. Rev. Sci. Instrum., 90 (11), 116101. (DOI: 10.1063/1.5116160).